

INFORMATION TO USERS

This manuscript has been reproduced from the microfilm master. UMI films the text directly from the original or copy submitted. Thus, some thesis and dissertation copies are in typewriter face, while others may be from any type of computer printer.

The quality of this reproduction is dependent upon the quality of the copy submitted. Broken or indistinct print, colored or poor quality illustrations and photographs, print bleedthrough, substandard margins, and improper alignment can adversely affect reproduction.

In the unlikely event that the author did not send UMI a complete manuscript and there are missing pages, these will be noted. Also, if unauthorized copyright material had to be removed, a note will indicate the deletion.

Oversize materials (e.g., maps, drawings, charts) are reproduced by sectioning the original, beginning at the upper left-hand corner and continuing from left to right in equal sections with small overlaps. Each original is also photographed in one exposure and is included in reduced form at the back of the book.

Photographs included in the original manuscript have been reproduced xerographically in this copy. Higher quality 6" x 9" black and white photographic prints are available for any photographs or illustrations appearing in this copy for an additional charge. Contact UMI directly to order.

UMI

A Bell & Howell Information Company
300 North Zeeb Road, Ann Arbor MI 48106-1346 USA
313/761-4700 800/521-0600

UNIVERSITY OF ALBERTA

AN ELECTROMAGNETIC APPROACH TO THE TREATMENT OF
SCOLIOSIS

BY

EDMOND HOK-MING LOU



A THESIS
SUBMITTED TO THE FACULTY OF GRADUATE STUDIES AND RESEARCH
IN PARTIAL FULFILLMENT OF THE REQUIREMENTS
FOR THE DEGREE OF DOCTOR OF PHILOSOPHY

DEPARTMENT OF ELECTRICAL AND COMPUTER ENGINEERING

EDMONTON, ALBERTA

SPRING 1998



National Library
of Canada

Acquisitions and
Bibliographic Services

395 Wellington Street
Ottawa ON K1A 0N4
Canada

Bibliothèque nationale
du Canada

Acquisitions et
services bibliographiques

395, rue Wellington
Ottawa ON K1A 0N4
Canada

Your file Votre référence

Our file Notre référence

The author has granted a non-exclusive licence allowing the National Library of Canada to reproduce, loan, distribute or sell copies of this thesis in microform, paper or electronic formats.

The author retains ownership of the copyright in this thesis. Neither the thesis nor substantial extracts from it may be printed or otherwise reproduced without the author's permission.

L'auteur a accordé une licence non exclusive permettant à la Bibliothèque nationale du Canada de reproduire, prêter, distribuer ou vendre des copies de cette thèse sous la forme de microfiche/film, de reproduction sur papier ou sur format électronique.

L'auteur conserve la propriété du droit d'auteur qui protège cette thèse. Ni la thèse ni des extraits substantiels de celle-ci ne doivent être imprimés ou autrement reproduits sans son autorisation.

0-612-29065-4

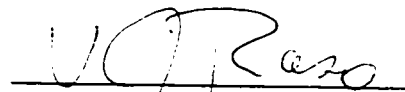
UNIVERSITY OF ALBERTA

FACULTY OF GRADUATE STUDIES AND RESEARCH

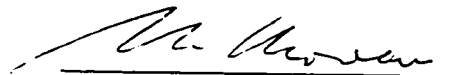
THE UNDERSIGNED CERTIFY THAT THEY HAVE READ, AND RECOMMEND TO THE FACULTY OF GRADUATE STUDIES AND RESEARCH FOR ACCEPTANCE, A THESIS ENTITLED AN **ELECTROMAGNETIC APPROACH TO THE TREATMENT OF SCOLIOSIS** IN PARTIAL FULFILLMENT OF THE REQUIREMENTS FOR THE DEGREE OF DOCTOR OF PHILOSOPHY.



Dr. N.G. Durdle
Supervisor



Mr. V.J. Raso
Co-Supervisor



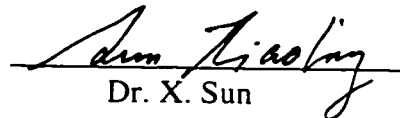
Dr. M. Moreau



Dr. A. Patwardhan



Dr. K. Stromsmore



Dr. X. Sun



Dr. A.M. Robinson

Date: April 7, 88

Abstract

A new proprioceptive approach to the treatment of scoliosis is proposed. This new approach requires a portable three-dimensional measurement system to detect the postural changes of a scoliotic trunk. Seven topographical features that significantly contributed to trunk deformities were identified. An objective method was developed examining trunk deformity. This objective method showed that the seven topographical features could be reliably and repeatably measured. Also, this method was chosen to assess the treatment outcome. To monitor the postural changes of a scoliotic trunk during daily activities, an electromagnetic three-dimensional measurement system has been investigated. An algorithm based on the electromagnetic theory was developed and implemented into the measurement system so that automatic measurements were obtained. Error analysis was done to demonstrate the accuracy of the system. Hardware and software challenges on investigating the electromagnetic approach were solved by theoretical analysis and laboratory testing. Finally a novel design of a three-dimensional low-power portable electromagnetic measurement system was developed. Experimental tests and clinical trials were done to verify that the accuracy of the system was able to detect the postural changes of human trunks.

Acknowledgement

Like any long piece of multi-disciplinary work, this work owns its success to number of people. I would like to express my profound gratitude to:

my supervisors, Dr. Nelson G. Durdle and Mr. James V. Raso for their guidance, support and encouragement throughout my studies.

my research team member, Doug Hill for his valuable suggestions and assistance with the drafting of papers and this thesis.

surgeons, Dr. Marc Moreau and Dr. Jim Mahood, for their valuable explanations and discussion about scoliosis.

my friend, Selina Shum for her valuable assistance in drawing diagrams and taking photographs.

my parents for their undying love, support and encouragement.

Last but not least, I really wish to thank my Almighty God who gave me strength, intelligence and confidence that made me completion of this thesis.

The financial support of the Department of Electrical and Computer Engineering, University of Alberta, the Glenrose Rehabilitation Hospital and the Alberta Heritage Foundations are gratefully acknowledged.

TABLE OF CONTENTS

1. INTRODUCTION	1
1.1. MOTIVATION	2
1.2. OBJECTIVES.....	4
1.3. OVERVIEW	5
2. LITERATURE REVIEW.....	6
2.1. THE ANATOMY OF HUMAN SPINE.....	6
2.1.1. <i>Cervical Spine</i>	9
2.1.2. <i>Thoracic Spine</i>	9
2.1.3. <i>Lumbar Spine</i>	12
2.1.4. <i>Sacrum</i>	12
2.1.5. <i>Coccyx</i>	13
2.1.6. <i>The Intervertebral Disc</i>	13
2.1.7. <i>The Spinal Ligaments</i>	17
2.2. SCOLIOSIS	19
2.2.1. <i>Definition of Scoliosis</i>	19
2.2.2. <i>Curvatures of the Spine</i>	21
2.2.3. <i>Rotation of Spine</i>	22
2.3. NATURAL HISTORY AND PREVALENCE OF IDIOPATHIC SCOLIOSIS	24
2.4. ETIOLOGY OF IDIOPATHIC SCOLIOSIS.....	26
2.4.1. <i>Growth Hormone</i>	27
2.4.2. <i>Bone</i>	28
2.4.2.a. <i>Vertebra</i>	28
2.4.2.b. <i>Rib Cage</i>	29
2.4.3. <i>Paraspinal muscle</i>	30
2.4.4. <i>Proprioception</i>	32
2.4.5. <i>Collagen</i>	33
2.4.6. <i>Genetics</i>	34
2.5. DETECTION OF SCOLIOSIS	35
2.6. TREATMENT OF SCOLIOSIS	38
2.6.1. <i>Non-surgical Treatment</i>	38
2.6.1.a. <i>Brace Treatment</i>	39
2.6.1.b. <i>The Physiotherapy Approach for the Treatment of Scoliosis</i>	42
2.6.2. <i>Surgical Treatment</i>	43
2.6.3. <i>Summary</i>	45
2.7. LITERATURE REVIEW OF THREE-DIMENSIONAL POSTURE MEASUREMENT SYSTEMS AND TRANSDUCERS	46
2.8. LITERATURE REVIEW OF ELECTROMAGNETIC SYSTEMS	49
3. TRUNK DISTORTION IN ADOLESCENT IDIOPATHIC SCOLIOSIS	51
3.1. INTRODUCTION.....	51
3.2. LITERATURE REVIEW OF METHODS FOR TRUNK ASSESSMENTS	52
3.3. SEVEN TOPOGRAPHICAL FEATURES.....	53

3.3.1. Shoulder Height Difference.....	55
3.3.2. Shoulder Angle Difference	55
3.3.3. Waist Asymmetry.....	55
3.3.4. Decompensation.....	56
3.3.5. Waist Crease.....	56
3.3.6. Scapular Asymmetry	56
3.3.7. Pelvis Asymmetry.....	57
3.4. RELIABILITY AND REPEATABILITY OF TRUNK MEASUREMENTS.....	57
3.4.1. Objective.....	57
3.4.2. Materials and Methods	57
3.4.3. Results and Discussion.....	60
3.5. SUMMARY	61
4. ELECTROMAGNETIC THEORY AND MEASUREMENT OF THE MAGNETIC FIELD DUE TO A MULTITURN SQUARE LOOP	62
4.1. INTRODUCTION.....	62
4.2. DESIGN PROCEDURES	63
4.3. DETERMINATION OF GAIN FACTOR DUE TO FERRITE CORES	65
4.4. THEORETICAL DEVELOPMENT AND EXPERIMENTAL RESULTS OF SELF-INDUCTANCE AND MAGNETIC FIELD DUE TO A MULTITURN SQUARE-LOOP COIL	69
4.4.1. Theoretical Analysis.....	70
4.4.2. Numerical Analysis and Results	75
4.4.3. Discussion and Conclusions.....	76
4.5. ALGORITHM TO CALCULATE POSITION AND ORIENTATION.....	81
4.6. SUMMARY	86
5. ERROR ANALYSIS.....	87
5.1. SYSTEMATIC ERRORS	87
5.2. SYSTEMATIC ERROR RELATED TO EFFECTIVE SURFACE AREA	89
5.3. SYSTEMATIC ERROR RELATED TO RESONANT FREQUENCY	90
5.4. SYSTEMATIC ERROR RELATED TO THE CURRENT IN THE TRANSMITTER COILS.....	93
5.5. SYSTEMATIC ERROR RELATED TO QUALITY FACTOR	94
5.6. MINIMUM AND MAXIMUM ERRORS	95
5.7. DISCUSSION.....	95
6. A NOVEL LOW POWER PORTABLE EM MEASUREMENT SYSTEM.....	96
6.1. INTRODUCTION.....	96
6.2. TRANSMITTER CIRCUIT	97
6.3. RECEIVER CIRCUIT	101
6.4. MICROCOMPUTER SYSTEM.....	105
6.4.1. The MC68HC16 Microcontroller	107
6.4.2. Digital Data Acquisition Section.....	108
6.4.2.a. Read Only Memory (ROM)	108
6.4.2.b. Read Access Memory (RAM).....	110
6.4.2.c. Programmable Real Time Clock (RTC)	111
6.4.3. Received Signal Section	112
6.4.3.a. The Multiplexer (MUX).....	112

6.4.3.b. <i>The Bandpass Filter (BPF)</i>	113
6.4.3.c. <i>RMS to DC Converter</i>	115
6.4.3.d. <i>Low Pass Filter</i>	116
6.4.3.e. <i>Phase Detection Circuit</i>	116
6.5. TEST OF THE RECEIVED SIGNAL SECTIONS	117
6.6. POWER CONSUMPTION.....	119
6.7. JUSTIFICATION DIFFERENT TYPES OF BATTERIES	120
6.8. SOFTWARE DEVELOPMENT	124
6.8.1. <i>Main Control Program</i>	124
6.8.2. <i>MAIN routine</i>	126
6.8.3. <i>INPUT mode</i>	127
6.8.4. <i>IRQ routine</i>	129
6.8.5. <i>CALIBRATION mode</i>	133
6.8.6. <i>OUTPUT mode</i>	135
6.8.7. <i>Interface Program</i>	135
6.9. SUMMARY.....	136
7. CALIBRATION PROCEDURES AND RESULTS	137
7.1. THE DISTANCE RANGE.....	137
7.2. CALIBRATION PROCEDURES	139
7.3. THE IMPLEMENTATION OF THE CALIBRATION RESULTS FOR THE SYSTEM	141
7.4. CALCULATION DEMONSTRATION	144
7.5. SUMMARY	146
8. LABORATORY MEASUREMENTS AND CLINICAL TRIALS.....	147
8.1. LABORATORY TEST PROCEDURES AND RESULTS	147
8.2. DISCUSSION.....	150
8.3. CLINICAL TEST PROCEDURES AND RESULTS	153
8.4. DISCUSSION.....	160
8.5. A COMPARISON BETWEEN A COMMERCIAL EM SYSTEM TO THE DESIGNED SYSTEM	161
8.5.1. <i>Procedures</i>	161
8.5.2. <i>Results and Discussion</i>	161
8.6. SUMMARY	163
9. CONCLUSIONS AND FUTURE DEVELOPMENT.....	164
9.1. CONCLUSIONS	164
9.2. RECOMMENDATIONS FOR FUTURE WORK	165
REFERENCES	167
APPENDIX A	180
A.1. CPU16.....	181
A.2. SYSTEM INTEGRATION MODULE (SIM)	182
A.3. ANALOG-TO-DIGITAL CONVERTER (ADC) MODULE.....	184
A.4. QUEUED SERIAL MODULE (QSM)	186
A.5. GENERAL PURPOSE TIMER (GPT) MODULE.....	186

A.6. STANDBY RAM (SRAM) MODULE	188
APPENDIX B	189
B.1. S-RECORD CONVERSION PROGRAM	190

LIST OF TABLES

Table 3-1. Summary of the Reproducibility of Trunk Measurements.	61
Table 4-1. The inductance of the larger holders with different number of turns of coil. ..	67
Table 4-2. The inductance of the smaller holder with different number of turns of coil. .	68
Table 4-3. The ratio between V_{xR} , V_{yR} and V_{zR} at different α_z with θ_z equal to 90°	85
Table 4-4. The values of a^2+b^2 and c at different θ_z and α_z	86
Table 5-1. The properties and characteristics of a coil with resonance circuit.	91
Table 6-1. Properties and characteristics of the transmitter coil with resonance circuit. ..	99
Table 6-2 a). The properties and characteristics of the receiver 1 with resonance circuit. .	102
Table 6-2 b). The properties and characteristics of the receiver 2 with resonance circuit. .	102
Table 6-3. Comparison of the microprocessor, microcontroller and DSP.	106
Table 6-4. The truth table between PD4-5, PF1-3 and the receiver channels.	113
Table 6-5. The current consumption of the system at each stage.	120
Table 7-1. The ratios between ($V_{xx} : V_{xy} : V_{xz}$), ($V_{yx} : V_{yy} : V_{yz}$), ($V_{zx} : V_{zy} : V_{zz}$), and ($V_{xR} : V_{yR} : V_{zR}$) on receiver 1 at calibration distances.	143
Table 7-2) The ratios between ($V_{xx} : V_{xy} : V_{xz}$), ($V_{yx} : V_{yy} : V_{yz}$), ($V_{zx} : V_{zy} : V_{zz}$), and ($V_{xR} : V_{yR} : V_{zR}$) on receiver 2 at calibration distances.	143
Table 8-1. The comparison of 10 position measurements on receiver 1 with the actual measurement.	148
Table 8-2. The comparison of 10 position measurements on receiver 2 with the actual measurement.	148
Table 8-3. The comparison between the average values of the distance r_a and angle α_a to the actual measured values r_m and α_m on the receiver 1.	149
Table 8-4. The comparison between the average values of the distance r_a and angle α_a to the actual measured values r_m and α_m on the receiver 2.	149
Table 8-5. The test result of subject 1.	155
Table 8-6. The test result of subject 2.	156
Table 8-7. The test result of subject 3.	157
Table 8-8. The test result of subject 4.	158
Table 8-9. Summary of the test results.	159
Table A-1. The configuration of PD0-PD7	188

LIST OF FIGURES

Figure 2-1. Anatomic planes.....	7
Figure 2-2. The anterior and lateral views of a normal spine.	8
Figure 2-3. Lateral view of cervical spine.	10
Figure 2-4. a) Superior view of a thoracic vertebra and b) lateral view of thoracic spine.	11
Figure 2-5. a) Superior and b) lateral views of a lumbar vertebra.	14
Figure 2-6. a) Anterior and b) posterior views of Sacrum.....	15
Figure 2-7. a) Anterior and b) posterior views of Coccyx.....	15
Figure 2-8. a) Superior and b) the cross sectional views of an intervertebral disc.	16
Figure 2-9. Ligaments in thoracic vertebra.....	18
Figure 2-10. Cobb Angle measurement.....	20
Figure 2-11. Five grades of vertebral rotation.	23
Figure 2-12. Iliac apophysis.....	25
Figure 2-13. Possible etiologies of idiopathic scoliosis.	26
Figure 2-14. Forward bending test.	36
Figure 2-15. a) A scoliometer and b) trunk rotation measurement.	37
Figure 2-16. Back view of a) a Milwaukee brace and b) a Boston brace.....	41
Figure 2-17. The surgical implant instrumentation.....	44
Figure 2-18. A Flock of Bird system developed by Ascension Technology Corporation.....	48
Figure 3-1. Cosmetic features of a scoliotic trunk.	54
Figure 3-2. The set up at the Glenrose hospital for taking images.	59
Figure 4-1. The outline of the smaller plastic holder with ferrite cube.....	64
Figure 4-2. The outline of the larger plastic holder with ferrite disc.	64
Figure 4-3. The position of the point P relative to the square loop of <i>abcd</i>	70
Figure 4-4. The coaxial orientation and the coplanar orientation of the receiver relative to the transmitter.....	73
Figure 4-5. The experimental and theoretical results on the coaxial and coplanar arrangement of coil-X to X.	78
Figure 4-6. The experimental and theoretical results on the coaxial and coplanar arrangement of coil-Y to Y.	78
Figure 4-7. The experimental and theoretical results on the coaxial and coplanar arrangement of coil-Z to Z.....	79
Figure 4-8. The experimental and theoretical results of the inductance on the transmitter with varying the number of turns of coil.	79
Figure 4-9. The experimental and theoretical results of the inductance on the receiver with varying the number of turns of coil.	80
Figure 4-10. The absolute error on the calculating inductance versus the number of turns of the coil on two different thickness of wires.....	80
Figure 5-1. The ratio of the actual area to the theoretical area at different dimensions of the coil.....	90
Figure 5-2. The ratio of the actual frequency to the theoretical frequency at different inductance and capacitance values.	92
Figure 5-3. The ratio of the actual current I to the maximum of current I_m versus inductance and capacitance.....	94

Figure 6-1. Schematic diagram of the inverted and non-inverted square wave signals generated.	99
Figure 6-2. The schematic diagram of the series LC transmitter circuits.....	99
Figure 6-3. The crosstalk voltage (1) and the resonant voltage (2) on two channels in transmitter.	100
Figure 6-4. The actual view of the transmitter unit.....	101
Figure 6-5. The schematic diagram of the receiver circuitry.....	103
Figure 6-6. The actual view of the receiver unit.	104
Figure 6-7. The time required for the receiver to receive a full scale signal after the transmitted signal was turned on.	105
Figure 6-8. The block diagram of the microcomputer system.....	107
Figure 6-9. The block diagram of the internal module of the MC68HC16Z1 microcontroller.	109
Figure 6-10. The block diagram of the connection between ROMs and MCU.....	110
Figure 6-11. The block diagram of the connection between RAMs and MCU.....	111
Figure 6-12. The block diagram of the connection between RTC and MCU.....	112
Figure 6-13. The internal circuitry of one section of the 2-nd order filter.	114
Figure 6-14. The schematic diagram of the active low pass filter.	116
Figure 6-15. The schematic diagram of the phase detection circuit.....	117
Figure 6-16. The output voltage from the low pass filter versus the input voltage on the bandpass filter of the channel 1.	118
Figure 6-17. The output voltage from the low pass filter versus the input voltage on the bandpass filter of the channel 2.	119
Figure 6-18. The discharge curves of the NiCd, NiMH and Li-ion batteries at 0.2C rate.....	123
Figure 6-19. The flowchart of the INIT routine.....	125
Figure 6-20. The flowchart of the MAIN routine.	126
Figure 6-21. The flowchart of the INPUT mode routine.....	128
Figure 6-22. The flowchart of the IN_CONV subroutine.	129
Figure 6-23. The flowchart of the IRQ routine.....	132
Figure 6-24. The flowchart of the CALIBRATION mode subroutine.....	134
Figure 7-1. The position of the transmitter and receivers at the back of the surface to measure the shoulder asymmetry feature.....	138
Figure 7-2. The distribution of the distance between the left shoulder and the pelvis....	138
Figure 7-3. The prototype system with one transmitter and two receivers lying over the grid map.	140
Figure 7-4. The first orientation of the receiver relative to the transmitter.	141
Figure 7-5. Four sets of data of receiver 1 and 2 at distance 32 cm.....	141
Figure 8-1. The absolute and percentage error of the measured distance at different distances on channel 1.	151
Figure 8-2. The absolute error of the measured angle α at different angles on channel 1.....	151
Figure 8-3. The absolute and percentage errors of the measured distance at different distances on channel 2.	152
Figure 8-4. The absolute error of the measured angle α at different angles on channel 2.....	152
Figure 8-5. One set of experimental test images from a subject.....	154
Figure 8-6. The average distance measurement with one standard deviation versus the actual distance from the Flock of Birds system	162

Figure 8-7. The average distance measurement with one standard deviation versus the actual distance from the designed system.....	162
Figure A-1. The internal addressing map of the MC68HC16Z1.	182
Figure A-2. The block diagram of SIM module.	184
Figure A-3. The block diagram of ADC module.	185
Figure A-4. The block diagram of QSM module.....	187
Figure A-5. The block diagram of GPT module.....	187
Figure B-1. An example of a S-19 record file	191

LIST OF ABBREVIATIONS

A	Ampere
AC	Alternating Current
A/D	Analog to Digital
AS	Address Strobe
Blt	Bend to left
BPF	Band Pass Filter
Brt	Bend to right
C	Capacitance or Capacitor
CE	Chip Enable
CMOS	Complementary Metal Oxide Semiconductor
CPU	Central Processing Unit
DC	Direct Current
DS	Data Strobe
DSP	Digital Signal Processor
E	System Clock Signal
EM	Electromagnetic
F	Faraday
f	Frequency
H	Henry
Hr	Hour
Hz	Hertz
IC	Integrated Circuit
IS	Idiopathic Scoliosis
k	Kilo
L	Inductance or Inductor
Li	Lithium
Ltsh	Lower left shoulder
LPF	Low Pass Filter
Lrtsh	Lower right shoulder
LSB	Least Significant Bit
M	Mega
mA	millampere
mAh	millampere-hour
MCU	Microcontroller Unit
μ	Micro
Mux	Multiplexer
NiCd	Nickel-Cadmium
NiMH	Nickel Metal Hydride
Ω	Ohm
OP-AMP	Operational Amplifier
PA	Posteroanterior
PC	Personal Computer
p-p	Peak to peak
R	Resistor or Resistance

RAM	Random Access Memory
Rltsh	Raise left shoulder
RMS	Root Mean Square
ROM	Read Only Memory
Rrtsh	Raise right shoulder
RTC	Real Time Clock
R/W	Read/Write
Rx.	Receiver
sec	second
3-D	Three dimensional
Tx.	Transmitter
Tx-x	Transmit from channel-x and receive in channel-x
Tx-y	Transmit from channel-x and receive in channel-y
Tx-z	Transmit from channel-x and receive in channel-z
Ty-x	Transmit from channel-y and receive in channel-x
Ty-y	Transmit from channel-y and receive in channel-y
Ty-z	Transmit from channel-y and receive in channel-z
Tz-x	Transmit from channel-z and receive in channel-x
Tz-y	Transmit from channel-z and receive in channel-y
Tz-z	Transmit from channel-z and receive in channel-z
UART	Universal Asynchronous Receiver Transmitter
V	Voltage
W	Watt

1. INTRODUCTION

This research introduces a new treatment approach for adolescents who have idiopathic scoliosis with mild to moderate curves. This approach is based on a biofeedback technique which uses proprioception by providing feedback signals to alert patients to adjust posture during daily activities. To investigate this approach, a low-power portable electromagnetic system is required. Research investigating low-power portable electromagnetic systems was carried out. This thesis describes the research required for the development of a new treatment tool as well as the new treatment approach.

Scoliosis is an abnormal curvature of the spine coupled with vertebral rotation. This abnormal curvature and vertebral rotation cause trunk deformities. Most patients are adolescent females who seek medical advice mainly because of their cosmetic appearance. Cosmetic appearance can be used as the basis for evaluating trunk distortion. To assess cosmetic appearance, topographical features that significantly contribute to trunk deformities are identified. A reliable and repeatable method that can permit an assessment of the postural changes has been developed.

To detect changes of topographical features, a measurement system is required. Literature review of different three-dimensional measurement systems has been carried out. Electromagnetic (EM) measurement systems were chosen to detect the postural changes. Since most of scoliotic patients are adolescent females, a small size and light weight measurement system was required. In the industrial market, most of the commercial EM systems are designed for laboratory environments; they are bulky, heavy and require AC power. Also, no feedback signals are generated from these systems.

Personal computer and technicians are required to operate these commercial systems. Therefore, the objectives of this research were to investigate a low-power portable electromagnetic device to the detection of the postural changes as well as a new approach to the treatment of scoliosis. The trunk distortion and back shape studies were to determine the features that contribute to deformity. EM theory was reviewed and confirmed as a basis for measuring the described features and to validate this new approach.

1.1. Motivation

According to the Scoliosis Research Society, about 10% of the adolescent population have some degree of scoliosis. This means that about 1 million children in the United States have scoliosis, and about 2.2% of those adolescents will require treatment, which consists of observation for further progression, bracing or surgery [90]. The number of new cases of scoliosis has been relatively constant and is about 200,000 per year in the United States. To determine the severity of scoliosis, the Cobb angle, which is the angle that measures the curvature of a scoliotic spine, is the most commonly used. A mild case of scoliosis is defined when the Cobb angle is less than 25 degrees; a moderate case is defined when the Cobb angle is between 25 to 45 degrees, while a severe case is defined when the Cobb angle is greater than 45 degrees. An untreated curvature can progress rapidly; 10 degrees or more in a few months. As the curve progresses, the size of the chest cavity can diminish, which can create respiratory problems for the child that will persist throughout life as well as cause pain and leave the child with a visible deformity.

Brace treatment is the most common non-surgical treatment for moderate scoliosis, but poor compliance and uncertainty about effectiveness are significant concerns. Poor compliance may be due to many factors. A brace limits physical activities and makes the wearer self-conscious about his/her appearance. In summer, hot weather combined with the poor ventilation of a brace makes the brace wearer feel very uncomfortable. Adolescents are particularly concerned about their appearance; some wearers refuse to wear the prescribed braces. The effectiveness of brace treatment is questioned [76, 77] by some researchers. It has been reported that braces reduce Cobb angles in the frontal plane, but they do not correct the 3-D thoracic spinal deformities [78]. Aubin *et al.* [79] reported that the Boston brace aggravates the deformity in the sagittal plane by shifting the spine and rib cage anteriorly and results in increasing thoracic hypokyphosis.

Children with mild curvature usually receive no treatment, but may be followed on a regular visit by an orthopaedist. Orthopaedists will recommend braces for patients when the spinal curvature is more than 25 degrees and the child has significant growth remaining. Most patients and their families are very concerned about comesis; this visible deformity of scoliosis is an important feature that often motivates families to seek treatment [89]. In a previous study, Mahood *et al.* [91] identified seven features: shoulder height and shoulder angle difference, waist asymmetry, decompensation, waist crease, scapula height and pelvis asymmetry which accounted for 85% of the overall impression of trunk deformity. Some researchers believe that improving the most striking features will result in a better appearance and can improve the scoliotic curve as well.

A biofeedback system is envisaged as a new method of improving cosmetic appearance as well as trunk deformities. To develop a biofeedback system, a three-dimensional system to measure the topographical features of the trunk must be developed. Once the system can detect the postural changes on a patient, an audio or vibrant feedback can be used to alert the patient to adjust the posture. The system must be low-power and portable so that patients can carry the system during their daily activities.

Electromagnetic measurement (EM) systems based-on a transmitter and a receiver are commonly used to determine three dimensional position and orientation. Commercial EM systems use high power and are bulky. A low-power portable and automatic EM system is required. An innovative approach to develop a low-power portable EM measurement device was a challenging task.

1.2. Objectives

The objective of this research was to investigate the use of portable EM systems to measure topographical features and providing feedback signal to patients to correct or improve trunk deformities. This research includes the following components:

- 1) identify significant topographical features that contribute to deformity,
- 2) establish reliability and repeatability of measuring the topographical features,
- 3) develop a theoretical framework for the analysis of postural status and provide feedback to patients in real time,
- 4) determine the accuracy and precision of the applied theory, and
- 5) confirm the clinical validity of this approach.

1.3. Overview

This thesis consists of 9 chapters. Chapter 2 reviews the literature on scoliosis, three-dimensional measurement systems and transducers, and electromagnetic systems. Chapter 3 defines the importance of topographical features most indicative of scoliosis, and describes a video image method to assess topographical changes. Also, the reliability and repeatability of that method are confirmed. Chapter 4 presents the electromagnetic theory to calculate the magnetic field due to a multiturn square-loop. Experiments have been done to confirm the EM theory. An effect due to the ferrite core inside a multiturn square coil has been investigated. An algorithm based on the EM theory was developed to calculate the three-dimensional parameters. Errors due to different factors that may occur in the system are discussed in chapter 5. Chapter 6 defines the system requirements and describes the technical challenges. Innovative approaches required to develop a low-power and miniature system are reported. Both hardware and software designs are reported. Chapter 7 reports the calibration procedures and the incorporation of calibration results into the system. Chapter 8 confirms the validation of the system through laboratory and clinical experiments. Chapter 9 provides conclusions and recommendations for future research and development.

2. LITERATURE REVIEW

This chapter introduces the medical background on scoliosis. It contains an introduction to the anatomy of the human spine, the definition of scoliosis, the natural history and prevalence of idiopathic scoliosis, the possible etiologies of idiopathic scoliosis, the detection of idiopathic scoliosis and the treatment methods for idiopathic scoliosis. Also, this chapter reviews the literature on three-dimensional measurement transducers and systems, and electromagnetic measurement systems.

2.1. The Anatomy of Human Spine

To have a better understanding of scoliosis, the anatomy of the vertebral column must be studied. While discussing the anatomy, the anatomic planes (Figure 2-1) are commonly used. The sagittal plane divides structures into a right and left side. The coronal or frontal plane divides structures into anterior and posterior sections. The axial or transverse plan lies at 90° to each of the other planes.

In a normal human spine, the vertebral column appears straight and symmetric in the frontal plane while a sinusoidal shape appears in the sagittal plane. A spine can be divided into five regions: cervical, thoracic, lumbar, sacrum and coccyx or tailbone. Figure 2-2 shows the anterior and lateral views of a normal spine. There are twenty-four vertebrae between the skull and the sacrum: seven cervical spine (C1-C7), twelve thoracic spine (T1-T12) and five lumbar spine (L1-L5). Both sacrum and coccyx are formed from the fusion of vertebrae into one solid bone. General descriptions of those five regions will be given in sections 2.1.1 to 2.1.5. Although the bones or vertebrae are similar throughout the spine, there are unique features that distinguish the vertebrae from

one region to another. Overall, the vertebrae from cervical to lumbar region are ringlike structures that provide bony protection to the spinal cord and support to the trunk of the body. Each vertebra may be separated into two main components: the body and the neural arch, and between each vertebrae is a fluid filled sac or disc. This segmental nature of the spine gives its flexibility. Spinal ligaments extend from the skull to the sacrum along the posterior and anterior surfaces of the vertebral body provide the flexible movement control at different regions of the spine. Sections 2.1.6 and 2.1.7 give a general description of both the intervertebral disc and spinal ligaments, respectively.

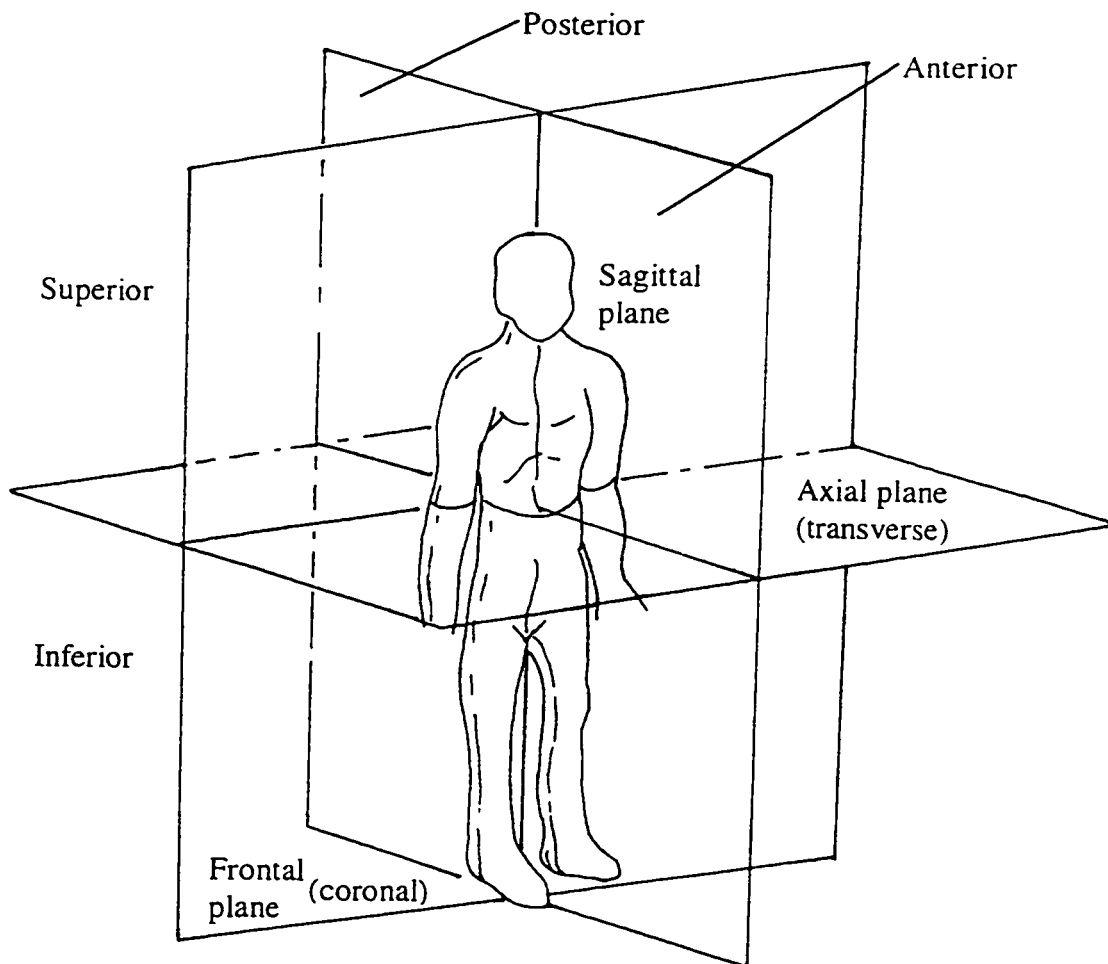


Figure 2-1. Anatomic planes.

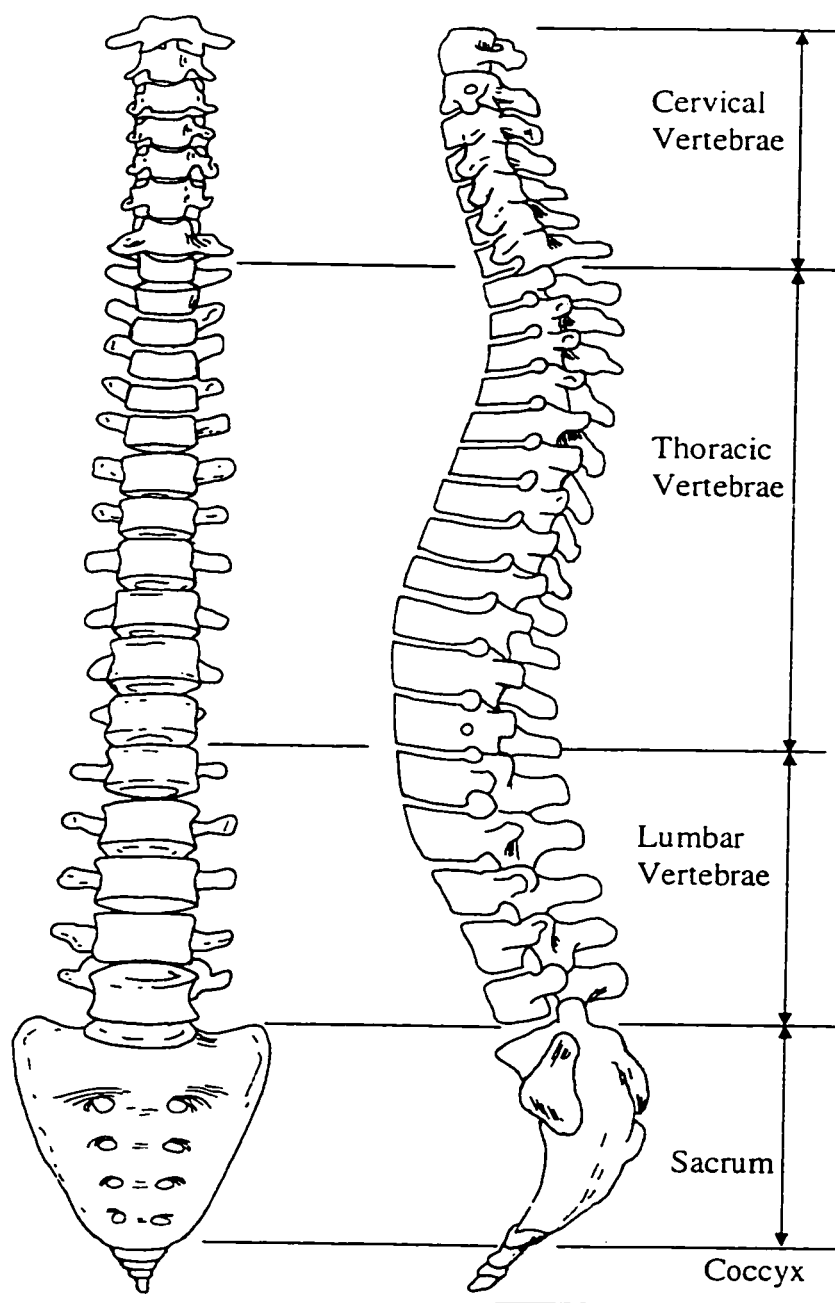


Figure 2-2. The anterior and lateral views of a normal spine.

2.1.1. Cervical Spine

Seven vertebrae comprise the cervical spine. They are arranged in a lordotic shape - a sagittal curve with the convexity anteriorly (Figure 2-3). The uppermost cervical vertebra C1, the atlas, is a ring-shaped structure articulating superiorly with the skull. The second vertebra C2, the axis, consists of a small body with a large neural arch in the transverse process. The C3 to C6 vertebrae have similar structures with the C7 vertebra having the largest spinous process.

2.1.2. Thoracic Spine

There are 12 thoracic vertebrae which are aligned in a kyphotic shape i.e. with curvature in the sagittal plane with the convexity posteriorly. Figure 2-4 shows the superior view of a thoracic vertebra and lateral view of thoracic column. The body of the thoracic vertebra is concave on four sides (top, bottom and lateral surfaces). Projecting backward from the vertebral body are the pedicles, short tubelike structures that essentially connect the vertebral body anteriorly to the laminae and spinous process. The pedicle joins the lamina with projections upward, which form the superior articular process. While the lamina projects downward, it reaches the inferior articular process. The thoracic spine is mainly responsible for lateral bending of the spine.

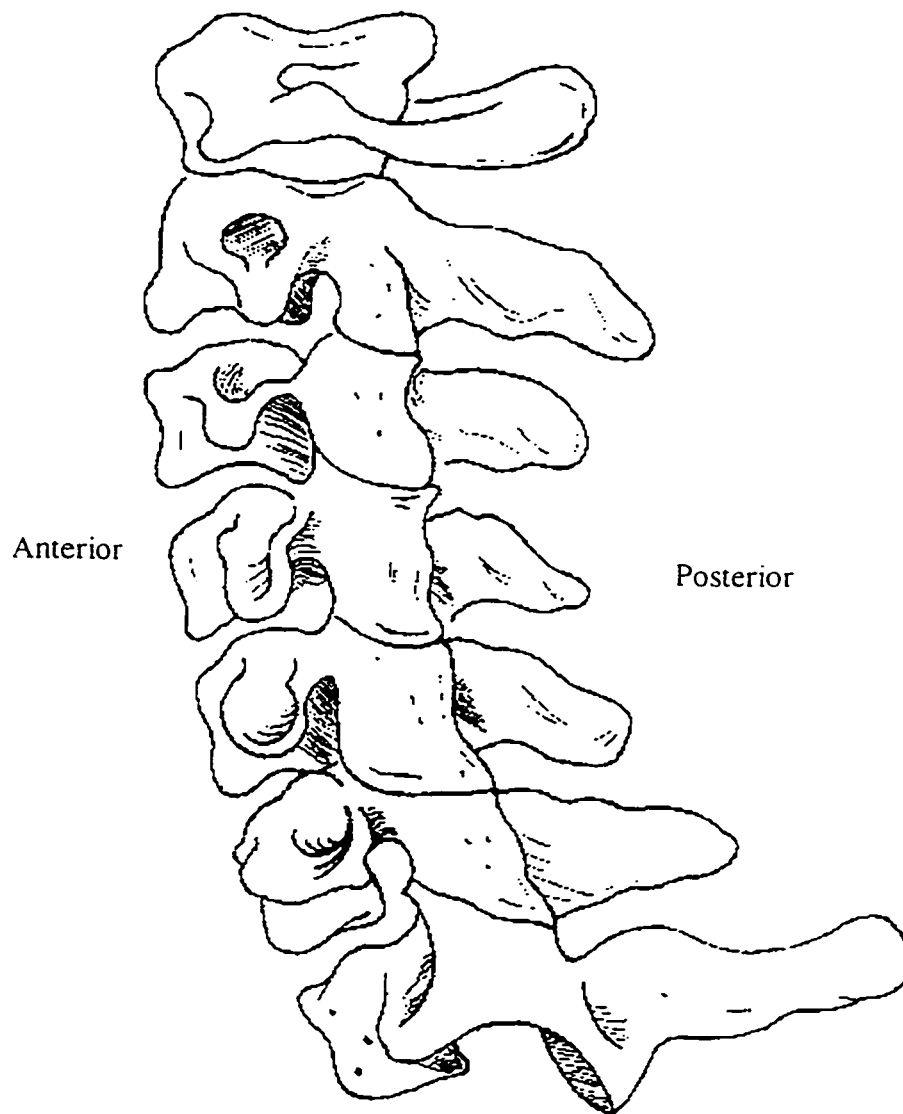


Figure 2-3. Lateral view of cervical spine.

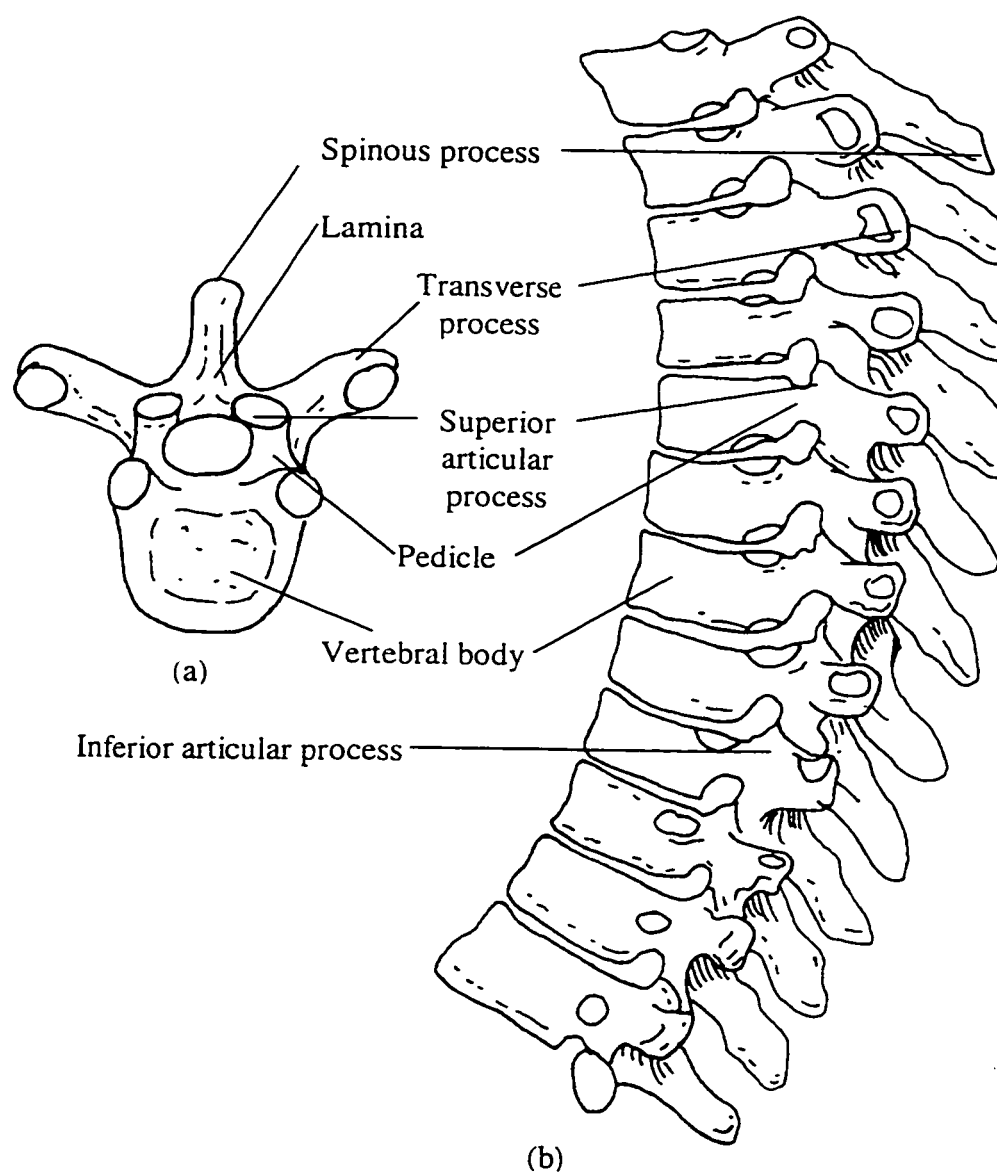


Figure 2-4. a) Superior view of a thoracic vertebra and b) lateral view of thoracic spine.

2.1.3. Lumbar Spine

There are five lumbar vertebrae, aligned in a lordotic shape, and all have similar characteristics. Figure 2-5 shows the superior and lateral views of a lumbar vertebra. The vertebral bodies are larger in the lumbar spine than in the thoracic or cervical spine. They are concave on their lateral and anterior surfaces. The pedicles project backward, linking the bodies to the posterior arch (the laminae and spinous process). The spinous processes are larger than those in the thoracic spine and project horizontally. The transverse processes in this region are smaller than those in the thoracic region. From the upper thoracic (T1) to lower lumbar (L5) spine, the size of each vertebra increases, providing inherent stability to a human spine. The lumbar spine is mainly responsible for forward bending (flexion) and posterior bending (extension).

2.1.4. Sacrum

The sacrum is made up of five vertebrae that are fused together. The anterior surface is concave in both the sagittal and frontal planes. Superiorly, the sacrum is broad so that the fifth lumbar vertebra can rest on top of that area. There are four pairs of foramina called the pelvis foramina, and between each pair is a ridge running transversely. The upper part of the first sacral vertebra is called the sacral promontory, and the area lateral to the pelvis foramina is called the pars lateralis. In the midline posteriorly is the sacral median crest, a fusion of the spinous sacral processes. Also there is a region called the sacral hiatus at where some bones are absent. At the cephalad end of the sacrum are two projections of bone superiorly, forming the superior articular

processes. The lateral surface of the upper vertebra is concave and articulate with the ilium on either side. Figure 2-6 shows the anterior and posterior views of the sacrum.

2.1.5. Coccyx

The coccyx is formed from the fusion of four rudimentary (undeveloped) vertebrae. Superiorly, there are projections of bone upward and lateral, called the coccygeal cornua and transverse processes, respectively. Each cornu articulates with the sacrum. Figure 2-7 shows the anterior and posterior views of the coccyx.

2.1.6. The Intervertebral Disc

The intervertebral disc is a composite structure that links contiguous vertebrae from C2 to the sacrum. It is a unique joint permitting multiplanar motion. The outer part of the disc, the annulus fibrosus, is made up of collagen fibers arranged in layers or lamellae. The lamellae are thicker and more numerous anteriorly. Each layer is oriented at 120° from each other (Figure 2-8). This interstriation angle imparts greater tensile strength. The outer lamellae are thicker than those toward the center. Furthermore, the collagen fibers of the outer lamellae are anchored to the end plate of the disc. The end plate is a 1 mm thick layer of hyaline cartilage attached to the inferior and superior surfaces of the vertebral body.

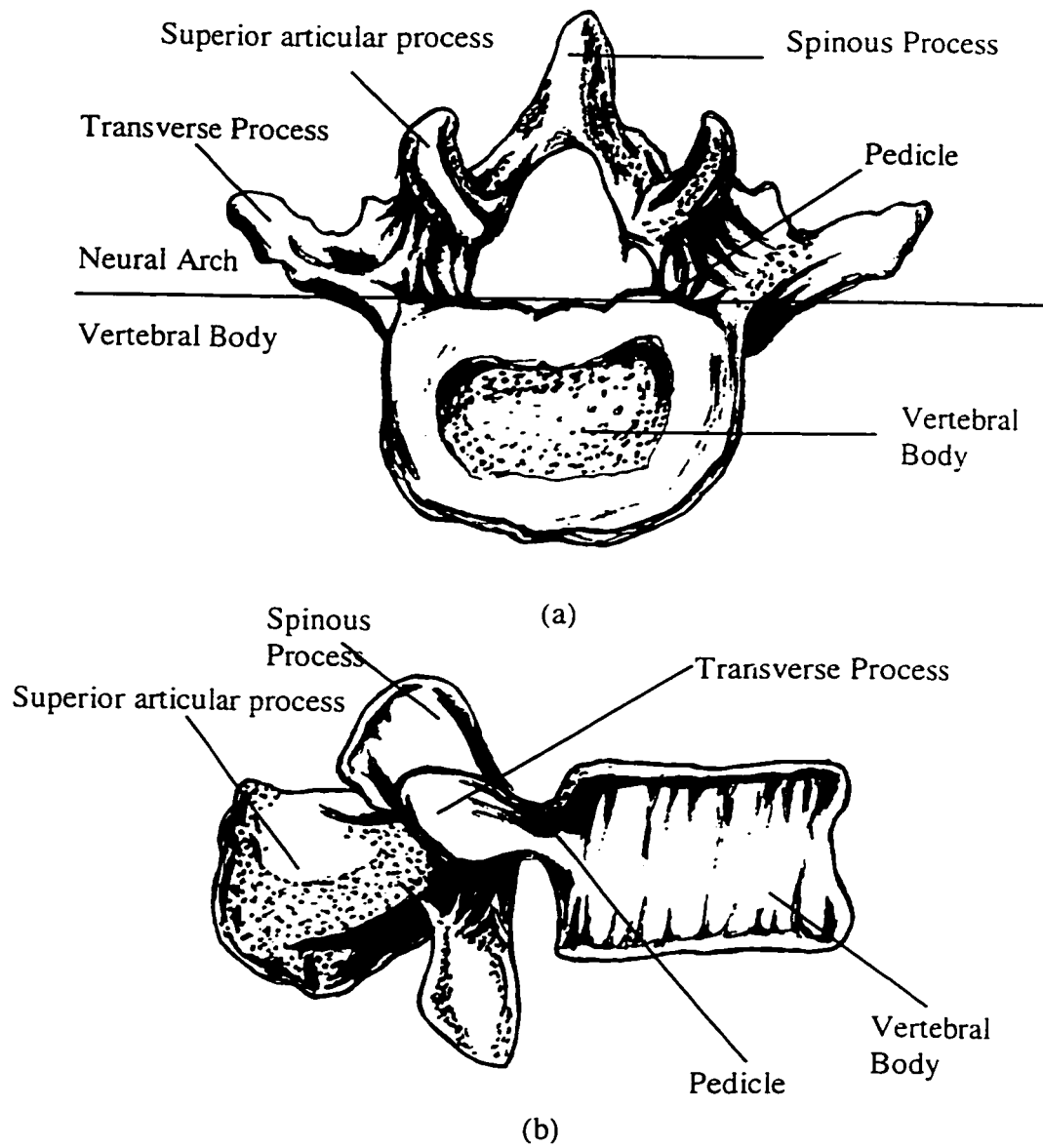


Figure 2-5. a) Superior and b) lateral views of a lumbar vertebra.

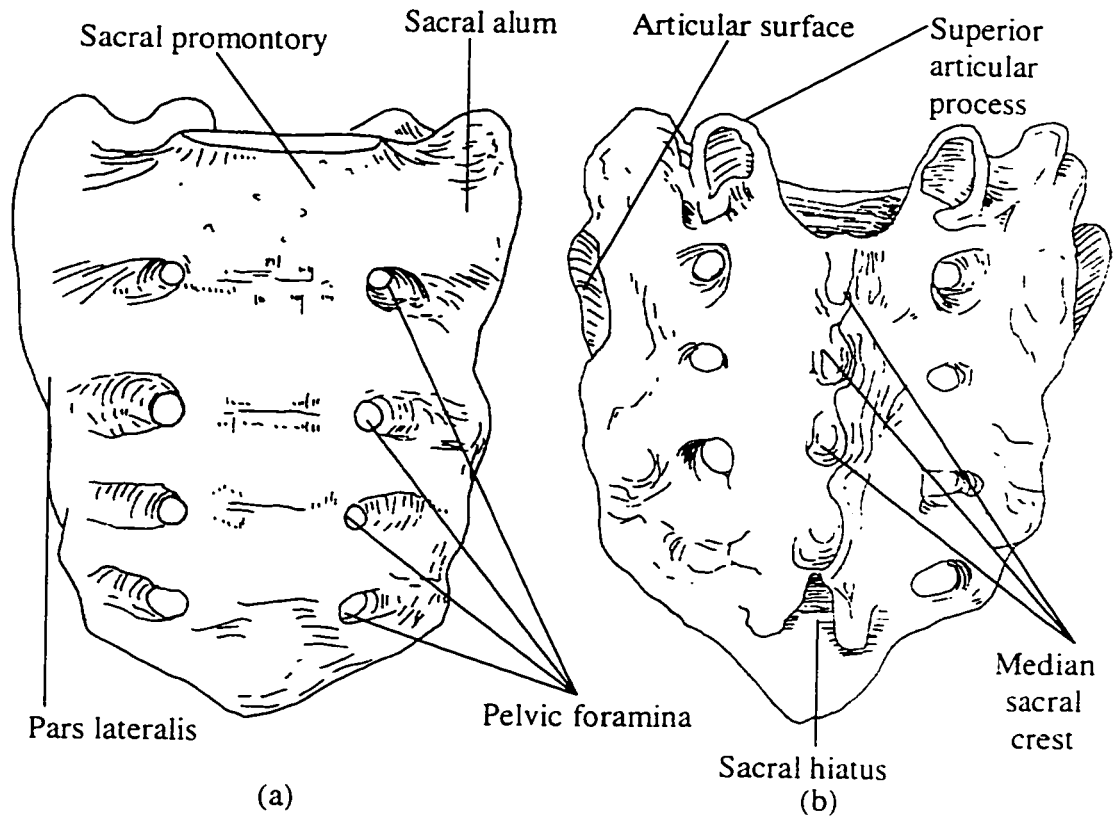


Figure 2-6. a) Anterior and b) posterior views of Sacrum.

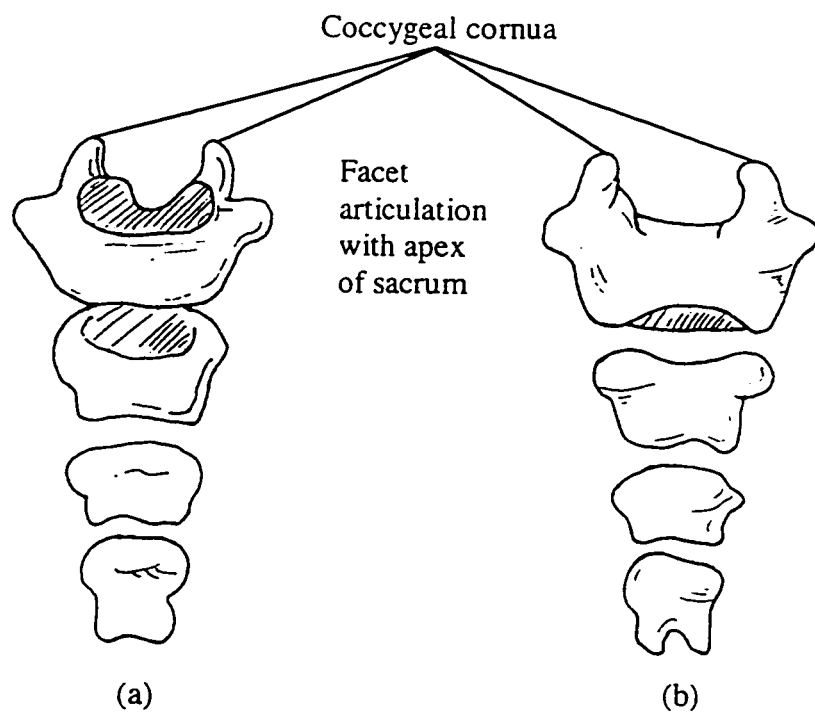


Figure 2-7. a) Anterior and b) posterior views of Coccyx.

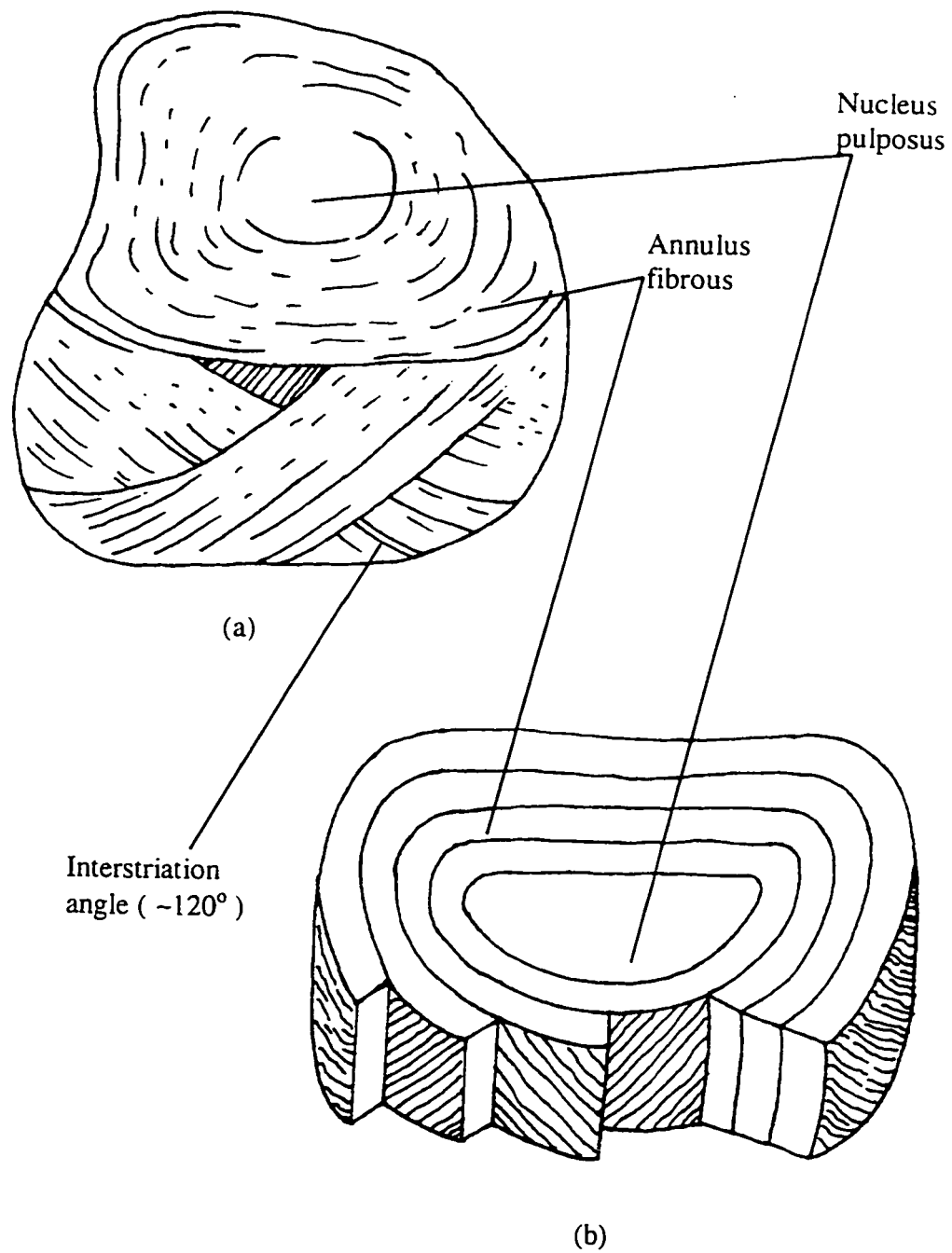


Figure 2-8. a) Superior and b) the cross sectional views of an intervertebral disc.

2.1.7. The Spinal Ligaments

There are eight sets of spinal ligaments which protect the spinal column from adverse loading conditions and provide a certain flexibility for the column. Starting from the posterior aspect, the eight sets of ligaments are (Figure 2-9): 1) the supraspinous ligament, 2) the interspinous ligament, 3) the anterior and posterior costotransverse ligaments, 4) the intertransverse ligament, 5) the ligamentum flavum, 6) the articular capsule ligament, 7) the posterior longitudinal ligament and 8) the anterior longitudinal ligament. Both the supraspinous and the interspinous ligaments connect the spinous processes of adjacent vertebrae and their functions are to prevent excessive rotation. The posterior and anterior costotransverse ligaments and the intertransverse ligaments connect the inferior aspect of one transverse process to the superior aspect of the adjacent transverse process. Their functions are to limit the lateral bending and axial rotation. The ligamentum flavum connects the lamina of adjacent vertebrae throughout the entire vertebral column. Its function is to limit flexion and intervertebral distraction. The articular capsule ligaments extend perpendicularly from the facets of one vertebra to the facets of the adjacent vertebrae. Both the posterior and anterior longitudinal ligaments extend from the skull to the sacrum along the posterior and anterior surface of the vertebral body. The function of the posterior longitudinal is the same as the ligament flavum, and the function of the anterior longitudinal ligament is to limit hyperextension.

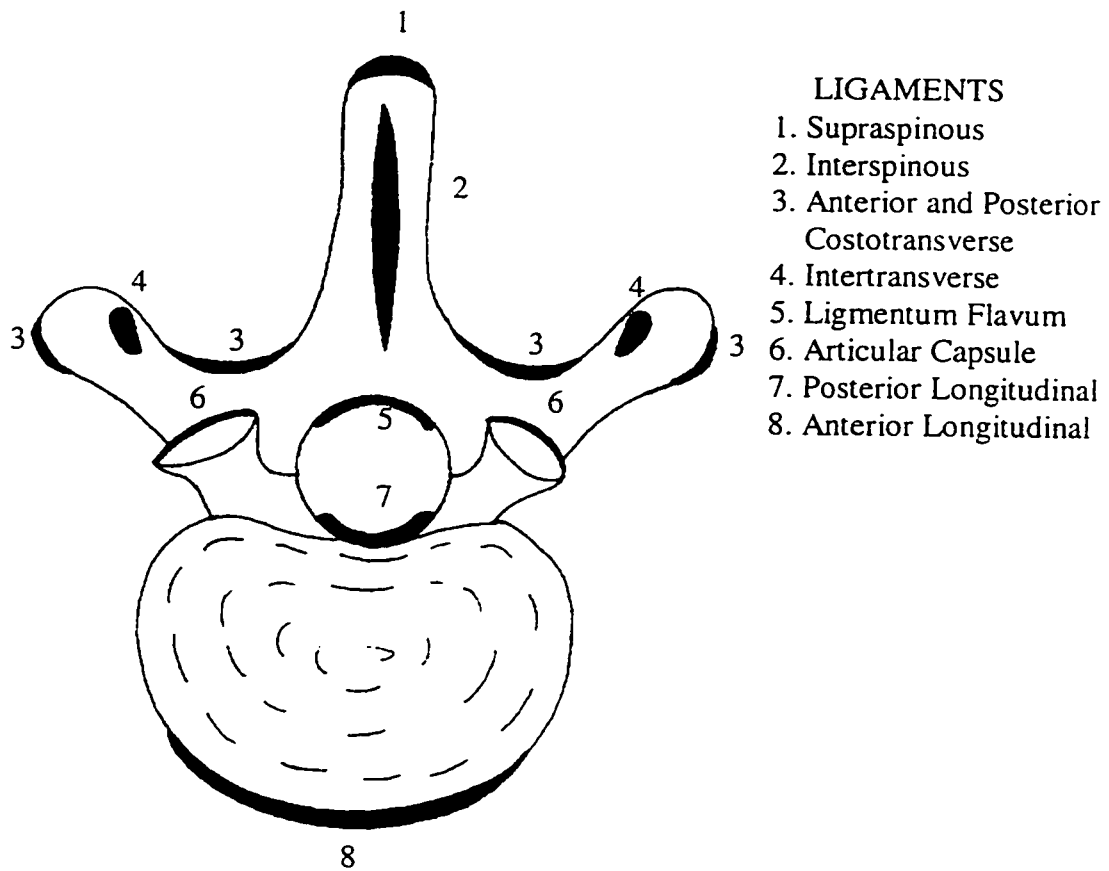


Figure 2-9. Ligaments in thoracic vertebra.

2.2. Scoliosis

This section includes a definition of scoliosis (section 2.2.1), the names and the types of different regions of scoliotic curves (section 2.2.2) and a definition of the rotation of scoliotic curves (section 2.2.3).

2.2.1. Definition of Scoliosis

The history of spinal deformity probably started from the days of Hippocrates, but the term scoliosis was first used by Galen (A.D. 131-201). Scoliosis is derived from the Greek word meaning curvature. When used in medical literature, it means a lateral curvature of the spine. Idiopathic scoliosis is divided into three categories according to when the condition first manifests itself: infantile or congenital (0-3 years), juvenile (3-10 years) and adolescent (10-17 years).

In 1948, Cobb separated scoliosis into two main groups, structural and functional or non-structural groups. A structural curve refers to a segment of the spine with a lateral curvature that lacks normal flexibility; a functional curve refers to a curve that has no structural component and that corrects or overcorrects on recumbent side-bending roentgenograms. In 1973, the Scoliosis Research Society was formed and one of its first tasks was to standardize the classification of spinal deformity based on Cobb's thinking [1]. The extent of a scoliosis is generally determined radiographically according to the Cobb measurement in a standing relaxed posteroanterior (PA) position. The Cobb angle is the gold standard to determine the curvature of the spine. To determine the "Cobb angle", the end-vertebrae of the curve must be first selected. These end-vertebrae are the vertebrae at the upper and lower limits of the curve which tilt maximally toward the

concavity. The Cobb angle is the angle between the lines, one draws along the upper end-plate of the upper body and one draws a second line along the lower end-plate of the lower body. Figure 2-10 shows the measurement of the Cobb angle. Another major task of the Scoliosis Research Society was to define the term scoliosis. It was defined as a lateral spinal curvature of the spine with 10° or greater in Cobb angle with vertebral rotation. Spinal curvature of less than 10° is viewed as a variation of normal spinal anatomy. Among more than 150 different types of spinal deformities, Idiopathic Scoliosis (IS), which means no known cause, is the most common form.

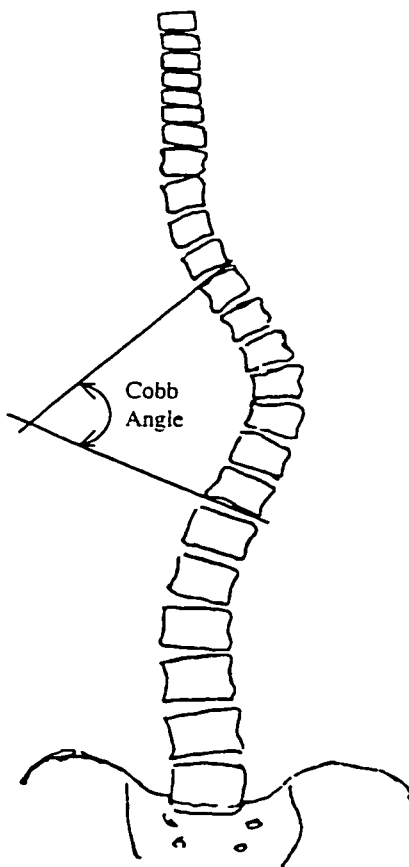


Figure 2-10. Cobb Angle measurement.

2.2.2. Curvatures of the Spine

Curvatures of the spine are identified by the area in which the apex (most abnormally deviated) of the curve is located [2].

Cervical curve : apex between C1 - C6.

Cervicothoracic curve : apex between C7 - T1.

Thoracic curve : apex between T2 - T11.

Thoracolumbar curve : apex between T12 - L1.

Lumbar curve : apex between L2 - L4.

Lumbosacral curve : apex between L5 - S1.

The four major curve patterns are the thoracic, lumbar, thoracolumbar and the double curve. Of the double curves, 90% have a right thoracic and left lumbar convexity.

King and Moe (1983) [2] have summarized idiopathic scoliosis into five types. with the following incidences.

Type I (12.9%): S-shaped curve in which both thoracic and lumbar curve cross the midline. The lumbar curve, which is more flexible on side bending, is greater than the thoracic curve on standing a radiograph.

Type II (32.6%): S-shaped curve in which the thoracic curve and lumbar curve cross the midline. The thoracic curve is greater than the lumbar curve.

Type III (32.8%): Thoracic curve in which the lumbar curve does not cross midline;

Type IV (9.2%): Long thoracic curve in which L5 is centered over the sacrum but L4 tilts into the long thoracic curve;

Type V (11.6%): double thoracic curve with T1 tilted into the convexity of the upper curve, the upper curve is rigid on side-bending.

2.2.3. Rotation of Spine

The axial rotation of vertebrae is assessed from anteroposterior or posteroanterior radiographs by examining the symmetry of the vertebral image. Cobb's method [3] was based on the offset of the spinous process from the center of the vertebral body. In 1969, Nash and Moe demonstrated that the shadow of the pedicle [4] could have better results on determining the angle of vertebral rotation. Nash and Moe classified the vertebral rotation into five grades (grade zero to grade IV) (Figure 2-11). Grade zero means that there is no rotation of the vertebrae; the shadow of the pedicle is symmetrical and equidistant from the sides of the vertebral body. Grade I rotation occurs when the pedicle shadow or the convexity has moved away from the side of the vertebral body. In grade II, the pedicle shadow is about 2/3 of the way to midline. In grade III rotation, the convex pedicle shadow is situated in the middle of the vertebrae. In grade IV rotation, the convex pedicle shadow is past the center of the vertebral body and closer to the concavity of the curve. In the 1980s, more quantitative methods [5, 6] have been used to assess axial vertebral rotation by using landmarks on the vertebra (usually pedicles or the spinous process and the vertebral body).

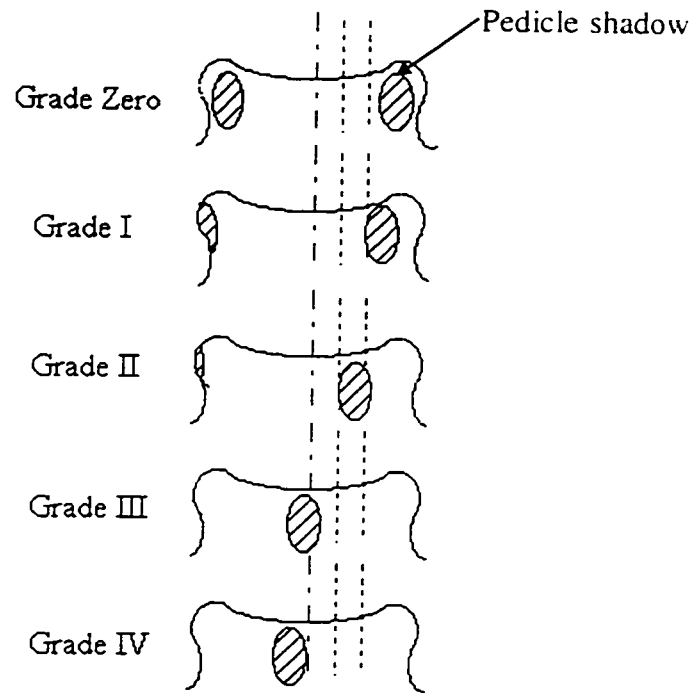


Figure 2-11. Five grades of vertebral rotation.

2.3. Natural History and Prevalence of Idiopathic Scoliosis

According to the age of onset, IS can be divided into three groups: the infantile, juvenile and adolescent. Some obvious signs are noticed in these three groups. The progressive infantile type is more common in boys, the adolescent type is more common in girls, while the juvenile type is about equally distributed. The common pattern of deformity in the infantile group is a left convex thoracic curve, in the adolescent group a right convex thoracic curve, while in the juvenile group there is equally distribution.

The Cobb angle can be used to measure the severity of the scoliosis. The prevalence of a Cobb angle greater than 10, 20, 30 and 40 degrees are 2-3%, 0.3-0.5%, 0.1-0.3% and less than 0.1% of the adolescent population, respectively [7]. The risk of further progression is much higher in females than in males. For those population with Cobb angles greater than 10, 20 and 30 degrees, the ratio of female to male are (1.4 to 2):1, 5.4:1 and 10:1, respectively [8].

Growth is one of the most important factors in the manifestation of adolescent IS. Although it is not possible to accurately predict the development of scoliosis in adolescents, a study was reported that the greatest risk of progression occurs prior to the maximum growth velocity [9]. The growth velocity is related to the age of the children. To determine the bone age of a patient, the radiograph of a patient's wrist may be used [10]. Also the cessation of spinal growth can be determined by the extent of the ossification of the iliac apophysis [11]. Ossification normally starts at the anterior superior iliac spine and progresses posteriorly to the posterior superior iliac spine. When the excursion of ossification is complete, fusion to the iliac crest occurs. Risser divided the excursion into four grades: 1 is 25% excursion, 2 is 50%, 3 is 75%, 4 is complete

excursion, and he assigned sign 5 as the fusion to the ilium (Figure 2-12). A Risser value of 0 signifies that no ossification has yet occurred. In general, a Risser sign 4 correlates with the cessation of spinal growth, and Anderson *et al.* [12] have shown that a Risser sign 5 correlates with cessation of height increase. In 1984, Lonstein and Carlson [13] evaluated the probability of the curve progression based on Risser's grade and found that the risk of progression decreases as skeletal maturity increased. Also, in 1982, Nachemson *et al.* found that the younger the patient at the time of diagnosis, the greater the risk of progression [14]. The curve patterns are also related to curve progression. A double-curve pattern has a greater tendency to progress than a single-curve pattern. Furthermore, the larger the magnitude of the curve at detection, the greater the risk of progression [15].

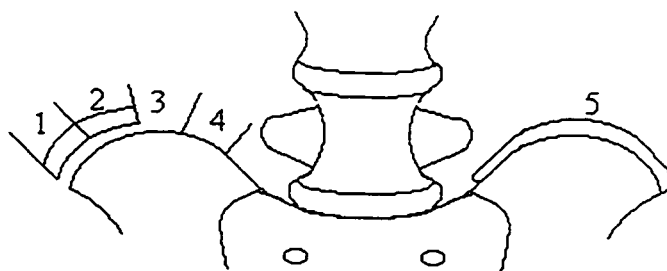


Figure 2-12. Iliac apophysis

2.4. Etiology of Idiopathic Scoliosis

Although the etiology of IS has been sought for many years, no single causative factor has been identified. Numerous suggestions have been made on the etiology of IS, which were summarized in "The Aetiology of Idiopathic Scoliosis" by Robin [16]. Figure 2-13 shows all the possible factors which would cause the idiopathic scoliosis, and each of the possible factors will be summarized in sections 2.4.1 to 2.4.6.

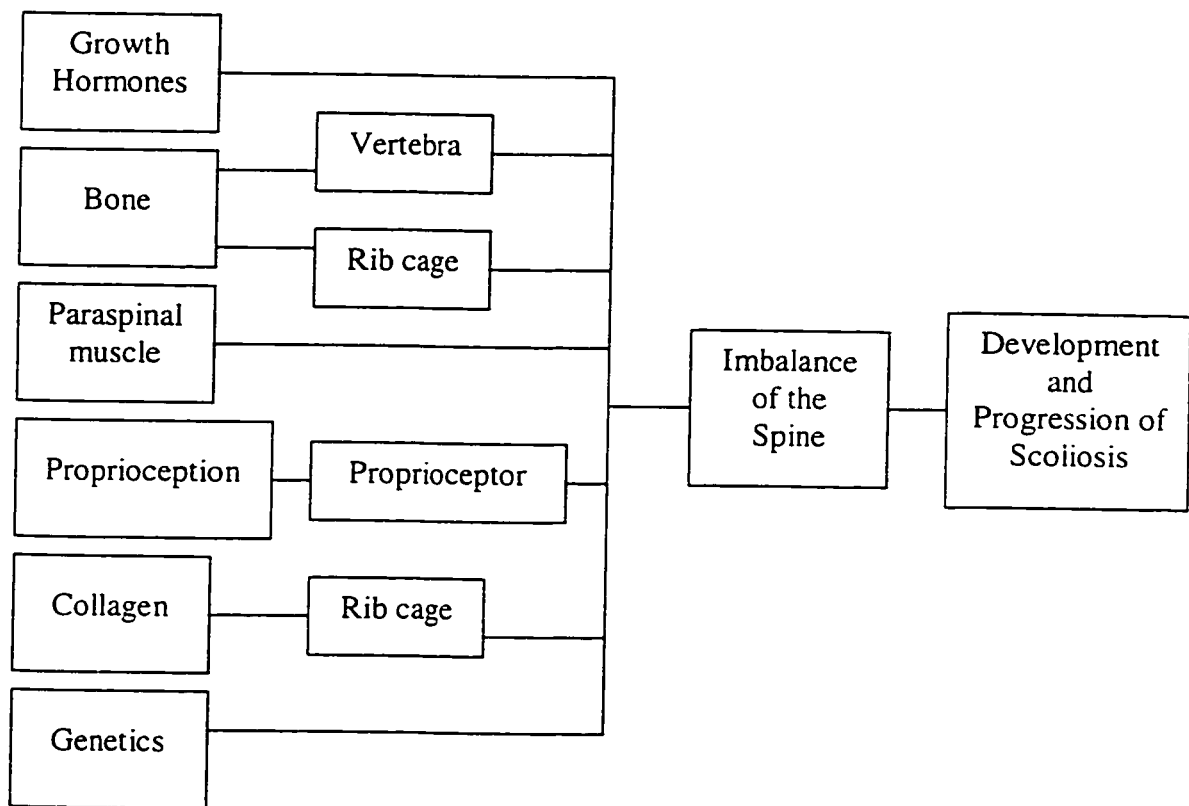


Figure 2-13. Possible etiologies of idiopathic scoliosis.

2.4.1. Growth Hormone

Observations have been made that people who have IS are taller than normal healthy non-scoliotic individuals [17, 18, 19, 20]. Also, idiopathic scoliosis is more prevalent in girls and curve progression usually occurs during the rapid growth period and stops when growth ceases [21]. This fact attracted some researchers to study the relationship between growth hormone and IS. Most researchers expected that growth hormone should be higher in growing children and postulated that a disturbance of growth hormone might be the cause of IS. The first group to study growth hormone in subjects with IS was Misol *et al.* [22]. They compared 15 moderate (with Cobb angle about 40°) subjects with IS to normal controls. They found that growth hormone showed great variation between individuals, but the correlation between growth hormone level and severity could be made. Somatomedins, a group of growth promoting chemicals released mainly from the liver in response to growth hormone, were studied by Willner *et al.* [23]. They studied 48 girls with IS and 23 normal controls and found an elevated serum level of somatomedin in the scoliotic girls. However, they didn't explain why the higher growth hormone and somatomedin levels would cause the IS. Skogland and Miller [24] studied 95 children with IS and 60 normal controls testing growth hormone and testosterone. They found a significantly higher response to growth hormone level in 7 to 12 years old girls with IS, but no significant difference was found among older girls. Also, the testosterone level was found to be higher in girls with IS between 9 and 12 years of age. Therefore, these findings supported the accelerated prepubertal growth in adolescent girls with IS. However, the mechanism by which the growth hormones affect IS had not been discussed. In 1981, Skogland *et al.* [25] reported another study where

serum levels of somatomedin A were normal in girls with IS under 13 years, but higher in the normal group than the scoliotics for age over 13. Therefore, they concluded that growth rate in the normal control group was higher than in the scoliotic girls over age 12 years.

From the above studies, one can only conclude that growth patterns and growth hormone appear to be different between normal and scoliotic adolescents.

2.4.2. Bone

2.4.2.a. Vertebra

Spinal biomechanics is a study of directed forces that produce equilibrium, motion, and deformity of the vertebral column. The most popular analogy of the biomechanics of spinal deformity in IS has been related to the Eulerian theory of buckling of a slender rod. Euler's mathematical expression assumes that all loads on the column under analysis are vertical and centered over the column. Column failure can be divided into short and long column analysis. Most spinal deformities can be described as problems in long column stability. Stability is defined as the tendency of the spinal column to return to its normal anatomic configuration when relatively small loads are applied. The mathematical expression for long column stability is $P < K \bullet \frac{EI}{L^2}$, where P is the compressive load, K is a constant, EI is the stiffness modulus of the column, and L is the length of the column. As long as the compressive force remains within limits set, column failure does not occur. The rotatory element of the deformity has been described as a "buckled lordosis"[26]. In 1978, Meade *et al.* [27] pointed out that the approach of

the Euler's theory is too simple. It could not explain the majority of the clinical findings in IS, especially in relation to curve progression.

In 1952, lordosis of vertebrae was first suspected as a primary cause of IS by Somerville [28]. Somerville postulated that failure of growth of the posterior elements of the vertebra would cause structural lordosis. As the spine flexed forward above and below to compensate for this lordosis, it was easier for the affected area of the spine to rotate instead of bending further forward. However, Somerville's work did not explain why the posterior parts of the spine would fail to grow. Roaf [29] suggested that the cause of scoliosis was due to growth being inhibited on the concave side and unrestrained on the convex side. However, in 1963 Roaf found that his assumption was wrong. Knutsson [30] postulated that abnormalities in the vertebral bodies themselves with asymmetrical growth at the paired neurocentral junction were the causes of IS. He explained that if the closure of the neurocentral junction took place at a different rate and lead to a premature synthesis on one side, the vertebral body would be twisted. However, experimental work by Enneking and Harrington [31] disproved this hypothesis.

2.4.2.b. Rib Cage

Olsen and Allan [32] were the first group to propose that lateral stability of the rib cage was the possible etiology of scoliosis. They commented that the rib cage could generate strong stabilizing forces in resisting lateral bending. Sevastikoglou *et al.* [33] postulated that asymmetrical growth of ribs could be a cause of IS. To prove their hypotheses, they operated on two groups of rabbits : one group with shortening of four ribs on one side and another group with shortening of four ribs on one side and fracture

of ribs on the other side. After 8 weeks, there was no apparent scoliosis in the first group, while three surviving rabbits in the second group developed scoliosis convex to the shortened side. They concluded that stimulation of longitudinal growth of the ribs might be one of the reasons for the spinal deformity of IS in human. However, clinical observations were controversial. Normelli *et al.* [34] reported their observations of six cases where the left ribs at the level of the concavity were found to be longer than the right ribs in five cases. While Stokes *et al.* [35] observed rib arc length on 71 patients with IS, 11 of 19 patients with single right thoracic IS tended to have longer ribs at the apex; 9 of 15 patients with left lumbar IS had longer ribs on the left side and 11 of 22 patients with double curves had ribs longer on the left. However, Sevastik *et al.* [36] performed rib elongation of 1 cm on the right side on rabbits and found that the rabbits developed immediately scoliosis convex to the left, thoracic lordosis, rotation of the vertebrae and a rib hump on the right. Even though there is no doubt that the geometry of the rib cage must have considerable mechanical influence on the spine in IS, it cannot be concluded that the asymmetry of the ribs is primary or secondary to IS.

2.4.3. Paraspinal muscle

The idea that disease or disability of muscle might be related to the pathogenesis of scoliosis was first raised nearly three hundred years ago. Many investigators pointed out that the spinal deformity of IS was due to abnormal contraction of the muscle on the concave side of the curvature [37]. Schwartzman and Miles [38] studied the effects of excision of part of the paraspinal musculature in rats and mice, and they postulated that muscle imbalance was the possible etiology of IS. More recently, Smith and Dickson

[39, 40] have shown that unilateral destruction of the posterior spinal muscles markedly increases the degree of deformity. To study the relationship between the spinal muscles and the etiology of IS, the strength of the muscle had to be measured. The first method used to measure the strength of the muscle was an electromyograph (EMG) by Riddle and Roaf [41]. They expected that the amplitude of the EMG tracing was higher on the convex side of the curve; however, clinical reports were controversial. Most of the investigators found that the EMG activity was greater on the convex side of the curve [42], but Badger [43], Gueth and Abbink [44] found no evidence of increased convex side EMG activity in the scoliotic subjects. Reuber *et al.* [45] was another group to study the EMG activity. They found that there was no significant difference in EMG activity between the normals and the subjects with IS whose curves were less than 25° , but the EMG activities of those subjects whose curves were more than 25° were significantly more asymmetric than normals. Reuber *et al.* analyzed their results using a biomechanical model and suggested that scoliosis progression seemed not to be caused by asymmetries in muscle contraction.

Another possible etiology of IS was imbalance of type I fibers in the paraspinal muscle. The imbalance of type I fibers might provide a sustained muscle pull on the spine which caused a curve convex to that side. Although Roaf [46] and Gonyea *et al.* [47] found a higher proportion of type I fibers on the convex side of IS at the apex, they could not explain whether the muscle fiber imbalance was primary or secondary to IS. Therefore, further studies were required to prove the postulates.

2.4.4. Proprioception

Proprioception is the sense of position of one part of the body relative to another. Proprioceptive dysfunction has been put forward as a possible etiology of IS in recent years [48, 49, 50, 51, 52]. One of the hypotheses is that, in the case of IS, a proprioceptive rearrangement or re-calibration of the internal representation of the body in space is present, and that a non-erect vertebral alignment may be erroneously perceived as straight. In 1979, Sahlstrand and coworkers [53] examined postural equilibrium in subjects with IS. They tested the postural sway and evaluated the electronystagmography of labyrinthine function. The results showed that there was a significant difference in postural equilibrium between normal children and those with scoliosis. Also, Keesseen [52] compared the proprioceptive accuracy among groups of scoliotic subjects, those with non-progressive spinal asymmetry and normal subjects. He found that there was a significant difference between the first two groups and the last group. However, no one was able to conclude whether the vestibular dysfunction was the cause or merely a result of the spinal deformity. Wyatt *et al.* [54] reported that scoliotic subjects had more difficulty in detecting vibration than normal controls. Also, they concluded that the posterior column dysfunction was somehow related to scoliosis. Yamamoto [55] postulated that the vestibular dysfunction was due to a defect in the brain-stem. Dubousset *et al.* [56] continued the study of the connection between brain-stem and scoliosis, and they stated that the continuous dysfunction of the postural reflex system might be the pathway in IS. However, they could not conclude that the defect of the brain-stem resulted in the development of IS.

2.4.5. Collagen

Bones, tendon and ligaments are held together by a "cement" called collagen which mainly consists of glycoproteins. Perhaps the most comprehensive work on this subject is by Nordwall [57]. However, Nordwall was unable to demonstrate that IS was caused by an abnormality in the mechanical properties of ligaments and tendons or by laxity of the joints. Later investigative work by Bradford *et al.* [58] led to the same conclusion. However, their reports were controversial. Pedrini *et al.* [59] studied the collagen level in the intervertebral disc and found the collagen level was higher in the nucleus pulposus. Taylor *et al.* [60] found the collagen content in the annulus on the concave side of the spinal deformity decreased, especially at the apical disc itself, but the collagen content increased in the nucleus pulposus at the apex of the curve. Robin [16] suggested that these findings might be related to an abnormality of collagen cross-linking. This hypothesis was also proposed by other authors [61, 62, 63]. Solubility of ligamentous tissue has been used to detect cross-link defects in collagen. Venn *et al.* [58] studied the collagen content and solubility in relation to cross-linking defects by comparing the supraspinous and interspinous ligaments from both subjects with IS and normals. He found no significant difference in the ligament collagen between the two groups. Furthermore, in 1983 Oegema *et al.* [64] concluded that IS was not due to a biochemical abnormality in either the annulus fibrous or nucleus pulposus. To summarize the findings in relation to collagen, it was accepted that the collagen abnormality in IS might be due to the definitive enzymatic findings in some individual collagen diseases. The possibility that IS may be a defect of collagen cross-linking still awaits for further proof.

2.4.6. Genetics

Genetics was one of the possible factors which most researchers believed was related to the etiology of scoliosis. Nitché and Armknecht [65] were the first group to point out the occurrence of scoliosis in twins. A major study of IS in twins was carried out in New York by Fisher and DeGorge [66]. They studied 1400 cases of IS, finding 17 pairs of twins. Of these only 14 pairs were able to be studied in depth. Six were monozygotic and eight were dizygotic. They found that all the monozygotic twins showed a concordant pattern of scoliosis. "Maternal environmental factors" could play an important role in the development of the disease. James [67] summarized some of these studies, and showed that three quarters of the identical twin pairs showed scoliosis in each child, while only half of the dissimilar twins had scoliosis in each. Familial patterns were also studied by many investigators [68, 69]. They come up with two genetic mechanisms involved in the inheritance of scoliosis; one was either an autosomal or sex-linked dominant or a recessive Mendelian (multiple gene inheritance pattern) systems mechanism and the other was a multifactorial polygenic transfer. In 1968, Wynne-Davies [70] reported on 114 cases of IS from the Edinburgh Scoliosis Clinic. The results showed that, in early onset type (infantile), the frequency of scoliosis in relatives from first to third degrees was 2.6%, 2.3% and 1.4%. In the late onset group (adolescent), the results were 6.94% in the first degree, 3.69% in the second degree and 1.55% in the third degrees. These results supported either a dominant or recessive Mendelian mechanism. However, Riseborough and Wynne-Davies [71] reviewed the families of 207 IS patients from Boston; they found a higher incidence of affected first degree relatives (11.1%) and about the same incidence in the second and third degrees

(2.4% and 1.4% respectively). Therefore, a multifactorial polygenic transfer mechanism was suggested. As a conclusion, the results of the studies performed in twin pairs and family studies cannot give a specific form of genetic inheritance; except the frequency of scoliosis in relatives has been shown to be decreased from first to third degrees.

2.5. Detection of Scoliosis

In the past, there was school screening program available for children between the ages of 11 and 14 (grade 5 to grade 9) to detect scoliosis in Canada. However, in 1979 and 1984 the Canadian Task Force refused the importance of the school screening to the detection of scoliosis, and the program was discontinued in Canada.

Scoliosis causes deformities of the spine and rib cage that present as postural distortions of the trunk. People notice scoliosis usually because of the cosmetic appearance. There are several ways that scoliosis may be detected:

1. by the family physician during routine examination
2. by parents who notice their child has:
 - a) poor or an unbalanced posture,
 - b) one shoulder appearing lower than the other
 - c) clothes that do not hang properly
 - d) one shoulder blade that appears more prominent than the other
 - e) uneven hips
3. by physical education teachers, sports and dance instructors.

One of the easiest ways to diagnose scoliosis is to do the forward bending test (Figure 2-14). From this test, the possible indicator is the asymmetry profile; at the

thoracic region one shoulder blade appears more prominent than the other while in the lumbar region rib cage rotation occurs. If a physician detects a significant asymmetry, the child will be referred to an orthopaedic specialist. Before making any decision on treatment by an orthopaedic specialist, a physical examination is performed to confirm that the child has scoliosis and to rule out other factors that may be involved. Also, the specialist may use a scoliometer to measure the rotation of the trunk. A scoliometer (Figure 2-15) is a spirit level that is placed horizontally upon the trunk while the subject is bent forward. According to the scoliometer developer Dr. William Bunnell, a 5° reading on the scoliometer relates approximately to a 20° Cobb angle curve. Low-dose X-rays are then taken so that the orthopaedic specialist can view the spinal curvature.

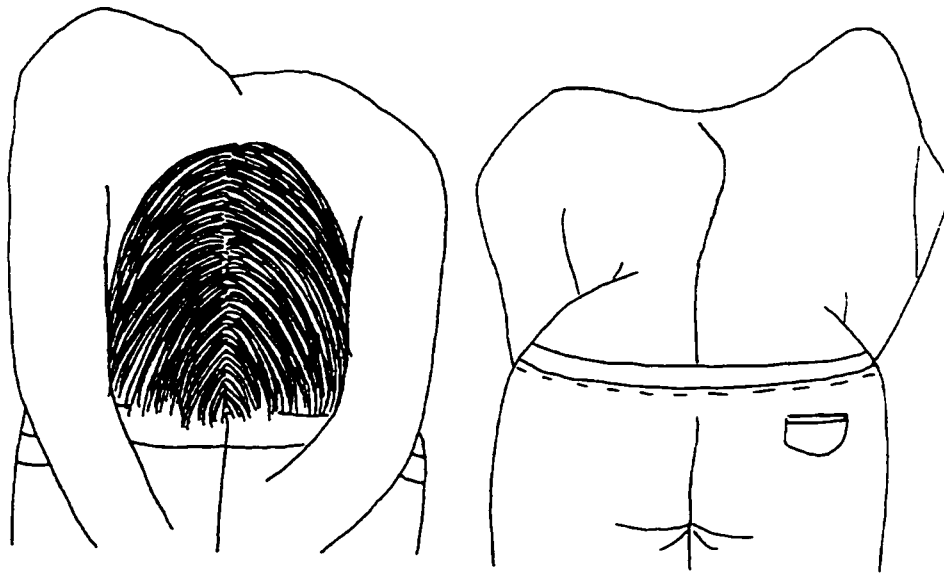
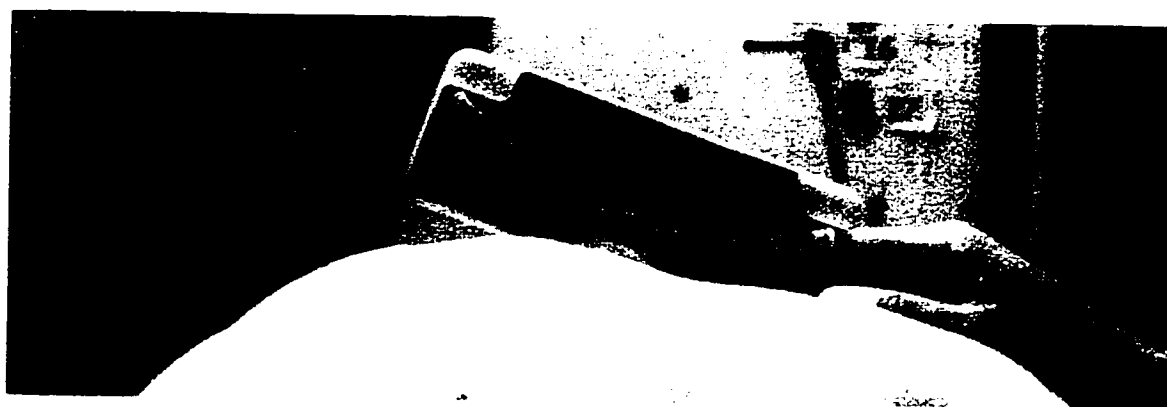


Figure 2-14. Forward bending test.



(a)



(b)

Figure 2-15. a) A scoliometer and b) trunk rotation measurement.

2.6. Treatment of Scoliosis

There are three treatment regimes for scoliosis. If the curvature is under 25° and the patient is perceived to be at risk of progression, a regular examination is required. Monitoring is done by regular radiographs and surface measurements. In most cases, the scoliosis does not progress to the point where treatment is required. However, if the curve is progressive and the Cobb angle increases beyond 25 degrees, non-surgical treatment or surgical treatment may be required. Surgical treatment is reserved for the severe progressive case when the curve is at least 45 degrees. Orthopaedic specialists have developed their own criteria of when to treat and which treatment approach to take based on empirical information and the perceived risk of further progression of the curvature.

2.6.1. Non-surgical Treatment

Nowadays, bracing is the most common form of non-surgical treatment for scoliosis. The brace action includes passive and active components. The passive component is the mechanical support by the brace, and the active component is the patient pulling the body away from pressure sites imposed by the brace. The active component has been suggested to be more important to improve the spinal curvature and cosmetic appearance. Therefore, many researchers have employed a non-mechanical approach for the treatment of scoliosis. The following two sections describe and review brace treatment and the physiotherapy approach for the treatment of scoliosis.

2.6.1.a. Brace Treatment

Spinal bracing was first attempted during the Middle Ages when the wealthy social groups instructed armorers to mold metal corsets in an attempt to halt scoliosis progression. At that time, braces were merely passive devices and did not incorporate any active corrective principle. In 1954 Blount and Schmidt developed the Milwaukee brace to treat progressive scoliosis. Figure 2-16a shows the back view of a Milwaukee brace. The Milwaukee brace incorporated active correction by encouraging the brace wearer to pull away from the thoracic pad. By 1976, the Milwaukee brace was the most frequently used brace in the United States for non-operative treatment of IS [72]. The design and construction of the Milwaukee brace has evolved away from the initial concept of mandibular and occipital distraction. It emphasized passive correction as well as active derotation with a medially directed force. The shoulder slings, thoracic pads, and the lumbar pads of the brace can apply forces of different magnitudes, in different directions, and at different points to correct single, double, and triple curves. The conventional Milwaukee brace has undergone many modifications [73]. In 1971 Hall and Miller modified the Milwaukee brace design to develop the Boston brace. The most dramatic change was the removal of the metal uprights.

The Boston brace is constructed from a prefabricated polypropylene pelvic module. No individual plaster mold is required. The module is trimmed into a "girdle" and shaped to the needs of an individual patient. The prefabricated module has a hard polypropylene plastic shell with a soft foam polyethylene lining providing a close fit to the pelvis and a "grip" which is used as a foundation for applying forces to the spine. Figure 2-16b shows the back view of a Boston brace. The symmetry of the inner surface

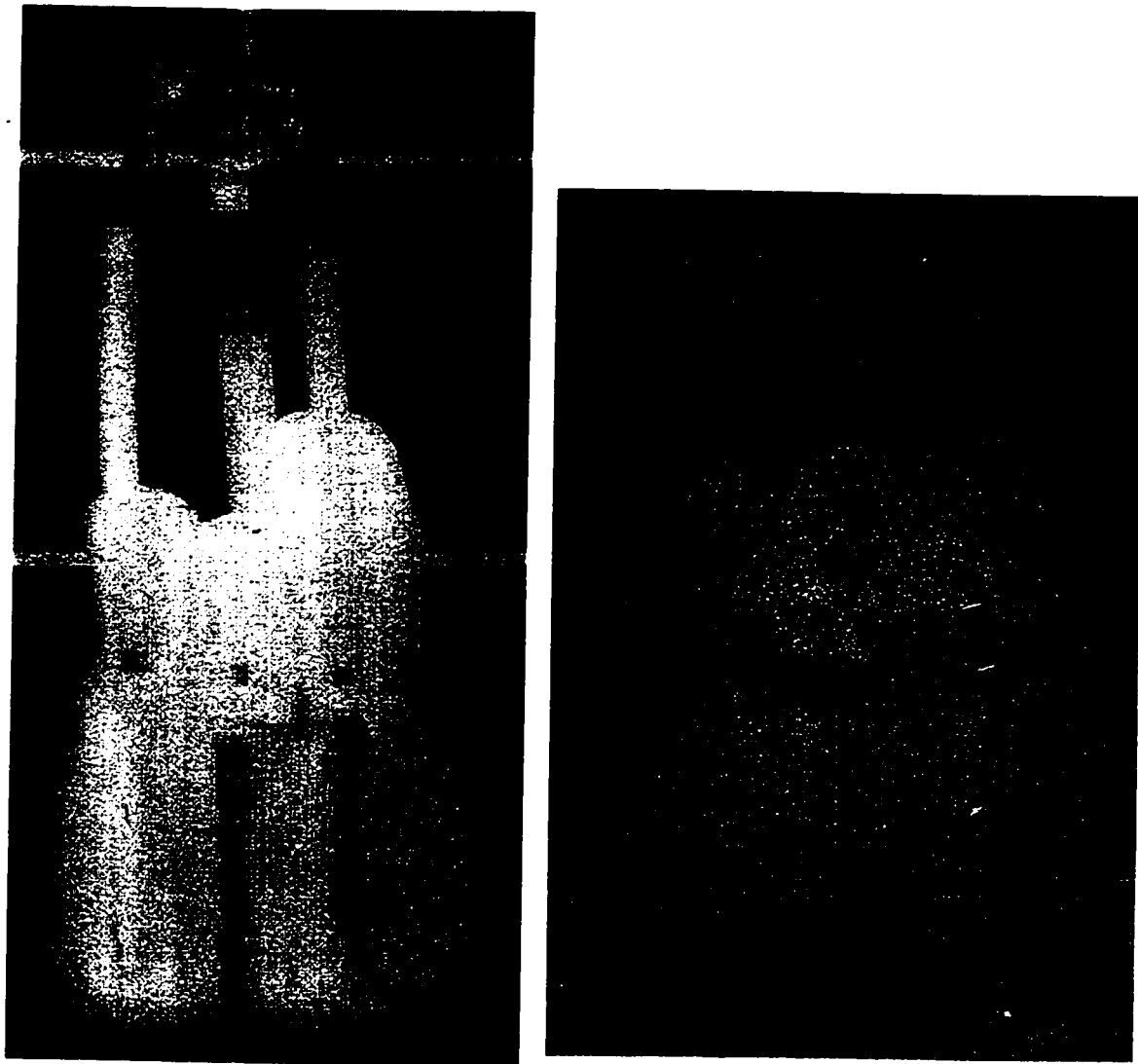
of the orthosis is altered only by the placement of pads which make contact with chosen areas of the patient's torso. These pads provide mechanical support for the spine, and their positions depend on the severity of rib cage rotation and the location of the curve. The biomechanical concept of the bracing system is to provide three-dimensional dynamic correction of the spine. This is achieved by using a prefabricated polypropylene module lined with polyethylene foam. The anatomic configuration of the module provides 15° of lumbar flexion, increased anterior abdominal force, fixation at the waist, and lateral torso containment [74].

Both the Milwaukee and Boston braces provide mechanical support for the spine by means of pressure pads. The type of brace chosen depends on the location of the curve. The Boston brace is most effective in controlling curves in the lumbar and thoracolumbar regions whereas the Milwaukee brace is favored for the thoracic curves. Today, the Boston brace is favored because their low profile permits them to be hidden from view with appropriate clothing.

The primary purpose of brace treatment is to prevent further increase of the spinal deviation during the high risk period of the adolescent growth spurt. The average length of time a patient wears a brace is about three years, with the brace worn full time (23 hours per day) for about 18-months. In curve correction, the active brace action by pulling the body away from pressure sites imposed by the brace is claimed to be more important [75].

Although bracing is currently favored as a non-surgical treatment for scoliosis, the actual effectiveness of the brace treatment is still uncertain [76, 77]. In 1992, Dansereau *et al.* [78] indicated that Boston brace didn't correct the three dimensional thoracic spinal

deformity, but it aggravated the deformity in the sagittal plane. In 1997, Aubin *et al.* [79] also reported that brace loads were not applied in an optimal way to correct the 3-D deformities associated with thoracic scoliosis. Therefore, further investigations or improvement in brace design must be done.



(a)

(b)

Figure 2-16. Back view of a) a Milwaukee brace and b) a Boston brace.

2.6.1.b. The Physiotherapy Approach for the Treatment of Scoliosis

Brace treatment is thought to rely on either the mechanical support by a brace (passive) or by pulling the body away from pressure sites imposed by the brace (active) [75]. In the passive case, true forces imposed by the braces on the trunk are considered the key to successful treatment. While in the active case, the brace simply provides a reference used by the patient to react against; it is the self muscular control to treat scoliosis. A technique described by Schroth *et al.* [80] called “rotational breathing” attempts to correct actively body shape. This technique is mainly to remind the patient to create the opposite appearance to what the scoliotic body looks like. For example, if one side of the ribs have sunk inwards and downward, patients will try to move the ribs outside and upwards when they breathe in. Wesis *et al.* [81] suggested that Schroth’s method is suitable for prevention and treatment of secondary functional impairment as well as for treatment of scoliosis related pain. Another group of researchers, Dworkin *et al.* [82], suggested that behavioral principles and therapeutic theory help scoliotic children correct their spinal deformities as well as cosmetic appearances. Dworkin’s group used the apparatus called “Micro-Straight” to treat children with scoliosis. The micro-straight detects the length of the trunk and compares it to a pre-set value. If the length of the trunk is different from the preset value and lasts longer than 20 seconds, a beep tone will alert the patient to correct the posture. The results presented by Dworkin *et al.* showed that this approach was very successful.

Both treatments approach rely less on mechanical correction, and more on providing appropriate feedback to the wearer. These studies suggest that patients are able to transfer the learned corrected posture to a long-term improvement of trunk deformity.

The mechanism for this may be that continuous muscle training results in a re-education of the scoliotic posture into a corrected balance posture. Furthermore, El-Sayyad *et al.* [83] also showed that exercise alone can decrease the curvature of the spine.

2.6.2. Surgical Treatment

There are three fundamental goals of spinal surgery: 1) to gain as much safe correction of the deformity as possible, 2) to produce a solid spinal fusion of the curve and 3) to bring the spine into a more balanced position. In spinal surgical treatment, three distinct mechanisms are used for curve correction: distraction, segment fixation and segment rotation. The traditional mechanism of achieving correction of scoliosis has been to generate a corrective moment at the spinal segments involved in the curve. All the instrumentation systems, such as the Allan Jack [84], the Harrington system [85], the Luque system [86, 87] and the Dwyer *et al.* system [88] generate a corrective moment across the scoliosis curve. The term “instrumentation” refers to a variety of devices such as rods, hooks, wires and screws (Figure 2-17), which are used to hold the correction of the spine in as normal an alignment as possible while the bone fusion heals. For example, the Harrington system consists of a distraction rod placed on the concave side of the curve, and a compression device applied to the convex side for the dynamic correction of scoliosis during surgery. However, the improvements due to the Harrington system are restricted to the frontal plane only. Techniques which attempts to ‘derotate’ the spine were put forth by Cotrel and Dubousset. The mechanism of action by which the Cotrel-Dubousset (C-D) system corrects a curve is distinctly different from that of the Harrington or the Luque systems. The major correcting mechanism in the Cotrel-

Dubousset (C-D) system [89] is the rotation of the rod which deliberately links frontal and sagittal plane correction. The C-D system or similar derotational systems are now the standard treatment in many centers for treating adolescent idiopathic scoliosis.

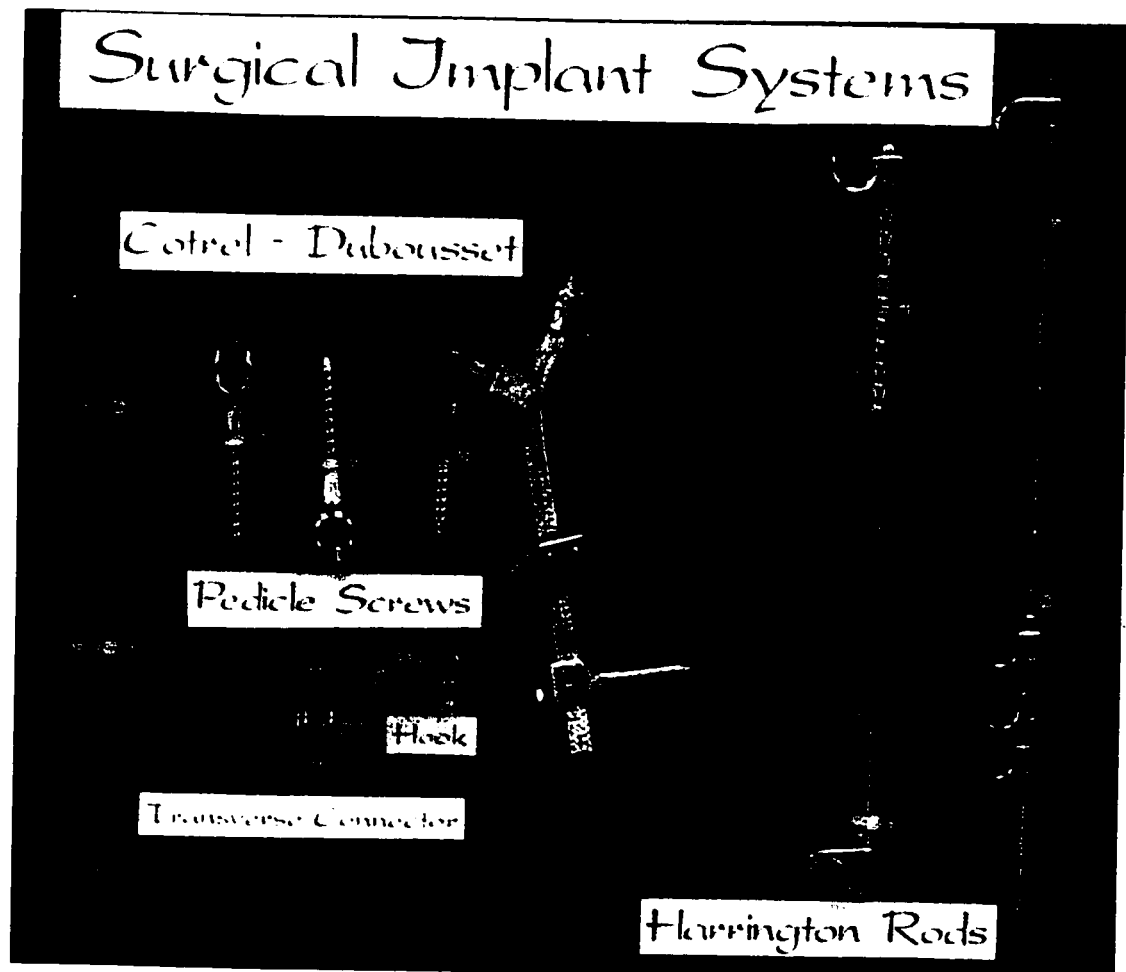


Figure 2-17. The surgical implant instrumentation.

2.6.3. Summary

In general there are some guidelines that can be used to decide which treatment method is suitable for people who have idiopathic scoliosis. The guidelines are based on age, type of curve, location of curve, severity, and skeleton maturity. However, orthopaedic specialists usually like to set the criteria and based on their experience to make recommendations to patients. The final treatment method is still chosen by the families and the scoliotic children.

2.7. Literature Review of Three-Dimensional Posture Measurement Systems and Transducers

Many methods for human posture measurement have been developed, including goniometry, photogrammetry, optoelectric analysis, video analysis, sonic analysis etc. The principles of these methods have been summarized in Hsiao and Keyserling [92]. These methods have been widely used in the fields of orthopaedics and biomechanics and most of them have the following disadvantages:

- i) a laboratory environment is required,
- ii) technicians are necessary to record data,
- iii) analysis time is long, and
- iv) set up charge is expensive.

Furthermore, many techniques have been used to measure three-dimensional surfaces. Gyroscope and magnetic sensors, both are commercially available [93], are the two well-known devices to measure tilt angle. They are small and light, but they are very sensitive to mechanical vibration and thus are not suitable for measuring human posture during daily activities. Kato *et al.* [94] developed a photoelectric inclination sensor, which consists of a LED, a hemispherical spirit level, and a photodiode array, to measure the shape of any 3-D object. This sensor uses the LED to project light on the bubble in the spirit level. The shadow is then projected onto the surface of the array composed of four equivalent p-n junction diodes, isolated by a cross on a wafer. By using a circular model for the shadow, the tilt angle and the direction in a two-dimensional plane can be obtained. However, this sensor is large (50mm x 50mm x 50mm) and accurate only

when the tilt angle is less than 10 degrees. The error increases when the tilt angle increases because the shadow on the photodiode array is no longer circular, but elliptical.

Tanaka *et al.* [95] developed a portable instrument for long-term ambulatory monitoring of posture change using miniature electro-magnetic inclinometers. The size of the inclinometer is small (length=30mm, radius=13mm), and the dimensions of the computer unit are 33mm x 68mm x 110mm. The weight of the whole system is only 200g, and it is battery-powered. However, the angular resolution of this system is 12 degrees and it can only obtain two-dimensional information. Therefore, this system is only good for monitoring human posture in these four states: standing, walking, sitting and lying.

In addition, there are some commercially available products that have been designed mainly for three-dimensional measurements, for example, the 6 degrees-of-freedom tracker systems from Ascension Technology Corporation and the 3Space Motion Tracking Systems from Polhemus. All those systems consist of one transmitter and number of receivers. To do a measurement, the transmitter is fixed in one position and the receiver is moved to a desired location. Then, the position and orientation of the receiver relative to the transmitter can be determined. The distance and orientation parameters are determined by using the field strength of the received signals. The highest accuracy of these systems is 0.03 inch RMS in distance and 0.15° RMS in angle, and the resolution is 0.0002inch/inch range and 0.025°, respectively. However, these products are designed to take measurements in laboratory environments and they are not easily portable due to their size, weight and dependency on AC power. Figure 2-18 is a photograph of one of the systems that was developed by Ascension Technology

Corporation. These commercial systems are also not designed to provide feedback signals to subjects. The size of the controller unit is about the same as that of a laptop computer, and the weight of the transmitter is 1.5 kg.

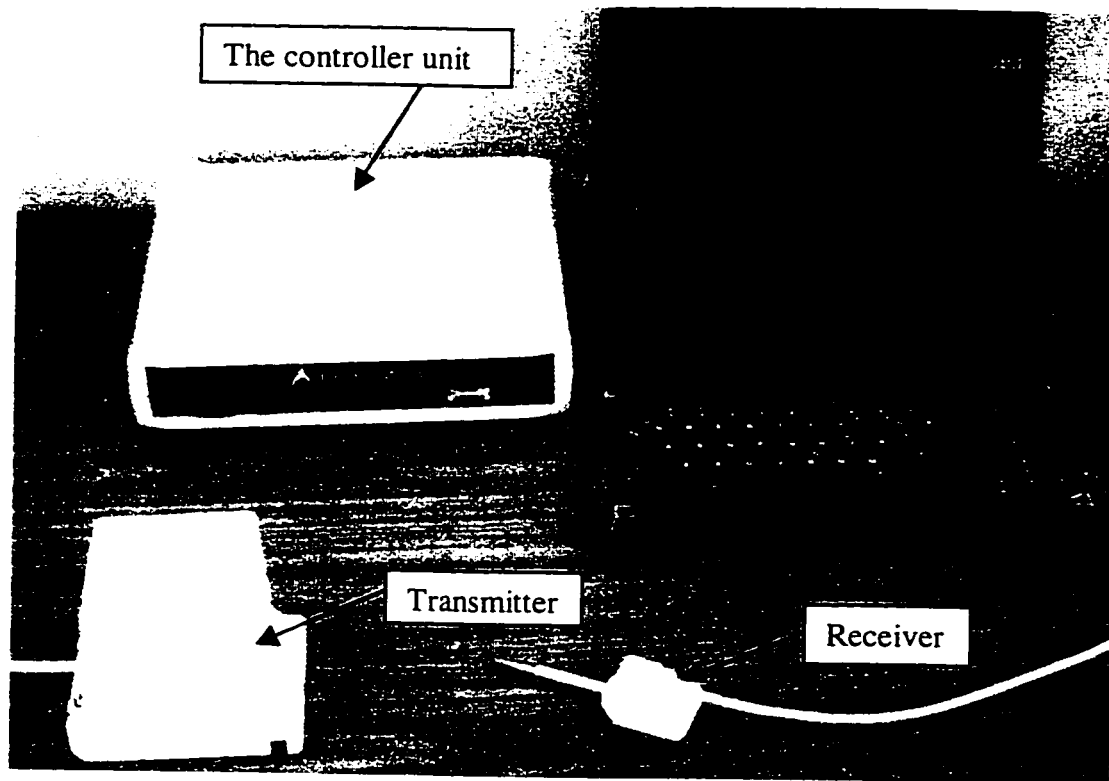


Figure 2-18. A Flock of Bird system developed by Ascension Technology Corporation.

2.8. Literature Review of Electromagnetic Systems

Low frequency quasi-static magnetic fields have been used for detecting position and orientation for many years. Most EM techniques are based upon free-space field geometry. In 1962, Kalmus [99] used phase-quadrature excitation techniques to determine position and orientation in two dimensions. Kalmus's system was designed to assist vehicles in following one another. The dimensions of the transmitter and receivers were the same, 12cm x 12cm x 2.5cm, and the power consumption of the system was 24W (12V x 2A). In 1979, Raab *et al.* [100] presented the principles and theory on how to calculate the position and orientation of a three-axis transmitter-receiver magnetic system. Also, Raab *et al.* developed a system to help aircraft on landing and take-off. The size, weight and power consumption of the system was huge. The weight of the transmitter was 4.5kg and the power consumption of the system was 400W. To determine the position of the receiver, the first position of the receiver had to be known. Then, the system tracked the position and orientation of a receiver by continuously determining small changes in positions. Therefore, motion on the receivers was necessary. In 1988, An *et al.* [101] used a three-axis transmitter and a three-axis receiver system to determine both the position and orientation of a transmitter relative to receivers. The system consisted of three components: a system electronic unit, a source, and a sensor. The dimensions of the source and sensor were 10cm x 10cm x 10cm and 3cm x 3cm x 2cm, respectively. The power consumption of the system was 20W (5Vx4A). AC power was required to operate the system. Furthermore, there are commercially available systems that use a three-axis transmitter and three-axis receivers systems for kinesiological studies: such as human back movement [102], respiratory

measurement [103], and wrist kinematic measurement [104]. However, all these measurements are restricted to laboratory conditions because those available systems are not portable due to their size, weight and large power consumption. Also, to do a measurement, those commercial systems must be connected to personal computers and operated by technicians. In addition, other electromagnetic systems have been used in mining [107] or underground services [108], but they all required high-power. Consequently, portable electromagnetic measurement systems require significant research to attain the low-power requirements.

3. TRUNK DISTORTION IN ADOLESCENT IDIOPATHIC SCOLIOSIS¹

This chapter reports a literature review of measurement methods to assess trunk deformities. From this review seven topographical features that contribute to the trunk deformity are identified. A video imaging method has been developed to measure those seven topographical features. Also, a study to determine the reliability and repeatability of measuring the cosmetic features is reported.

3.1. Introduction

Scoliosis causes deformities of the spine and rib cage that present as postural distortions of the trunk. To diagnosis and assess of scoliosis, either the internal alignment or the cosmetic appearance can be used as the base to evaluate the distortion. To exam the internal alignment, a radiograph is taken and the Cobb angle is measured. However, the Cobb angle itself only represents a single plane measurement of the internal spinal alignment, it does not truly represent the three-dimensional trunk distortion. To assess cosmetic appearance, clinicians have had to rely on subjective measures such as patients or families satisfaction. Although researchers know that an objective method is important to evaluate the treatment outcome, very little work has been done to develop tools for assessing trunk distortion in children with spinal deformities. To develop an objective method to assess trunk deformities, topographical features that significantly

¹ The material in this chapter has been published in : V. J. Raso, E. Lou, D. L. Hill, J. K. Mahood, M. J. Moreau, and N. G. Durdle, "Trunk Distortion in Adolescent Idiopathic Scoliosis", *Journal of Pediatric Orthopaedics*, vol. 18, no. 3, 1998, and in : E. Lou, D. L. Hill, V. J. Raso, N. G. Durdle and J. K. Mahood, "An objective Measurement of Trunk Deformity", the Transactions of the 2nd combined meeting of the Orthopaedic Research Societies of U.S.A., Japan, Canada and Europe, p.242, 1995.

contribute to the overall impression must be defined. A study from Mahood *et al.* [82] reported that seven topographical features contribute 85% of the overall impression of trunk deformity. A further study [109] on the perception of trunk deformities reported that among those seven topographical features, three are significant predictors of cosmetic impression. Furthermore, if these significant topographical features can be reliably and repeatably measured, it would permit the objective assessment of changes to trunk deformity and possibly a basis for the treatment of trunk deformity. Therefore, a study [110] was done to determine the reliability and repeatability of the measurement method.

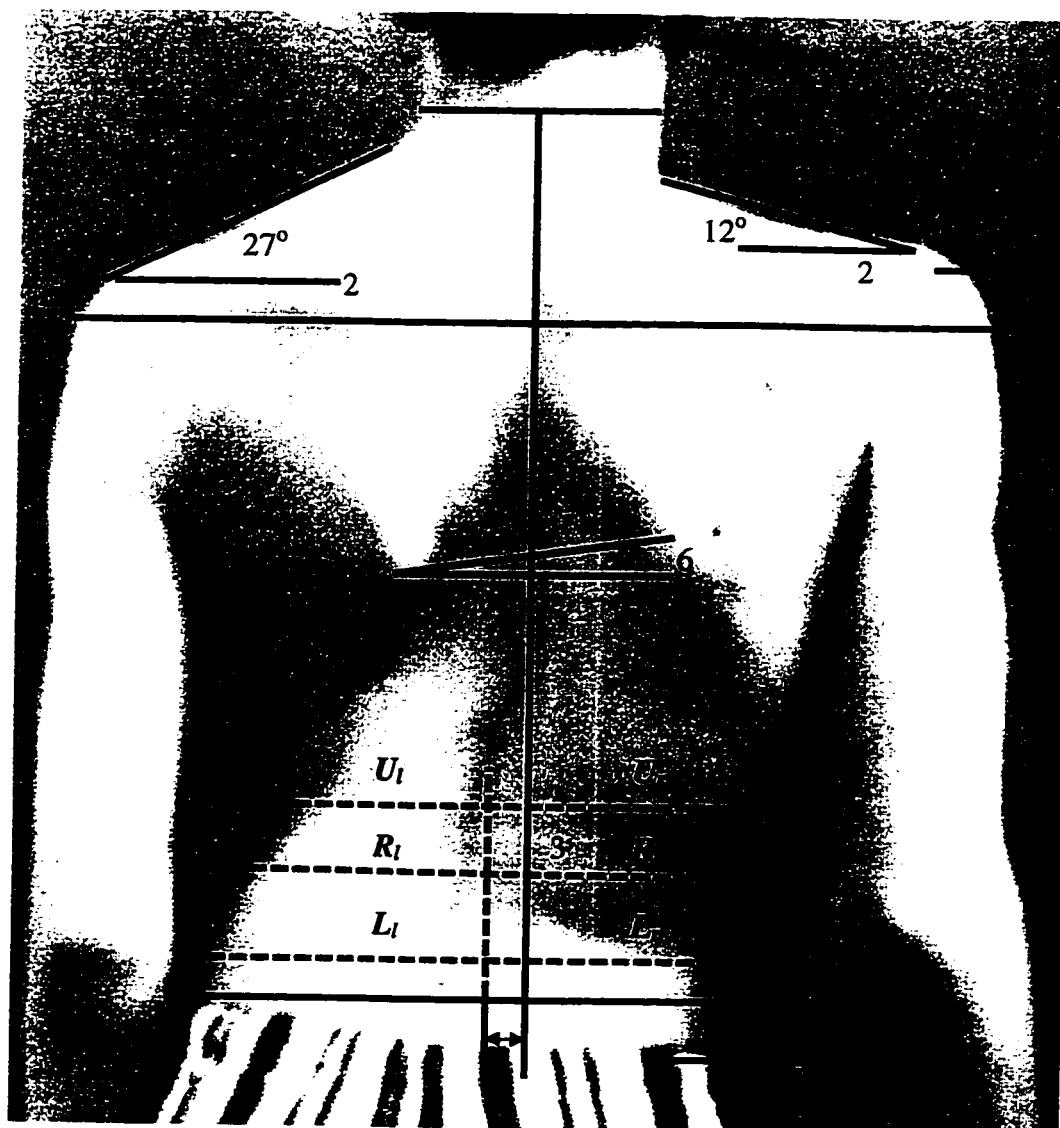
3.2. Literature Review of Methods for Trunk Assessments

Moiré (meaning watered silk) fringe technique was applied to measure contour changes on the backs of patients with scoliosis in 1970's. At that time researchers started to develop and enhance that technique and hoped that it might be a supplement or a substitute of radiographs. However, in the 1980's moiré techniques had proven to be unreliable and sensitive to patient position [96]. A new method developed by Turner-Smith *et al.* [96] called Integrated Shape Imaging System (ISIS) had met with limited clinical success. But the reliability of the ISIS method still depended on how well the operator could locate reference marks over the anatomical landmarks. Very little work has been done to develop research tools for assessing trunk distortion in children with spinal deformities. In the absence of such research, clinicians have had to rely on personal recollections and the impressions from patients and their families. These approaches do not provide objective measures of trunk deformities.

To develop an objective method to assess trunk deformity, topographical features that contribute to trunk deformity must be identified first. In 1993, Theologis *et al.* [97] developed a cosmetic spinal score based upon parameters from the ISIS scan to assess trunk deformities. From their study they reported that the most important feature that contribute to trunk deformities was the rib prominence. However, in 1995 Mahood *et al.* [82] reported that 85% of the overall impression of trunk deformity were account on seven topographical features: shoulder height and shoulder angle differences, pelvis asymmetry, decompensation, waist crease, scapular height difference and waist asymmetry. A video measurement method [110] was then developed to measure the seven topographical features. Hill *et al.* [98] used the seven topographical features to develop a cosmetic score method to represent the surface deformity due to scoliosis. The cosmetic score was then used as an objective method to assess trunk distortion. A further study [109] to determine the perception of trunk deformities was carried out again and the results showed that among these seven cosmetic features, scapular asymmetry, shoulder angle asymmetry and waist asymmetry were the most significant predictors of cosmetic impression.

3.3. Seven Topographical Features

The details of the seven cosmetic features are described in the following with reference to Figure 3-1.



Cosmetic features:

1. Shoulder height difference
2. Shoulder angle difference
3. Waist asymmetry
4. Decompensation
5. Waist crease
6. Scapula asymmetry
7. Pelvis asymmetry

Figure 3-1. Cosmetic features of a scoliotic trunk.

3.3.1. Shoulder Height Difference

Shoulder height difference is the difference between the height of the right shoulder and left shoulder. Referring to Figure 3-1, a horizontal line is drawn at the height of the right shoulder as well as at the height of the left shoulder. The vertical distance between these two lines is the difference in shoulder height.

3.3.2. Shoulder Angle Difference

Shoulder angle difference is the difference between the angle of the right shoulder and left shoulder. Generally the slope of the right shoulder will be less than the left shoulder because right thoracic curve is more common than the left thoracic.

3.3.3. Waist Asymmetry

Waist asymmetry is an index to measure how much the waist is shifted. In a severe case of scoliosis, the waist region may be noticeably “swept”, either to the right or to the left. This sweeping is primarily due to the scoliotic curve in the lower part of the trunk. The waist asymmetry scores ranges from 0 to 2 with 1 being perfect asymmetry. A value less than 1 reflects sweeping to the right whereas a value greater than 1 represents sweeping to the left.

Waist asymmetry (W.A) is made up of six parameters U_l , U_r , R_l , R_r , L_l and L_r and its expression is $W.A = \frac{R_l U_l U_r}{R_r L_l L_r}$.

To determine these six parameters, a reference vertical line is drawn from the center of the pelvis. A horizontal line is drawn at the waist - the minimum horizontal

distance in the waist region. The horizontal distances from the reference to the body edges are R_l (*Reference left*) and R_r (*Reference right*). Horizontal lines drawn at 10% of the trunk length above and below the waist are referred as *Upper* (U_l , U_r for left and right) and *Lower* (L_l , L_r for left and right) respectively. Trunk length is the vertical distance from the pelvis to the shoulder.

3.3.4. Decompensation

Decompensation is a measure of balance - how far the head is shifted away from the center of the pelvis. To measure decompensation, a vertical line is drawn from the center of the neck and another vertical line is drawn from the center of the pelvis. The horizontal distance between these two lines is the decompensation.

3.3.5. Waist Crease

Waist crease is a marked folding of the skin which occurs in the severe forms of scoliosis. The skin can either be on the left or right side. The crease or fold starts from the edge of the body just below the rib cage and radiates upward towards the center of the back.

3.3.6. Scapular Asymmetry

One shoulder blade or scapular may be more prominent with increased scoliosis. As well, the shoulder blades may be at different heights due to the curve in the upper part of the back. The high points on the right and left scapula are marked off. The scapula angle is the angle made with these points and the horizontal.

3.3.7. Pelvis Asymmetry

Pelvis asymmetry is measured much like the shoulder height - mark horizontal lines from the right and left pelvis. The height difference between the left and right pelvis is the pelvis asymmetry. When clothing covers the pelvis, the pelvis height cannot be measured. Clothing may give you an indication of the pelvis height difference in that the subjects are standing with both feet at the same height and thus their pants should be level.

3.4. Reliability and Repeatability of Trunk Measurements

In order to use the cosmetic scores to determine the treatment outcomes on scoliosis, a study to determine the reliability and repeatability of trunk measurements on the seven topographical features were done.

3.4.1. Objective

The objective of this study was to determine the reliability and repeatability of the video image method that used to measure the seven topographical features.

3.4.2. Materials and Methods

Twenty-five females, age 13.1 ± 1.6 years, with scoliosis major in right thoracic curves (Cobb angle: $48.8^\circ \pm 18.8^\circ$, range: 11° to 80°) were examined. None of the subjects had had previous spinal surgery. Subjects wore a hospital gown which opened at the back were arranged to take the photograph in a relaxed standing position. Subjects were instructed to remove their shoes and to stand in front of a JVC SK310U video

camera. Figure 3-2 shows the set up for taking the images. The camera was positioned so that the image of 640 by 480 mm was centered about the midpoint of the back. Just before the picture was taken, subjects were instructed to inhale and hold their breath. Some of the subjects were free standing, but some of them used a chariot to guide the position. A Scion Image Capture II frame grabber on a Macintosh was used to acquire a single 8 bit grey scale image of 640 by 480 picture elements. All the cosmetic parameters were measured from the images by using the program IMAGE 1.59 (National Institutes of Health, USA).

Two examiners measured the images of twenty-five subjects twice to get two sets of data. To blind the examiners, subjects were labeled as 1-25. The examiners waited a week between repetitions to minimize bias. The first set of data from each examiner were compared with each other. Also, the first set of data for both examiners were compared to their second set of data.

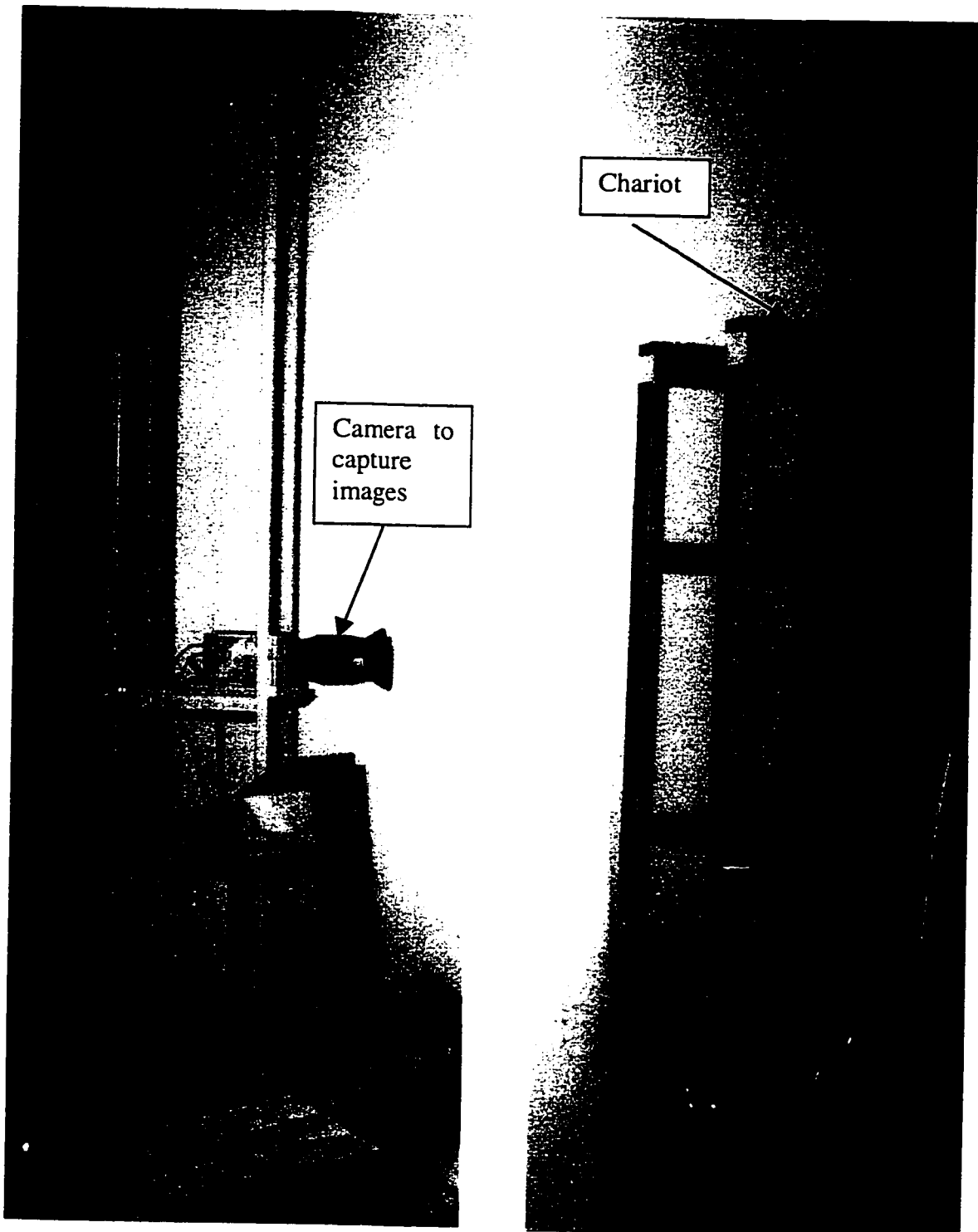


Figure 3-2. The set up at the Glenrose hospital for taking images.

3.4.3. Results and Discussion

All the cosmetic parameters, such as the waist asymmetry index, the decompensation, the pelvis asymmetry, the shoulder height difference, the right shoulder angle, the left shoulder angle, the scapular asymmetry and the waist crease, were measured from the twenty five images. Table 3-1 shows the summary of the results on the repeatability and the reliability of the measurements made by both examiners. There was no significant effect due to examiners or to repetitions, but the effect due to posture control was very significant. Critical differences were considered to be $\pm 5^\circ$ for the shoulder angles, $\pm 3^\circ$ scapular asymmetry, ± 0.1 for the waist asymmetry index and $\pm 5\text{mm}$ for the distance measurements. The worst result was for scapular asymmetry for which only 59% of the measurements were within $\pm 3^\circ$. Also, the repeatability on measuring scapular asymmetry by judge 1 and judge 2 was 72% and 67%, respectively. Judges measured this feature with the least confidence. In addition, by comparing examiner 1 with examiner 2, 76% of the total measurements were within the critical differences. Therefore, it was believed that most of the topographical features were able to measure reliably and repeatably.

Table 3-1. Summary of the Reproducibility of Trunk Measurements.

	Judge 1 Trial 1 vs. Trial 2	Judge 1 (Trial 1) vs. Judge 2 (Trial 1)	Judge 2 Trial 1 vs. Trial 2
Wai (± 0.1)	84%	88%	88%
Decom. (± 5 mm)	80%	68%	92%
Pelvis Asy. (± 5 mm)	84%	60%	84%
Shoulder Height diff. (± 5 mm)	84%	80%	88%
R. Shoulder Ang. ($\pm 5^\circ$)	76%	80%	96%
L. Shoulder Ang. ($\pm 5^\circ$)	96%	84%	96%
Scapular Asy. ($\pm 3^\circ$)	72%	59%	67%
Waist Crease	88%	88%	88%

3.5. Summary

From the literature review of trunk measurements of scoliosis, seven topographical features that contribute to trunk deformities were identified. A study by using a video image method to measure those topographical features was done. The results of that study showed that most of the topographical features of the trunk that contribute to the perception of deformity can be measured reliably and objectively. Consequently, the reproducible measurements would permit the objective assessment of changes to trunk deformity.

4. ELECTROMAGNETIC THEORY AND MEASUREMENT OF THE MAGNETIC FIELD DUE TO A MULTITURN SQUARE LOOP²

This chapter provides the theoretical basis and experimental validation for the development of electromagnetic system to measure changes in topographical features. The designed EM system consists of one transmitter and two receivers. Experiments have been carried out to investigate the effect of ferrite cores inside the transmitter and a receiver. Also, due to the cube-shaped of both the transmitter and receivers, an equation has been derived to show that an electromagnetic field generated by a square loop is the same as that from a circular loop as long as the ratio between the size of the square loop and the distance between the transmitter and the receiver is 1 to 7.5. Theoretical and experimental analyses to verify the derived equations have been done. An algorithm has been developed to calculate position and orientation of a receiver relative to the transmitter.

4.1. Introduction

Low frequency quasi-static magnetic fields have been used for detecting position and orientation for many years. Electromagnetic systems based on this technique usually consists of one transmitter and number of receivers. Position and orientation of a receiver relative to the transmitter is determined by the field strength of received signals. Electromagnetic receivers and transmitters are usually formed by winding magnetic wires

² Material in this chapter has been accepted to be published - E. Lou, N. G. Durdle, V. J. Raso, and D. L. Hill, "Measurement of the Magnetic Field in the Near-Field Region and Self-inductance in Free Space Due to a Multiturn Square-Loop", IEE Proceedings – Science Measurement and Technology, vol. 144, no.6, pp. 252-256, 1997.

around ferrite rods or by winding three orthogonal multiturn circular loops concentrically in free space. For those systems with ferrite rods, the power consumption is moderate (~20W), but the size is quite large. For those systems with air core, the size is smaller, but the power consumption is significant (> 40W). Therefore, an innovative approach using 3-axis coil transmitter and receivers has been developed. The size of the transmitter and receivers also depends upon the size of wire, the type of ferrite cores, the shape, and the number of turns of wire along each axis.

4.2. Design Procedures

To design small-size 3-axis coil transmitter and receiver units, ferrite cores were used to increase the sensitivity [105] for both the transmitter and the receiver units. First of all, both the transmitter and receiver units were designed to be cube-shaped because a cube-shaped holder was easy to hold. Plastic cube holders, with two different dimensions - one is 9mm on each size and the other is 13mm - were designed to allow magnetic wires to be wound in each direction. A ferrite cube (each side 7mm) cut from a ferrite rod (Amidon, California) (diameter 9mm) was inserted into the center of the smaller plastic holder (assumed to be a receiver). Ferrite discs cut from the ferrite rod with thickness, 5mm, were inserted into the six faces of the bigger holder (assumed to be a transmitter). Figure 4-1 shows the outline of the smaller plastic holder and a ferrite cube. Figure 4-2 shows the outline of the larger plastic holder and a ferrite disc.

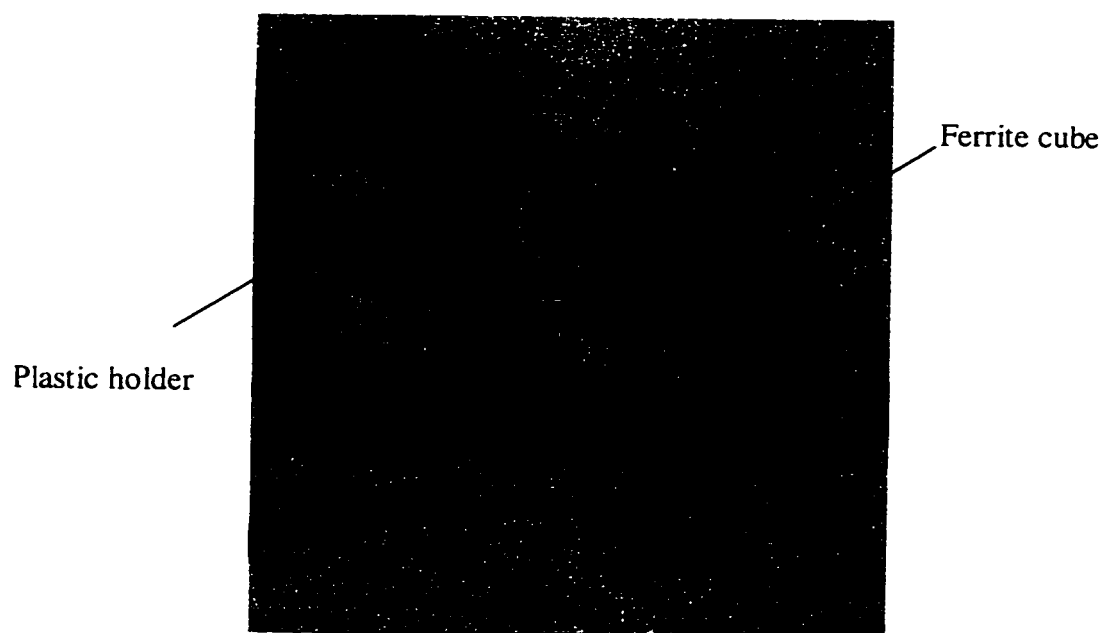


Figure 4-1. The outline of the smaller plastic holder with ferrite cube.

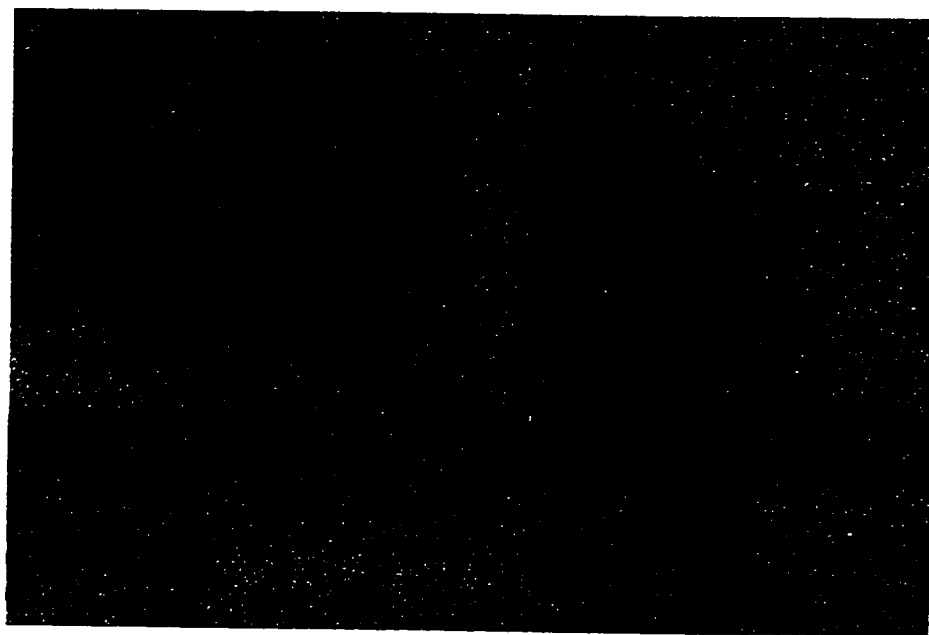


Figure 4-2. The outline of the larger plastic holder with ferrite disc.

4.3. Determination of Gain Factor due to Ferrite Cores

The purpose of placing ferrite cube or discs in the center of the plastic holder was to increase the permeability of the transmitter and receiver coils and this resulted in amplifying the transmitted and received signals. The amplification of the signals depended on the properties of the ferrite core. According to the data sheet of the ferrite rod from the manufacturer, the permeability of the ferrite core area depended on the number of turns wound around the ferrite, the length of the ferrite, and the size of the winding wire. To determine the actual gain factor due to the ferrite cube or the ferrite discs, an experiment was carried out. The measured gain factor would be used in the theoretical analysis.

To investigate the gain factors due to the ferrite cube and ferrite discs, four sensory units were built. The four sensory units were divided into two sets; each set contained one large and one small holder. The first set had ferrite cores inside both of the holders while the second set had no ferrite cores. Eight hundred turns of 36 AWG wire ($\rho = 1.36\Omega/\text{m}$) were wound on the larger holders, while five hundred turns of 38 AWG wire ($\rho = 2.13\Omega/\text{m}$) were wound on the smaller holders. Since, the inductance of a multiturn coil is directly proportional to the permeability of the free space or the material that is wound around by the magnetic wires, gain factors due to the ferrite cores inside the cube holders can be determined from their inductances. For the larger holders, the coil was unwound 30 turns at a time and the inductance was measured using the DM27XT series multimeter (Wavetek, San Diego). With 500 turns of wire remaining on the larger holder, the coil was unwound 50 turns at a time. Table 4-1 shows the measurements of the inductance with different number of turns of wire on both larger

holders. The average gain factor due to the ferrite discs was 1.62. A similar procedure was done on the smaller holders except only 20 turns were unwound each time. With 300 turns of wire remaining, 50 turns of wire were unwound from the smaller holders each time. Table 4-2 shows the measurements of the inductance as a function of the number of turns of wire on both smaller holders. The average gain factor due to the ferrite cube was 1.63. Hence, the gain factor due to the ferrite discs was approximately the same as that due to ferrite cube.

Table 4-1. The inductance of the larger holders with different number of turns of coil.

Number of turns	L1 (mH)	L2 (mH)	Gain Factor(L1/L2)
800	18.17	10.58	1.71
770	15.15	9.80	1.65
740	14.68	9.01	1.63
710	13.64	8.27	1.65
680	12.00	7.50	1.60
650	11.15	5.80	1.64
620	9.80	5.09	1.61
590	8.66	5.47	1.58
560	7.82	4.87	1.61
530	7.11	4.35	1.63
500	5.14	3.77	1.63
450	5.67	3.5	1.62
400	3.90	2.38	1.64
350	2.87	1.73	1.66
300	1.98	1.23	1.61
250	1.30	0.79	1.64
200	0.79	0.49	1.61
150	0.40	0.25	1.60
100	0.18	0.11	1.64
50	0.022	0.014	1.57

L1 represents the inductance of the larger holder that has ferrite discs.

L2 represents the inductance of the larger holder that only has the plastic holder.

Table 4-2. The inductance of the smaller holder with different number of turns of coil.

Number of turns	L1 (mH)	L2 (mH)	Gain Factor
500	4.36	2.79	1.56
480	4.00	2.55	1.57
460	3.74	2.33	1.61
440	3.37	2.12	1.59
420	3.10	1.92	1.61
400	2.67	1.67	1.60
380	2.45	1.48	1.66
360	2.18	1.31	1.66
340	1.89	1.16	1.62
320	1.68	1.02	1.65
300	1.40	0.87	1.61
250	0.91	0.55	1.65
200	0.55	0.33	1.69
150	0.30	0.18	1.67
100	0.10	0.06	1.67
50	0.02	0.01	1.64

L1 represents the inductance of the smaller holder that has ferrite cube.

L2 represents the inductance of the smaller holder that only has the plastic holder.

4.4. Theoretical Development and Experimental Results of Self-Inductance and Magnetic Field due to A Multiturn Square-Loop Coil

The equation to calculate the magnetic flux density generated from a circular current loop can be found in any electromagnetic textbooks. However, in this case, both the transmitter and receivers are cube-shaped. An equation that calculates a magnetic flux density generated from a multiturn square current loop must be derived. To derive the equation, some properties of the multiturn coils must be measured. Experiments have been carried out to arrive at the correct equation.

To measure the properties of two different sizes of 3-axis multiturn coils, the smaller holder was used for a receiver while the larger holder was used for a transmitter. Both the receiver and transmitter had either a ferrite cube or the ferrite discs in the center, respectively. Both of them had three orthogonal coils wound around. Coil-X was the most inner layer of the loops while Coil-Z was the outer layer of the loops. The average loop diameters of the transmitter in coil-X, -Y, -Z are 16.7, 18.0 and 18.7 mm, respectively. The average loop diameters of the receiver in coil-X, -Y, -Z are 10.8, 11.5 and 11.9 mm, respectively. The resistances of the transmitter in coil-X, -Y, -Z are 71.1, 74.7 and 78.7 ohms, and the inductances are 18.2, 19.1 and 19.0mH, respectively. The resistances of the receiver in coil-X, -Y, -Z are 46.5, 50.0 and 53.6 ohms, and the inductances are 4.43, 4.86 and 5.06mH, respectively. Each loop of the transmitter is in turn excited with a 10Vp-p driving signal identical in frequency and phase. A twelve-kilohertz sine wave signal was chosen because that particular frequency has minimum interference from other EM signals. The transmitter acts as a fixed magnetic-dipole transmitting antenna which produces a far-field component and a near-field component.

The near-field or quasi-static field component is dominant when the distance between the transmitter and the receiver is less than $\lambda/2\pi$ (where the wavelength $\lambda = 25$ km). The near-field component is frequency independent and decreases by the inverse cube of distance. For the transmitter, a series LC circuitry was used in which the quality factors Q_x , Q_y , and Q_z are 10.06, 10.13 and 10.19; for the receiver, a parallel LC circuit was used in which Q_x , Q_y , and Q_z are 7.18, 7.33 and 7.12.

4.4.1. Theoretical Analysis

To calculate the magnetic field generated by a square loop $abcd$ (Figure 4-3) to a point $P(R, \theta, \phi)$ (spherical coordinates), the vector magnetic potential \mathbf{A} is first calculated from:

$$\mathbf{A} = \frac{\mu_0 I}{4\pi} \oint_c \frac{d\mathbf{l}}{R} ; \quad (1)$$

where μ_0 is the permeability of free space, I is the current flowing in the loop.

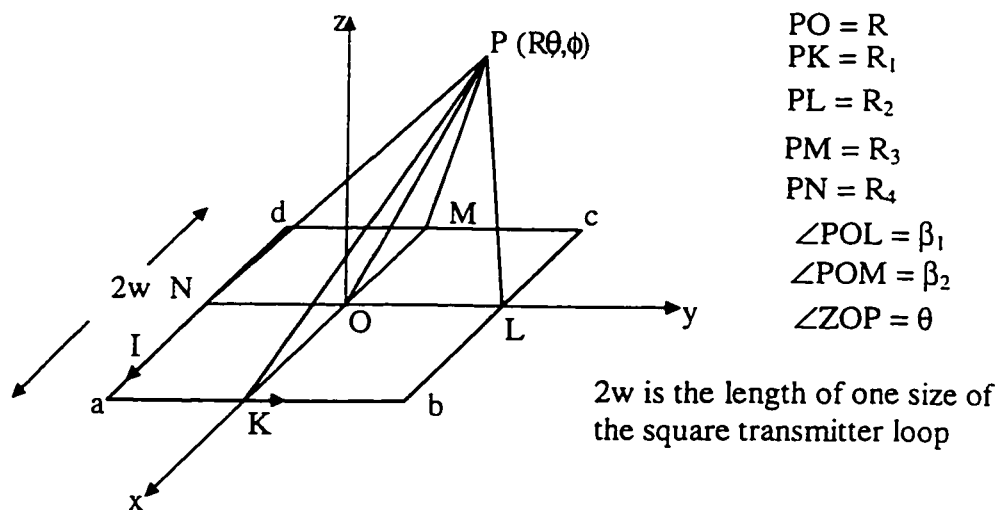


Figure 4-3. The position of the point P relative to the square loop of $abcd$.

Therefore, the vector magnetic potential \mathbf{A} from the square loop $abcd$ is:

$$\mathbf{A} = \frac{\mu_0 I}{4\pi} \int_0^{2w} \left[dx \left(\frac{1}{R_4} - \frac{1}{R_2} \right) \mathbf{a}_x + dy \left(\frac{1}{R_1} - \frac{1}{R_3} \right) \mathbf{a}_y \right], \quad (2)$$

where \mathbf{a}_x and \mathbf{a}_y are the unit vectors in x and y directions, respectively.

Using the law of cosines, the distances are derived as

$$R_1^2 = R^2 + w^2 + 2Rw \cos(\beta_2) \quad (3)$$

$$R_2^2 = R^2 + w^2 - 2Rw \cos(\beta_1) \quad (4)$$

$$R_3^2 = R^2 + w^2 - 2Rw \cos(\beta_2) \quad (5)$$

$$R_4^2 = R^2 + w^2 + 2Rw \cos(\beta_1), \quad (6)$$

where $R_1, R_2, R_3, R_4, w, \beta_1$ and β_2 are distances and angles which are defined in Figure

4-3. The angles β_1 and β_2 are related to the spherical coordinates as followings:

$$\cos(\beta_1) = \sin(\theta) \sin(\phi) \quad (7)$$

$$\cos(\beta_2) = -\sin(\theta) \cos(\phi) \quad (8)$$

In our implementation $R \approx 30\text{cm}$ and $w \approx 0.5\text{cm}$.

If it can assume $R \gg w$, apply the Taylor's series expansion and substituting equations

(3) - (6) into (2) gives

$$\mathbf{A} = \frac{-\mu_0 I}{4\pi R^2} (4w^2) [\cos(\beta_1) \mathbf{a}_x + \cos(\beta_2) \mathbf{a}_y] \quad (9)$$

Substituting (7) and (8) into (9) gives

$$\begin{aligned} \mathbf{A} &= \frac{-\mu_0 I}{4\pi R^2} (4w^2) [\sin(\theta) [\sin(\phi) \mathbf{a}_x - \cos(\phi) \mathbf{a}_y]] \\ \mathbf{A} &= \frac{\mu_0 I}{4\pi R^2} (4w^2) [\sin(\theta) \mathbf{a}_\phi], \end{aligned} \quad (10)$$

\mathbf{a}_ϕ is the unit vector of a polar coordinate (R, θ, ϕ) .

Therefore, the magnetic flux density \mathbf{B} is:

$$\mathbf{B} = \nabla \times \mathbf{A} = \frac{1}{R \sin(\theta)} \frac{\partial}{\partial \theta} [A_\phi \sin(\theta)] \mathbf{a}_R - \frac{1}{R} \frac{\partial}{\partial R} [R A_\phi] \mathbf{a}_\theta$$

$$\mathbf{B} = \frac{\mu_0 m}{4\pi R^3} [2 \cos(\theta) \mathbf{a}_R + \sin(\theta) \mathbf{a}_\theta], \quad (11)$$

where m is the magnetic dipole moment and \mathbf{B} is the magnetic flux density at the point P due to the current loop $abcd$. Also, \mathbf{a}_θ , \mathbf{a}_ϕ and \mathbf{a}_R are the unit vectors in the spherical coordinates.

Therefore, the magnetic flux density generated by a square current loop is the same as that from a circular current loop (with the same magnetic dipole moment m) when the coil size is much less than the distance between the loop and the measurement point.

If S_1 is the cross sectional area of the transmitter loop, and ω is the resonant frequency of both transmitter and receiver circuitry, then

$$m = I_0 \sin \alpha \cdot S_1 \quad (12)$$

The magnetic flux (Φ) linkage from a square loop transmitter to a small square loop receiver with center at P is:

$$\Phi = \int_{S_2} \mathbf{B} \cdot d\mathbf{S}_2, \quad (13)$$

where S_2 is the cross sectional area of the receiver.

With N_1 number of turns in the transmitter and N_2 number of turns in the receiver, the voltage generated on the receiver is:

$$V = N_1 N_2 \left(-\frac{d\Phi}{dt} \right) \quad (14)$$

To reduce the measurement error of the magnetic field ($<1.0\%$), the ratio between R and the size of the receiver must be greater than 7.5 [105]. To simplify the calculation,

only coaxial orientation and coplanar orientation between the transmitter and receiver was investigated (Figure 4-4).

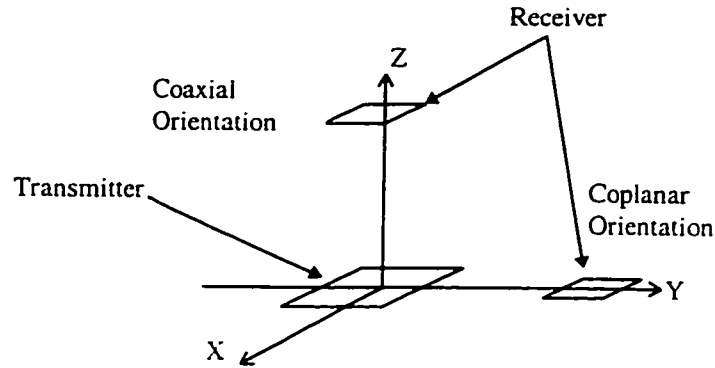


Figure 4-4. The coaxial orientation and the coplanar orientation of the receiver relative to the transmitter.

For coaxial orientation, $\theta = 0^\circ$,

$$\mathbf{B} = \frac{\mu_0 m}{2\pi R^3} \mathbf{a}_R \quad (15)$$

$$|V_{ca}| = \frac{\mu_0}{2\pi R^3} Q_i G N_1 N_2 S_1 S_2 I_0 \omega \quad (16)$$

For coplanar orientation, $\theta = 90^\circ$,

$$\mathbf{B} = \frac{\mu_0 m}{4\pi R^3} \mathbf{a}_\theta \quad (17)$$

$$|V_{cp}| = \frac{\mu_0}{4\pi R^3} Q_i G N_1 N_2 S_1 S_2 I_0 \omega \quad (18)$$

where G is the gain factor due to the ferrite core inside the transmitter and the receiver, and Q_i is the quality factor of coil- i of the receiver.

To calculate the self-inductance of a single square loop $abcd$, magnetic flux density \mathbf{B}_o at the center O of the square loop $abcd$ (refer to Figure 4-3) is first calculated. By applying the Biot-Savart law on the wire ad :

$$\mathbf{B}_o = \int d\mathbf{B} = \mathbf{a}_z \frac{\mu_0 I}{4\pi} \int_0^{2\pi} \frac{w dx}{(x^2 + w^2)^{3/2}}, \quad (19)$$

where \mathbf{a}_z is the unit vector in z-direction.

$$\mathbf{B}_o = \mathbf{a}_z \frac{\mu_0 I}{2\sqrt{2}\pi w}$$

Therefore, the total magnetic flux density due to the current loop *abcd* is:

$$\mathbf{B}_o = \mathbf{a}_z \frac{\mu_0 I}{2\sqrt{2}\pi w} \times 4 = \mathbf{a}_z \frac{\sqrt{2}\mu_0 I}{\pi w} \quad (20)$$

Therefore, the magnetic flux Φ due to N-turns of square loop is:

$$\Phi = \int_S N \mathbf{B}_o \cdot d\mathbf{s}, \quad (21)$$

where S is the cross sectional area of the square loop.

The direction of the B field is the same as the direction of the normal to the square loop, and the area of the square loop is $4w^2$. The B field at the center of the coil is greater than the B field at the ends of the coil. An average correction factor of 0.9 is used in the equation (21), because the B field at the end is 0.8 of the B field at the center [106].

Therefore, the total magnetic flux Φ due to N turns of coil is:

$$\Phi = \frac{4\sqrt{2}N\mu_0 I w * 0.9}{\pi} \quad (22)$$

The flux linkage Λ equals $N\Phi$, and the self-inductance L equals to the flux linkage Λ per unit current. Therefore, L is:

$$L = \frac{4\sqrt{2}N^2\mu_0 w * 0.9}{\pi} \quad (23)$$

Also, w can be calculated from the following equation:

$$w = \frac{r}{2(4\pi N)} \quad (24)$$

where r is the resistance of the coil and ρ is the resistivity of the wire.

4.4.2. Numerical Analysis and Results

Given $G=1.62$ (gain factor of the transmitter) \times 1.63 (gain factor of the receiver) = 2.64 , $N_1=800$ (no. of turns of transmitter), $N_2=500$ (no. of turns of receiver) and $\omega=24000\pi \text{ rads}^{-1}$ (the frequency for the transmitter and receiver)

The voltage generated by the coil-X of the transmitter in coil-X of the receiver can be calculated from equations (16) and (18). For $I_{x0} = 23.6 \text{ mA RMS(measured)}$, $S_{1x} = 278.89 \text{ mm}^2$, $S_{2x} = 116.64 \text{ mm}^2$ and $Q_x = 7.18$:

$$|V_{ca_{x-x}}(rms)| = \frac{8.8 \times 10^{-5}}{R^3} \quad (25)$$

$$|V_{cp_{x-x}}(rms)| = \frac{4.4 \times 10^{-5}}{R^3} \quad (26)$$

Likewise to calculate the signal in coil-Y of the receiver caused by coil-Y of the transmitter for which $I_{y0} = 22.8 \text{ mA RMS(measured)}$, $S_{1y} = 324 \text{ mm}^2$, $S_{2y} = 132.25 \text{ mm}^2$ and $Q_y = 7.33$:

$$|V_{ca_{y-y}}(rms)| = \frac{11.40 \times 10^{-5}}{R^3} \quad (27)$$

$$|V_{cp_{y-y}}(rms)| = \frac{5.70 \times 10^{-5}}{R^3} \quad (28)$$

Similarly for the signal caused by the coil-Z of the transmitter in coil-Z of the receiver, $I_{z0} = 19.9 \text{ mA RMS(measured)}$, $S_{1z} = 349.69 \text{ mm}^2$, $S_{2z} = 141.61 \text{ mm}^2$ and $Q_z = 7.12$,

$$|V_{ca_{z-z}}(rms)| = \frac{10.88 \times 10^{-5}}{R^3} \quad (29)$$

$$|V_{cpz-z}(rms)| = \frac{5.44 \times 10^{-5}}{R^3} \quad (30)$$

Since the size of coil-X (10.8 mm) of the receiver is the minimum of the three coils, the minimum distance between the transmitter and receiver is required to be $7.5 \times 10.8 \text{ mm} = 81 \text{ mm}$ so that the measurement error of the magnetic field is less than 1% [105].

Figures 4-5, 4-6 and 4-7 show the experimental and theoretical results of coaxial and coplanar orientation on coil-X to -X, coil-Y to -Y, and coil-Z to -Z, respectively. The voltage $V_{cax-x}(\text{RMS})$ is smaller than $V_{cay-y}(\text{RMS})$ and $V_{caz-z}(\text{RMS})$ because the cross sectional area of coil-X is the smallest of the three. The value of $V_{cat-i}(\text{RMS})$ is about twice the value of $V_{cpi-i}(\text{RMS})$, where i can be x or y or z . Also, the errors between theoretical and the experimental values are less than 1%. The theoretical values are always larger than the experimental value suggesting a systematic error.

Figures 4-8 and 4-9 show the experimental results and theoretical results of the inductance on the transmitter and receiver with only 1 layer of coil, respectively. Figure 4-10 shows the percentage error on the calculated inductance versus the number of turns of the coil on both transmitter and receiver.

4.4.3. Discussion and Conclusions

The output voltage of the receiver was measured by a Wavetek DM27XT digital multimeter and the accuracy on the AC measurement was $\pm 1.5\%$. The range of the distances between the transmitter and receiver is smaller in the coplanar position than the coaxial position because the voltage from the coplanar position is only half the voltage from the coaxial position. The differences of the experimental and theoretical results for

V_{cax-x} , V_{cpx-x} , V_{cay-y} , V_{cpy-y} , V_{caz-z} , and V_{cpz-z} are less than 1 % (within the accuracy of the test equipment). The theory that was applied to derive the magnetic flux density and the voltage received on the receiver was based on the Biot-Savart law. However, in this case the Biot-Savart law can be applied only when both the transmitter and the receiver are considered as two points. The larger the ratio of the size of the loop to the measured distance, the better the assumption. From Figures 4-8 and 4-9, more turns of the coil or smaller wire size produce less relative error on the calculated inductance. The measured inductance of the coil is proportional to the square of the number of turns that agrees with equation (23). The maximum error is about 2% on the receiver when the number of turns is more than 400. However, for both the transmitter and the receiver with the number of turns less than 300, the error is more than 10%. The error increases as the inductance value decreases. Also, the discontinuities on both figures 4-8 and 4-9 are due to the different errors in the multimeter at different scale range. From Figure 4-10, the error is greater than 50% when the number of turns are less than or equal to 100. The large errors associated with few turns occur because the wire does not cover the whole cross sectional area and thus equations (22) to (24) are not valid.

This study showed that the theoretical analysis of the magnetic field and the self-inductance due to a multiturn square-loop transmitter-receiver system matched the experimental measurements.

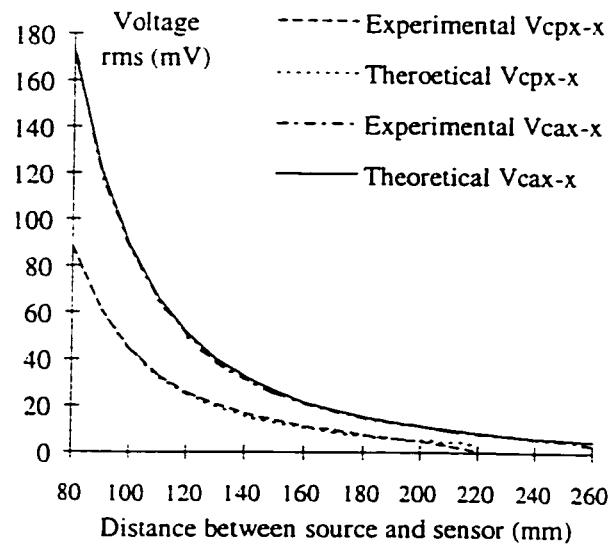


Figure 4-5. The experimental and theoretical results on the coaxial and coplanar arrangement of coil-X to X.

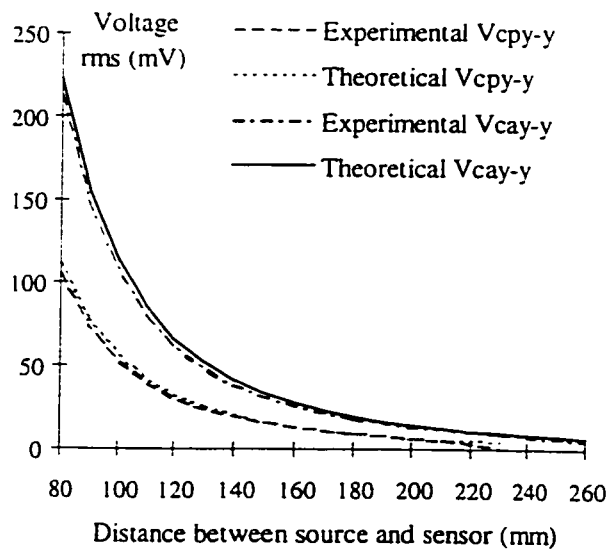


Figure 4-6. The experimental and theoretical results on the coaxial and coplanar arrangement of coil-Y to Y.

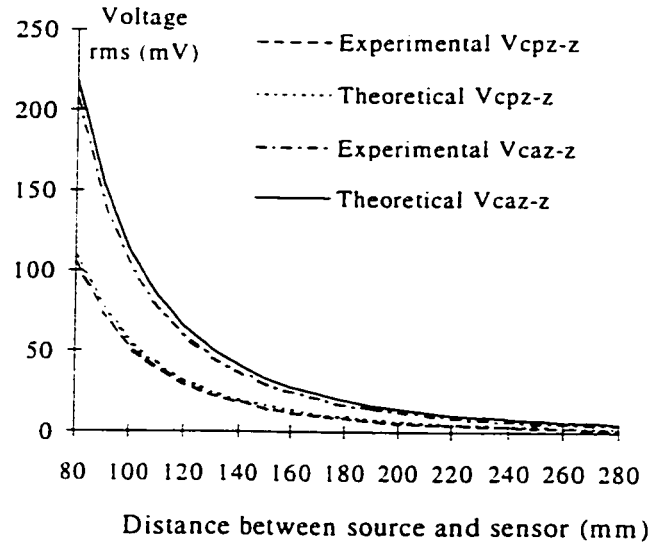


Figure 4-7. The experimental and theoretical results on the coaxial and coplanar arrangement of coil-Z to Z

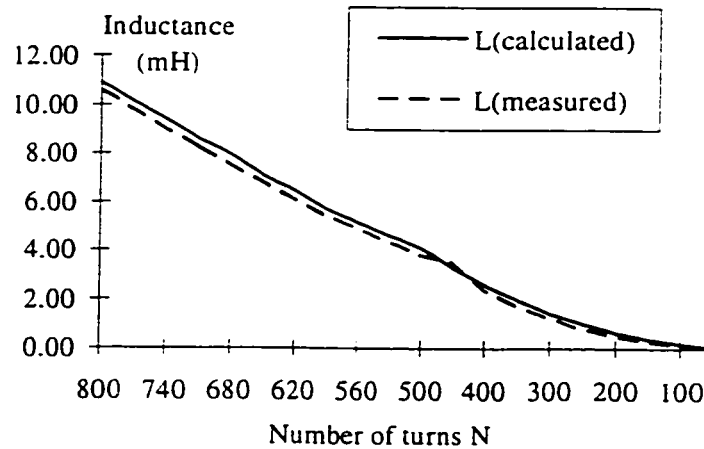


Figure 4-8. The experimental and theoretical results of the inductance on the transmitter with varying the number of turns of coil.

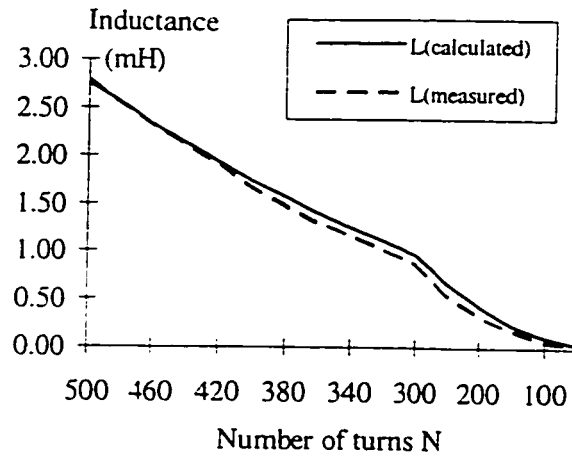


Figure 4-9. The experimental and theoretical results of the inductance on the receiver with varying the number of turns of coil.

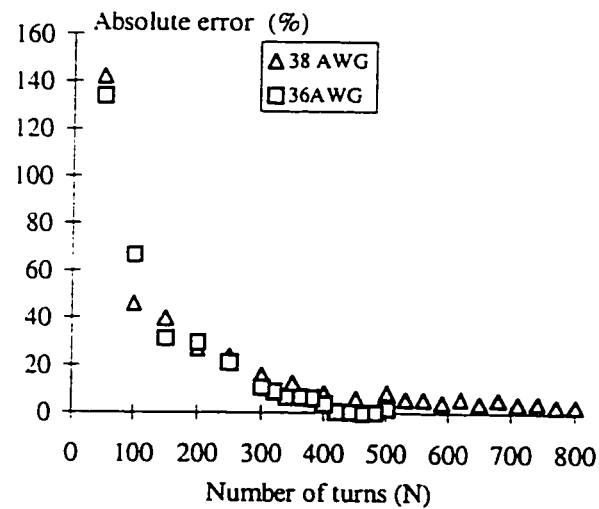


Figure 4-10. The absolute error on the calculating inductance versus the number of turns of the coil on two different thickness of wires.

4.5. Algorithm to Calculate Position and Orientation²

To determine the position and orientation of a receiver relative to the transmitter, the strength of the received signal was used. Referring to Figure 4-11 and from equation (11), the magnetic flux density \mathbf{B}_z generated from the square loop $abcd$ (with normal parallel to the z axis) to a point P is:

$$\mathbf{B}_z = \frac{\mu_0 m}{4\pi R^3} [2 \cos(\theta_z) \mathbf{a}_R + \sin(\theta_z) \mathbf{a}_{\theta_z}] \quad (31)$$

and the magnitude of the magnetic flux density $|\mathbf{B}_z|$ is:

$$|\mathbf{B}_z| = \frac{\mu_0 m}{4\pi R^3} \sqrt{[3 \cos^2(\theta_z) + 1]} \quad (32)$$

where m is the magnetic dipole moment from the loop $abcd$, μ_0 is the permeability of the free space.

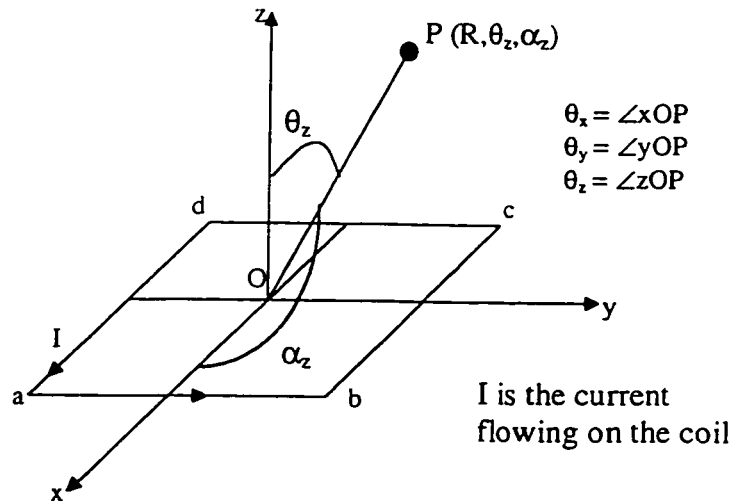


Figure 4-11. The position of the point p relative to the position of the square loop $abcd$.

² Material in this section has been submitted to IEEE Instrumentation and Measurements Journal on February, 1997, authors: E. Lou, N. G. Durdle, V. J. Raso, and D. L. Hill, title: A Low Power Posture Measurement System for the Treatment of Scoliosis.

Similarly, for a coil with a normal parallel to the x-axis or y-axis, the magnetic flux densities \mathbf{B}_x and \mathbf{B}_y and their magnitudes $|\mathbf{B}_x|$ and $|\mathbf{B}_y|$ will be equal to the followings:

$$\mathbf{B}_x = \frac{\mu_0 m}{4\pi R^3} [2 \cos(\theta_x) \mathbf{a}_R + \sin(\theta_x) \mathbf{a}_{\theta_x}] \quad (33)$$

$$|\mathbf{B}_x| = \frac{\mu_0 m}{4\pi R^3} \sqrt{[3 \cos^2(\theta_x) + 1]} \quad (34)$$

$$\mathbf{B}_y = \frac{\mu_0 m}{4\pi R^3} [2 \cos(\theta_y) \mathbf{a}_R + \sin(\theta_y) \mathbf{a}_{\theta_y}] \quad (35)$$

$$|\mathbf{B}_y| = \frac{\mu_0 m}{4\pi R^3} \sqrt{[3 \cos^2(\theta_y) + 1]} \quad (36)$$

Since

$$\cos^2(\theta_x) + \cos^2(\theta_y) + \cos^2(\theta_z) = 1, \quad (37)$$

the resultant magnitude $|\mathbf{B}_R|$ of the magnetic flux density due to the three transmitter coils is a constant at a fixed location.

$$|\mathbf{B}_R| = \sqrt{|\mathbf{B}_x|^2 + |\mathbf{B}_y|^2 + |\mathbf{B}_z|^2} = \text{constant}. \quad (38)$$

If S_1 is the cross sectional area of the transmitter loop $abcd$, the direction vector of \mathbf{S}_1 is the vector perpendicular to the cross section. The ω is the resonant frequency (12 kHz in this case) for both the transmitter and receiver. The magnetic dipole moment m can be calculated from equation (12). Then the magnetic flux linkages (Φ) can be calculated from equation (13). With N_1 number of turns in the transmitter and N_2 number of turns in the receiver, the voltage generated on the receiver is calculated from equation (14). If G is the total gain that includes the quality factor, the gain factors from ferrite cores and the circuit gain from an amplifier, then equation (14) can be rewritten as:

$$V = N_1 N_2 G \left(-\frac{d\Phi}{dt} \right) \quad (39)$$

Therefore, for a signal that transmits from a coil-z of the transmitter to a coil-z of the receiver, the voltage V_{zz} is:

$$V_{zz} = \left| \frac{\mu_0 G N_1 N_2 I_0 \omega S_1 S_2 [2 \cos(\theta_z) \mathbf{a}_R + \sin(\theta_z) \mathbf{a}_\theta] \cdot \mathbf{a}_z}{4\pi R^3} \right|$$

$$V_{zz} = \left| \frac{K [2 \cos(\theta_z) \mathbf{a}_R + \sin(\theta_z) \mathbf{a}_\theta] \cdot \mathbf{a}_z}{R^3} \right| \quad (40)$$

where K is a constant.

Since

$$\mathbf{a}_x = \mathbf{a}_R \sin(\theta_z) \cos(\alpha_z) + \mathbf{a}_\theta \cos(\theta_z) \cos(\alpha_z) - \mathbf{a}_\alpha \sin(\alpha_z) \quad (41)$$

$$\mathbf{a}_y = \mathbf{a}_R \sin(\theta_z) \sin(\alpha_z) + \mathbf{a}_\theta \cos(\theta_z) \sin(\alpha_z) - \mathbf{a}_\alpha \cos(\alpha_z) \quad (42)$$

$$\mathbf{a}_z = \mathbf{a}_R \cos(\theta_z) - \mathbf{a}_\theta \sin(\theta_z), \quad (43)$$

by substituting (43) into (40), gives

$$V_{zz} = \left| \frac{K [2 \cos^2(\theta_z) - \sin^2(\theta_z)]}{R^3} \right| = \left| \frac{K [3 \cos^2(\theta_z) - 1]}{R^3} \right| \quad (44)$$

Similarly

$$V_{zx} = \left| \frac{K [3 \cos(\theta_z) \sin(\theta_z) \cos(\alpha_z)]}{R^3} \right| \quad (45)$$

$$V_{zy} = \left| \frac{K [3 \cos(\theta_z) \sin(\theta_z) \sin(\alpha_z)]}{R^3} \right| \quad (46)$$

Therefore, the resultant voltage due to the coil-z of the transmitter is:

$$V_{zR} = \sqrt{V_{zx}^2 + V_{zy}^2 + V_{zz}^2} = \frac{K \sqrt{[3 \cos^2(\theta_z) + 1]}}{R^3} \quad (47)$$

Likewise, the V_{xR} and V_{yR} are equal to :

$$V_{xR} = \sqrt{V_{xx}^2 + V_{xy}^2 + V_{xz}^2} = \frac{K \sqrt{[3 \cos^2(\theta_x) + 1]}}{R^3} \quad (48)$$

$$V_{yR} = \sqrt{V_{yx}^2 + V_{yy}^2 + V_{yz}^2} = \frac{K\sqrt{[3\cos^2(\theta_y) + 1]}}{R^3} \quad (49)$$

Distance R can be determined by using the total sum of the square of the voltage. To calculate the location of point P, the following relations between θ_x and θ_y to the angles θ_z and α_z are used.

$$\cos(\theta_x) = \sin(\theta_z)\cos(\alpha_z) \quad (50)$$

$$\cos(\theta_y) = \sin(\theta_z)\sin(\alpha_z) \quad (51)$$

Summing the square of equation (50) and (51), gives

$$\cos^2(\theta_x) + \cos^2(\theta_y) = \sin^2(\theta_z) \quad (52)$$

From equation (52), the sum of the squares for the voltage V_{xR} and V_{yR} is a function of $\sin^2(\theta_z)$. A look-up table that relates the function of the ratio V_{xR} , V_{yR} and V_{zR} at different locations can be generated. Table 4-3 shows a part of the look-up table. Note that for $\mathbf{a}^2 + \mathbf{b}^2 = 5.0$; θ_z is 90° although α_z may vary from 0° to 90° . The specific value for θ_z can be determined by interpolation, e.g. $\mathbf{a}^2 + \mathbf{b}^2 = 4.90$, $\theta_z = 86.2^\circ$. The particular α_z can be determined from further interpolation (Table 4-4). For example, with $\mathbf{a}^2 + \mathbf{b}^2 = 4.90$ and $c = 1.973$; $\alpha_z = 4.00^\circ$.

Hence, the location of P (R, θ_z, α_z) is identified. Since, the look up table uses 5° increments, the maximum error on the angle calculations due to the linear interpolation method is 2.5° .

Table 4-3. The ratio between V_{xR} , V_{yR} and V_{zR} at different α_z with θ_z equal to 90° .

α_z (deg.)	θ_z (deg.)	$a=V_{xR}/V_{zR}$	$b=V_{yR}/V_{zR}$	$c=V_{xR}/V_{yR}$	a^2+b^2
0.0	90.0	2.00	1.00	2.00	5.00
5.0	90.0	1.99	1.01	1.97	5.00
10.0	90.0	1.98	1.04	1.89	5.00
15.0	90.0	1.95	1.10	1.78	5.00
20.0	90.0	1.91	1.16	1.64	5.00
25.0	90.0	1.86	1.24	1.50	5.00
30.0	90.0	1.80	1.32	1.36	5.00
35.0	90.0	1.74	1.41	1.23	5.00
40.0	90.0	1.66	1.50	1.11	5.00
45.0	90.0	1.58	1.58	1.00	5.00
50.0	90.0	1.50	1.66	0.90	5.00
55.0	90.0	1.41	1.74	0.81	5.00
60.0	90.0	1.32	1.80	0.74	5.00
65.0	90.0	1.24	1.86	0.66	5.00
70.0	90.0	1.16	1.91	0.61	5.00
75.0	90.0	1.10	1.95	0.56	5.00
80.0	90.0	1.04	1.98	0.53	5.00
85.0	90.0	1.01	1.99	0.51	5.00
90.0	90.0	1.00	2.00	0.50	5.00

Table 4-4. The values of a^2+b^2 and c at different θ_z and α_z .

α_z (deg.)	θ_z (deg.)	$c=V_{xR}/V_{yR}$	a^2+b^2
0.0	90.0	2.000	5.00
5.0	90.0	1.972	5.00
0.0	85.0	1.994	4.87
5.0	85.0	1.966	4.87

4.6. Summary

Both the transmitter and receivers are cubed-shaped. The gain factor due to the selected ferrite core was investigated. The increased permeability of the coil with the ferrite core was about 1.62 times of the free space. Also, from the self-inductance experiments, it was shown that the larger the ratio of the size of the loop to the measured distance, the more accurate on regarding the transmitter and receiver as two points. The magnetic flux density from a square loop was the same as that from a circular loop when the size of loop was much smaller than the distance between the loop to the desired point. Finally, an algorithm was developed to determine the positions and orientations of receivers relative to the transmitter so that the designed system can calculate the parameters automatically.

5. ERROR ANALYSIS

Errors are a concern in any measurement system. To preclude a false sense of accuracy, one must investigate the nature of the error, the sources, types, and magnitude of errors made at various stages of the measurement operation, and the interrelationship of errors. There are two types of errors, systematic and random. A systematic error is one which will invariably have the same magnitude and the same sign under the same given conditions. Such error can be estimated after a certain time of measurements. However, a random error is unpredictable. In this chapter, systematic errors related to different factors are examined.

5.1. Systematic Errors

In any measurement system, two types of error may exist, either systematic or random errors. Systematic errors are attributable to known conditions and vary with these conditions. Such errors can be evaluated and applied, with sign reversed, as corrections to measured quantities. Three types of systematic errors are natural errors, instrumental errors and personal errors. Natural errors arise from natural phenomena and they are really the effects of certain influences that operate to prevent the observer seeing or reading directly the quantity he is seeking. For example, an instrument that measures distance between two points by using the traveling time of a radio wave may give an erroneous distance if an adjustment is not made for the effect of atmospheric pressure and the moisture content in the air. Instrumental errors are the effects of imperfections in the construction or adjustment of the instruments used in making measurements. Personal errors depend on the physical limitations and on the habits of the observer. For example,

the observer may have poor ability in noting time at the beginning and end of an interval when using a stop-watch.

In this thesis, the instrumental errors that introduce systematic errors to the measurement device are evaluated. The instrumental errors exist because of the imperfect components and measurement instrument. In chapter 4, the ratio $V_{xx} : V_{yy} : V_{zz} : V_{yx} : \dots : V_{zz}$ was assumed equal to 1. The perfect ratio 1 occurs only when the system is ideal. Also, the ratio of $V_{xR} : V_{yR} : V_{zR}$ is 1 : 1 : 1 when the first assumption is valid. The system is an ideal system under the following conditions:

- 1) the effective surface areas in the transmitter of coil-X, -Y and -Z are the same.
- 2) the effective surface areas in the receiver of coil-X, -Y and -Z are the same,
- 3) the resonance frequencies in the transmitter of coil-X, -Y, and -Z are the same.
- 4) the resonance frequencies in the receiver of coil-X, -Y, and -Z are the same
- 5) the current flowing through coil-X, -Y, and -Z on the transmitter is the same, and
- 6) the quality factors of coil-X, -Y and -Z are the same.

These six factors affect the K value of the equation (40) in chapter 4. Any one of the above could alter the K value and change the final results. The variations due to these six factors can be divided into four groups. The first one is the effective surface area factor, the second one is the resonant frequency factor, the third one is the current flowing factor and the last one is the quality factor. Instead of calculating errors from each of the coils in those four groups, only errors from coil-Y will be calculated and used to demonstrate the calculation process. An analysis of individual factors is presented on each subsequent section.

5.2. Systematic Error Related to Effective Surface Area

In a perfect situation, the effective surface areas of coil-X, -Y and -Z must be the same. However, if the coil-X, -Y and -Z have different coil sizes, the K values for coil-X, coil-Y and coil-Z are different. Hence, it affects the ratio $V_{xx} : V_{xy} : V_{xz} : V_{yx} : \dots : V_{zz}$ as well as the ratio $V_{xR} : V_{yR} : V_{zR}$.

To determine the error due to the effective surface area, the ratio between the actual effective area and an assumed surface area was calculated. The configuration and size of the transmitter is the same as the receiver that described in chapter 4. Consequently, both of the transmitter and receivers have 500 turns of coils wound around on each direction. To determine the range of the surface area of coil-Y, the range of coil size for multiturn coil Y was measured to be 11.2 to 11.8mm. If the average coil size was used to represent the dimension of multiturn coil Y, the average effective area was $132.25\text{mm}^2 (=11.5 \times 11.5)$. Figure 5-1 shows the ratio of the actual area to the average effective area versus the dimension of a coil. For example at the point (11.2, 11.2, 0.95), each size of a coil is 11.2mm and the ratio of the actual area to the average effective area is 0.95. Therefore, the minimum and the maximum error factors are 0.95 and 1.05, respectively.

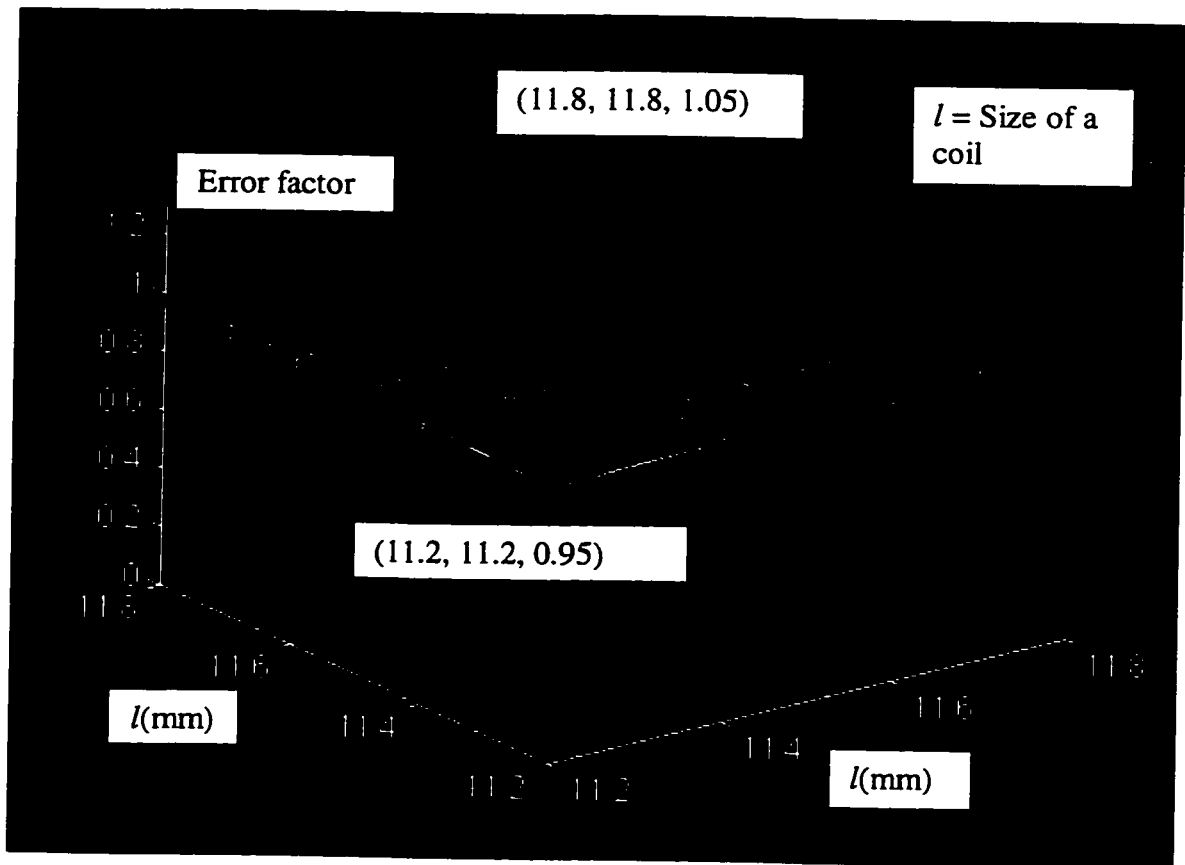


Figure 5-1. The ratio of the actual area to the theoretical area at different dimensions of the coil.

5.3. Systematic Error Related to Resonant Frequency

In any LC circuit, resonance frequency of a LC circuit is usually calculated from the actual values of the capacitance and the inductance. A multimeter can measure these two values. Specifications and accuracy of multimeters are provided by the manufactures. The multimeter that was chosen for measuring the designed circuit had 5% error in inductance and capacitance, and 1% error in resistance. Therefore, the actual values of L and C may vary from 95% to 105% of the measured values. Since the error of the resistance was only 1%, the error due to resistance was ignored when comparing to

inductance and capacitance. Table 5-1 shows the properties and characteristics of a coil with resonance circuit.

Table 5-1. The properties and characteristics of a coil with resonance circuit.

	Resistance R (Ω)	Inductance L (mH)	Capacitance (nF)	Quality Factor ($\omega L/R$)
Coil-X	48.28	4.79	36.7	7.48
Coil-Y	51.24	4.83	36.4	7.11
Coil-Z	55.63	5.03	35.0	6.82

For coil-Y the range of inductance was $4.83 \pm 0.2415 \text{mH}$ and capacitance was $36.4 \pm 1.85 \text{nF}$. On a series LC circuit, the theoretical resonant frequency ω_0 was calculated by the following equation:

$$\omega_0 = \frac{1}{\sqrt{L_0 C_0}}, \quad (1)$$

where $L_0 = 4.83 \text{mH}$ and $C_0 = 36.4 \text{nF}$.

However, the actual frequency ω was calculated from the actual L and C values.

$$\omega = \frac{1}{\sqrt{(L_0 + \delta L)(C_0 + \delta C)}}, \quad (2)$$

where δL and δC were the errors of the inductance and capacitance from the multimeter.

Figure 5-2 shows the values of ω/ω_0 versus the actual values of L and C. The minimum and maximum values of ω/ω_0 are 0.952 and 1.053, respectively.

On a parallel LC circuit, the theoretical resonant frequency ω_0 was calculated by

$$\omega_0 = \sqrt{\frac{1}{LC} - \left(\frac{R}{L}\right)^2} \quad (3)$$

Since the value $(1/LC)$ is much greater than $(R/L)^2$, the resonant frequency ω_0 from a parallel LC circuit is approximately equal to that from a series LC circuit. Therefore, the error from the parallel LC circuit was assumed to be the same as that from a series LC circuit.

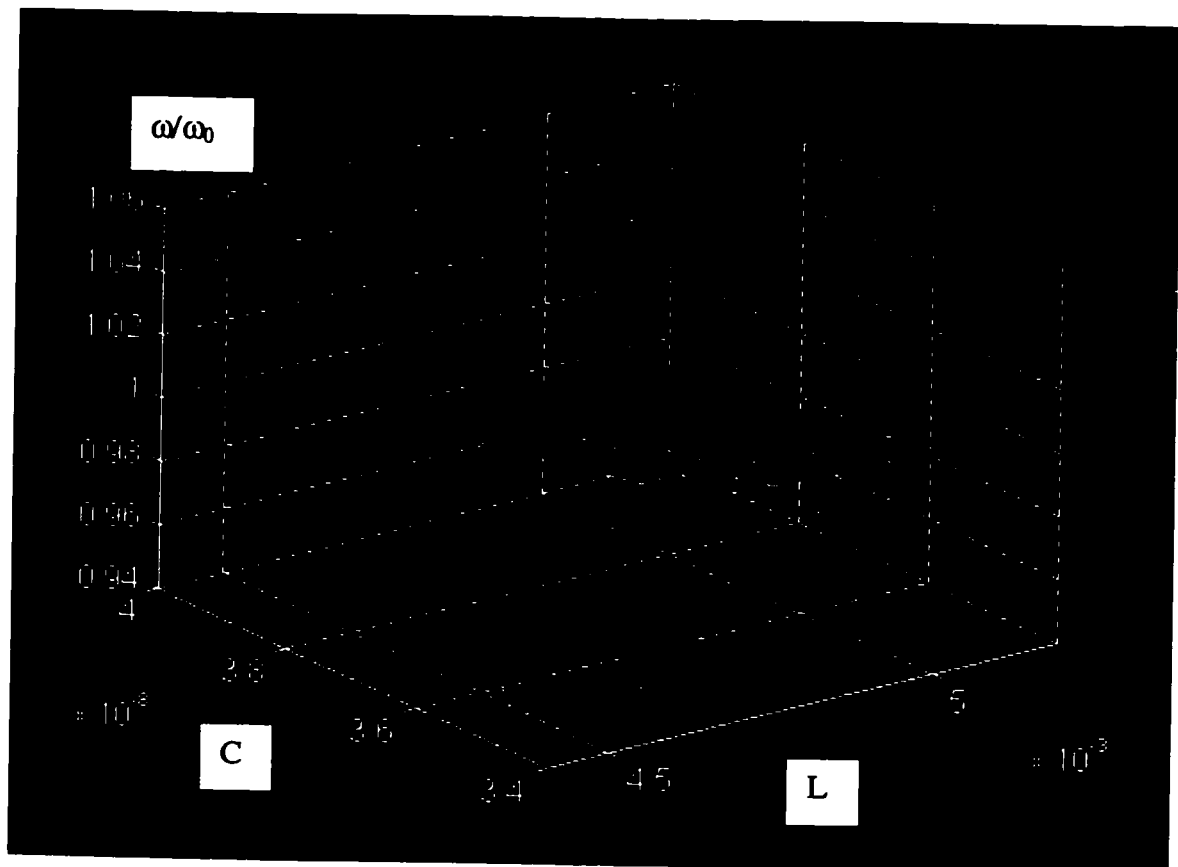


Figure 5-2. The ratio of the actual frequency to the theoretical frequency at different inductance and capacitance values.

5.4. Systematic Error Related to the Current in the Transmitter Coils

Current flowing through a series LC circuit depends on the admittance Y of the circuit. Y was calculated from the following equation:

$$Y = \frac{1}{R + j(\omega L - 1/\omega C)} \quad (4)$$

The magnitude of the admittance is:

$$|Y| = \frac{1}{\sqrt{R^2 + (\omega L - 1/\omega C)^2}} \quad (5)$$

The magnitude of the current I was then calculated from the following equation:

$$|I| = |V||Y|, \quad (6)$$

where $|V|$ is the magnitude of the voltage supply to the circuit and is a constant.

Therefore, as the frequency varies, the magnitude of Y varies and is maximum when $\omega L = 1/\omega C$. Since the inductance and capacitance for the coil-X, -Y and -Z were different, the current flowing in each coil was slightly different. If Y_m is designated the maximum magnitude of Y and $\pm 5\%$ of the variation of the inductance and capacitance is added, then Y/Y_m is:

$$\frac{Y}{Y_m} = \frac{1}{1 + jQ_0\left(\frac{\omega}{\omega_0} - \frac{\omega_0}{\omega}\right)}, \quad (7)$$

where $Q_0 = \frac{1}{R} \sqrt{\frac{L_0}{C_0}}$, ω and ω_0 were calculated from equations (1) and (2).

Figure 5-3 plots the values of $|Y|/|Y_m|$ versus the inductance and capacitance of coil Y.

From equation (6), the magnitude of I was proportional to the magnitude of Y ; therefore,

$|I|/|I_m|$ would be equal to $|Y|/|Y_m|$. The minimum and maximum values of $|Y|/|Y_m|$ are 0.8078 and 1.0, respectively.

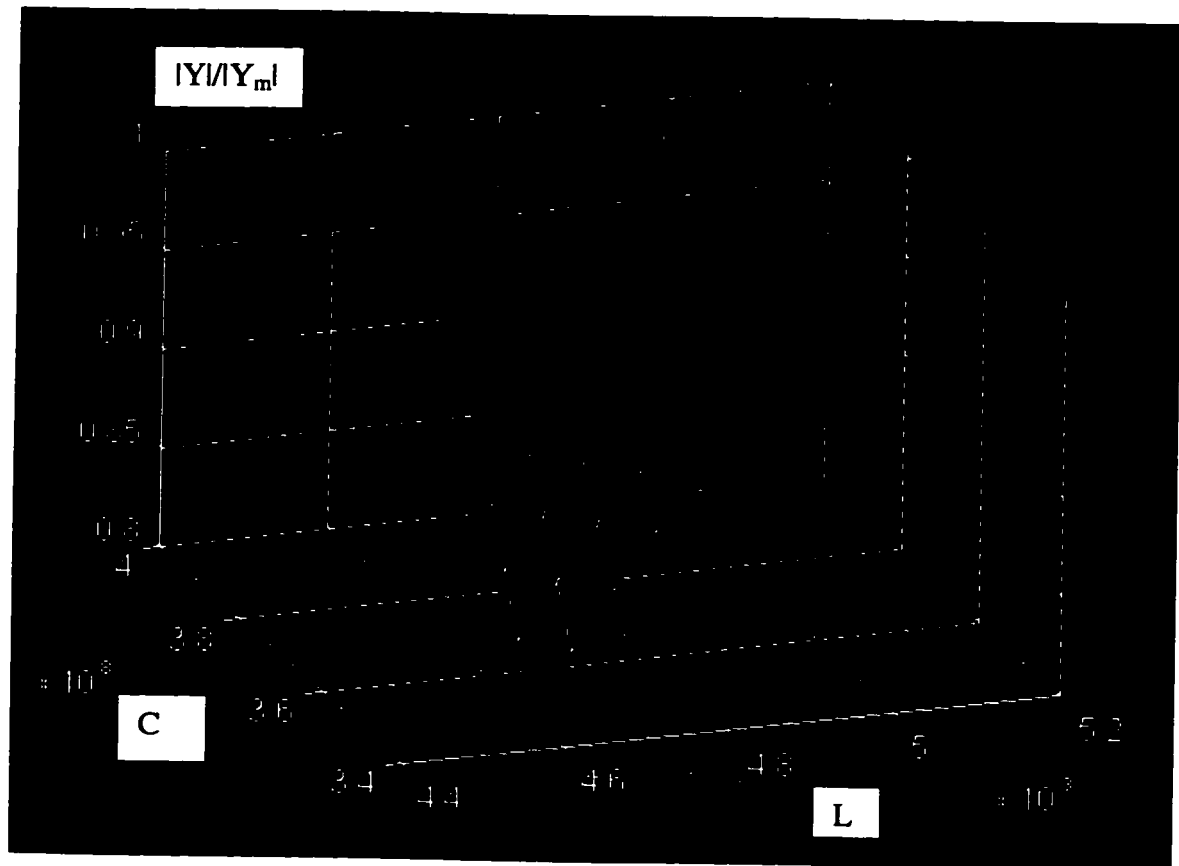


Figure 5-3. The ratio of the actual current I to the maximum of current I_m versus inductance and capacitance.

5.5. Systematic Error Related to Quality Factor

From the table 5-1, the quality factor of coil-X, -Y and -Z are 7.48, 7.11 and 6.82, respectively. For the coil-Y, the average quality factor was 7.11 and equal to $\omega L/R$, the error of the quality factor can be calculated from the product of the error from ω and L . Therefore, the minimum and maximum errors from the quality factors are 0.9996 and 1.004.

5.6. Minimum and Maximum Errors

From equation (40) in chapter 4. K is equal to

$$K = CS_1S_2\omega I_0Q, \quad (8)$$

where C is a constant. By combining the error scale factor due to each of the above factors, the total minimum and maximum scale factors due to the above three factors can be calculated to be:

minimum error scale factor = $0.95*0.95*0.952*0.8078*0.9996 = 0.693$, and

maximum error scale factor = $1.05*1.05*1.053*1.0*1.004 = 1.166$.

5.7. Discussion

In the pervious calculations. errors in coil-Y were calculated. The results only show the intra-error in one coil, but the inter-errors between coil-X and coil-Z relative to coil-Y exist. The inter-error occurs because in theoretical calculations properties and characteristics of coil-Y are assumed to be the average values for all three coils. Therefore, the maximum and minimum errors of the system based on theoretical calculations will be greater than the calculated values. Therefore, instead of using a theoretical approach, calibration of the system to obtain the actual ratios between the nine collected data will be done in chapter 7. These data will be implemented into the system to calculate the required parameters.

6. A NOVEL LOW POWER PORTABLE EM MEASUREMENT SYSTEM

To measure postural changes of topographical features, a low power portable EM measurement system was investigated. In this research, the term “low power system” means a system with a power supply less than 9V and the average current consumption per hour is less than 5 mA. The hardware of the EM system can be divided into three sections: a transmitter circuit, a receiver circuit and a microcomputer system. To establish the best approach for the development, studies of each section were done. In addition, power supply requirements is one of greatest concern for portable electronic devices. A literature review of different types of batteries was done to facilitate the choice of a power supply. Furthermore, the software was designed to make the system completely automatic. Three programs, the control program for the microcomputer system, the interface program for calibration, and the conversion program to convert a S-record file into machine code will be described.

6.1. Introduction

A biofeedback approach to help adolescents who have idiopathic scoliosis has been proposed. This approach is based on the proprioceptive concept of monitoring patients posture during their daily activities. A system to measure topographical features and to provide feedback to patients was envisioned. Since the system will be carried by patients during their daily activities, small size, light weight, low-power and robustness are necessary. The size and weight of the system was based on discussions with patients. Most patients expect the size and weight of the system to be similar to a “Walkmen”

(dimensions: 12cmx 9cm x3cm, weigh: 50g). The smaller and lighter the system, the more favor by patients.

A selection of a power supply usually depends on the power consumption of a system. Also, since the size and weight of a battery pack is usually proportional to its power capacity, the type of battery selected depends on the run-time of the battery. To establish a miniature low power system, the number and type of ICs that provided all the required functions were carefully selected. Also, power consumption can be reduced by turning off the power to any ICs that is not in use. Apart from the hardware design, a custom software design also provides challenges.

6.2. Transmitter Circuit

In the first prototype, the larger cube with three orthogonal coils described in chapter 4 was used to generate a relatively strong signal. To generate a transmitted signal, a Wein bridge oscillator with a 12 kHz sine wave signal was first built and connected to the transmitter through 3 cables (about 40cm long). Each cable had a pair of wires connected to either end of the multiturn coil. The 12 kHz signal was selected because that frequency had minimum interference [100] from the environment. To save energy, the oscillator was switched in turn so that only one coil was in resonance at a time. Each coil was connected as a series LC resonant circuit. Maximum current drawn from the source to coil-X, -Y or -Z was measured to be 23.6 mA RMS. The crosstalk signal from the active channel to the other two channels was -45dB (resonant voltage: 70V p-p, crosstalk signal: 400 mV). Crosstalk signals not only waste power but also corrupt the transmitted signals by adding erroneous results to the received signals. Also,

the long wires added extra inductances, capacitances and resistances to the three LC circuits in the transmitter, which made the resonant signals very unstable due to the unstable impedance on the wires. Touching or bending could change the impedance of the wires, which resulted in changing the resonant voltages. Therefore, a refinement of the transmitter circuit was necessary. In the new approach the problems due to the long lead wires were solved and the size of the transmitter and the crosstalk signals were reduced.

A new transmitter which was similar in size to the receiver was built. The new transmitter was expected to have either the same or higher transmitted signal level. Instead of using the sine wave signal, two twelve-kilohertz square waves were connected to each of the LC circuits. These two square waves were 180 degrees out of phase. An op-amp was used to generate a square wave signal, and an inverted square wave was then obtained by using an inverter circuit. The square wave signal was used because a stronger transmitted signal were obtained. Figure 6-1 shows the schematic diagram that used two op-amps to generate a non-inverted and an inverted square waves. Two power amplifiers with maximum output current of 100mA were used as buffers to drive the transmitter. Maximum current drawn from the source to coil-X, -Y or -Z was measured to be 170 RMS mA. Figure 6-2 shows the schematic diagram that connects the two square wave signals to the transmitter. Each coil was still switched in turn so that only one coil was in resonance at a time. Since a new transmitter coil was built, the properties and characteristics of the new transmitter coil are reported in table 6-1.

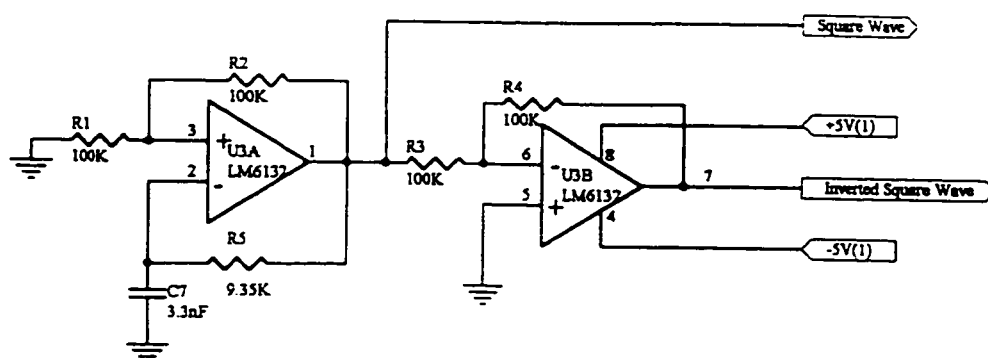


Figure 6-1. Schematic diagram of the inverted and non-inverted square wave signals generated.

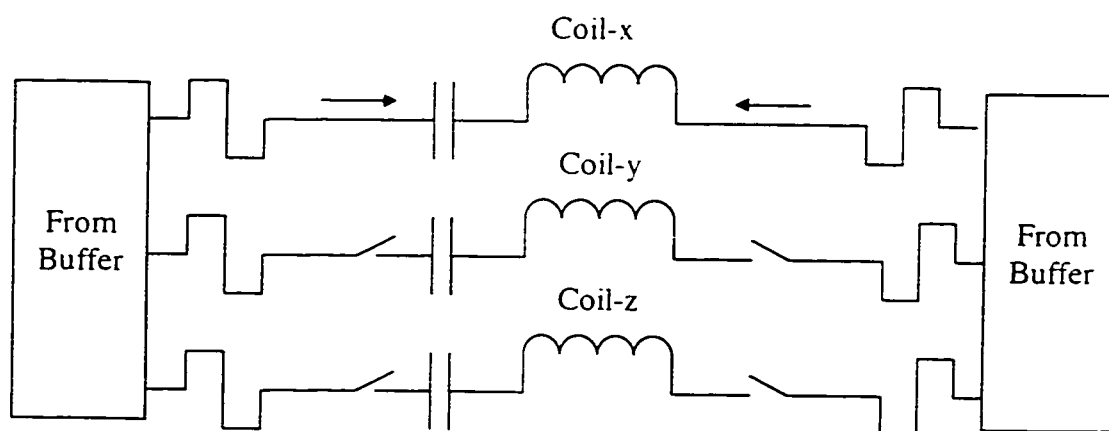


Figure 6-2. The schematic diagram of the series LC transmitter circuits.

Table 6-1. Properties and characteristics of the transmitter coil with resonance circuit.

	Resistance (Ω)	Inductance (mH)	Capacitance ¹ (nF)	Quality Factor ($\omega L/R$) ²
Coil-X	48.99	4.94	35.6	7.60
Coil-Y	50.98	4.85	36.3	7.17
Coil-Z	52.78	4.82	36.5	6.88

¹ The capacitor value that used to build the resonance circuit in the transmitter.

² $\omega (=2\pi f)$ is the resonance frequency in radian/sec.

To eliminate the voltage drop, noise pick up and the unstable impedances due to the long lead wires, circuits that generate the square and inverted square waves, and the switching circuits were placed adjacent to the transmitter coils. The crosstalk signal was measured again. Figure 6-3 shows the crosstalk and resonant voltages on two channels in the new transmitter. The crosstalk signal was reduced from -45dB (from the previous version) to -62dB . The final dimensions of the transmitter unit became $1.5\text{cm} \times 1.5\text{cm} \times 3.5\text{cm}$. Although the size of the transmitter unit was bigger than a three-axis coils unit ($1.5\text{cm} \times 1.5\text{cm} \times 1.5\text{cm}$), a more stable signal with less crosstalk was obtained. Figure 6-4 shows the new transmitter unit.

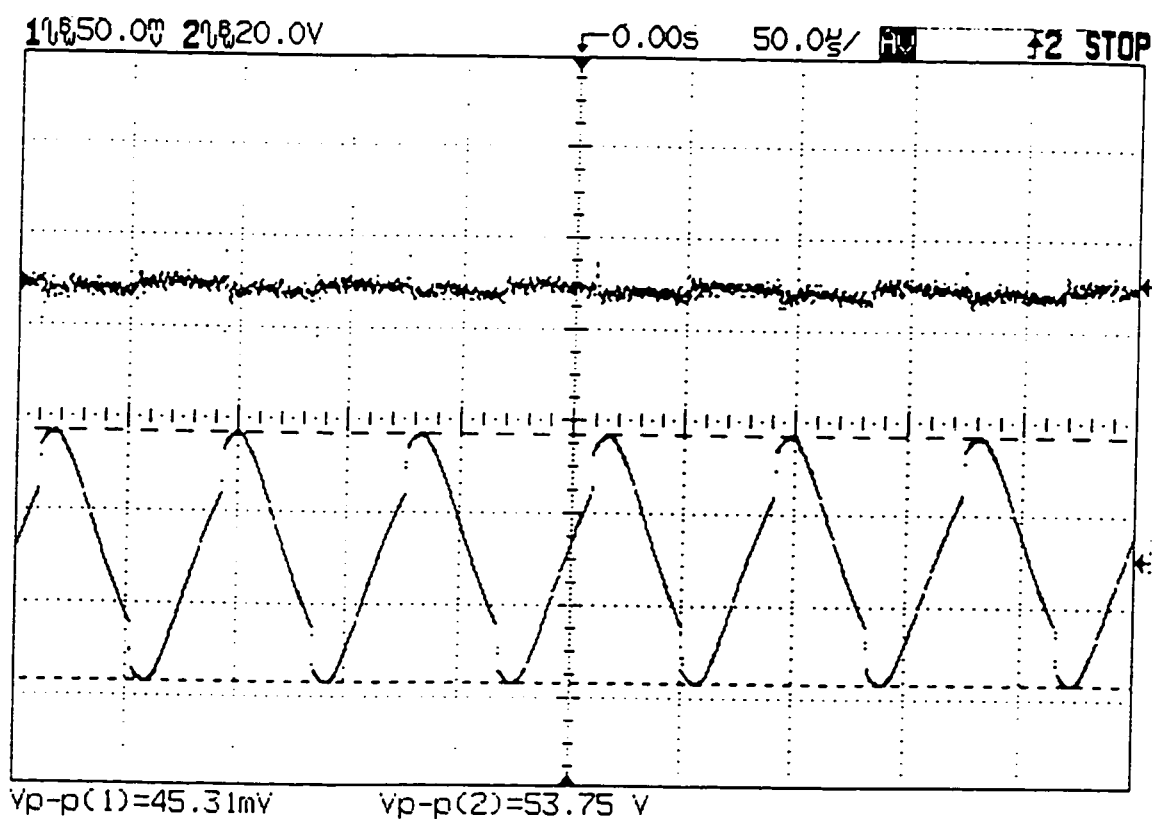


Figure 6-3. The crosstalk voltage (1) and the resonant voltage (2) on two channels in transmitter.

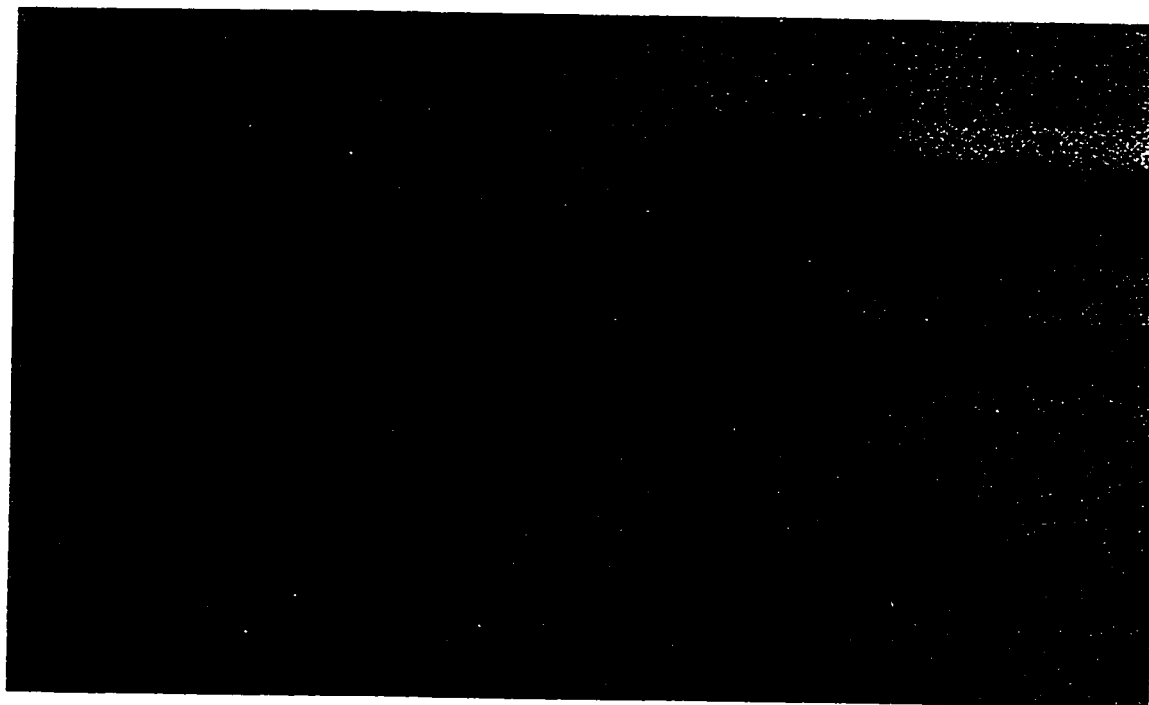


Figure 6-4. The actual view of the transmitter unit.

6.3. Receiver Circuit

In initial prototyping, one more receiver which was the same as that described in chapter 4 was built. Table 6-2 a) and b) shows the properties and characteristics of the receiver coils 1 and 2, respectively. Each three-axis coil unit was connected to the main circuit board through 3 long cables (about 50 cm). Each cable had a pair of wires connected to either end of one-axis multiturn coil. A parallel LC circuit was used to receive the signals. The long cables picked up environmental noises and changed the received signals due to the change of impedance in the wires. Problems due to the long cables were similar to that from the first transmitter. Also, the signal-to-noise ratio of the received signals was only 45dB when the received signal was 1V p-p. To improve the

performance of the receiver circuit and to eliminate the problems due to the long cables, a modified receiver circuit was built.

Table 6-2 a). The properties and characteristics of the receiver 1 with resonance circuit.

	Resistance R (Ω)	Inductance L (mH)	Capacitance ³ (nF)	Quality Factor ($\omega L/R$) ⁴
Coil-X	48.28	4.79	36.7	7.48
Coil-Y	51.24	4.83	36.4	7.11
Coil-Z	55.63	5.03	35.0	6.82

Table 6-2 b). The properties and characteristics of the receiver 2 with resonance circuit.

	Resistance R (Ω)	Inductance L (mH)	Capacitance ³ (nF)	Quality Factor ($\omega L/R$) ⁴
Coil-X	49.30	4.82	36.5	7.37
Coil-Y	52.21	4.87	36.1	7.03
Coil-Z	56.43	5.15	34.1	6.88

³ The capacitor value that used to build the resonance circuit in the transmitter.

⁴ ω is the resonance frequency in rad/sec ($=2\pi f$).

To eliminate the problems due to the long cables the amplifier and all the required circuits were placed close to the receiver coils. Figure 6-5 shows the schematic diagram of the new receiver circuit. The receiver circuit still used parallel LC circuit to receive signals. When coil-X was closed, coil-Y and coil-Z were opened. The multiplexer was used to select the required channel, and its output was connected to an amplifier so that a pre-gain signal was sent to the main circuit board. Also, to increase the signal-to-noise ratio on the received signal, either the size of the receiver must be increased or the noise picked up from environment must be reduced. However, since small size was one of the aims of the system, noise reduction was the favored way to increase the signal-to-noise

ratio. Noise reduction was achieved by amplifying the received signal before sending it to the computer unit. The resonance and the amplification circuits placed adjacent to receiver coils also achieved this purpose. Surface mount ICs were used for the required circuit to keep the size of the whole unit as small as possible. Also, this arrangement increased the portability of the receiver unit so that it might be used for other applications without requiring any other external circuit. The signal-to-noise ratio of the received signal was 65dB when the received signal was 1 V p-p. Therefore, the new receiver unit combined with circuit proved to be a better approach for the receiver. The final dimensions of the receiver units were 1.5cm x 1.5cm x 3.0cm (Figure 6-6).

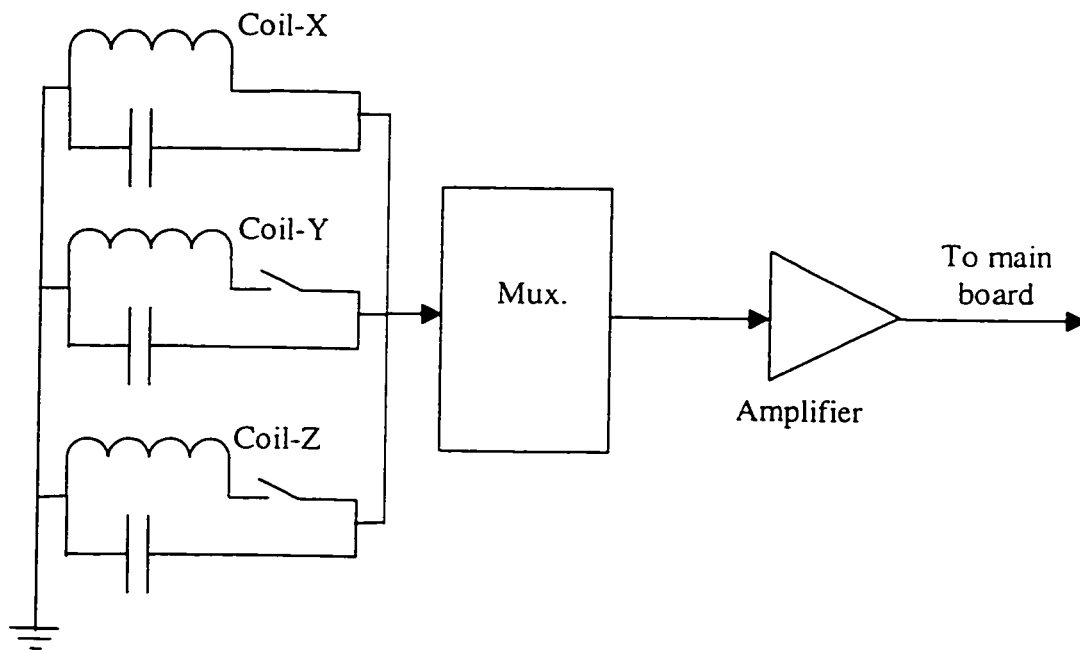


Figure 6-5. The schematic diagram of the receiver circuitry.

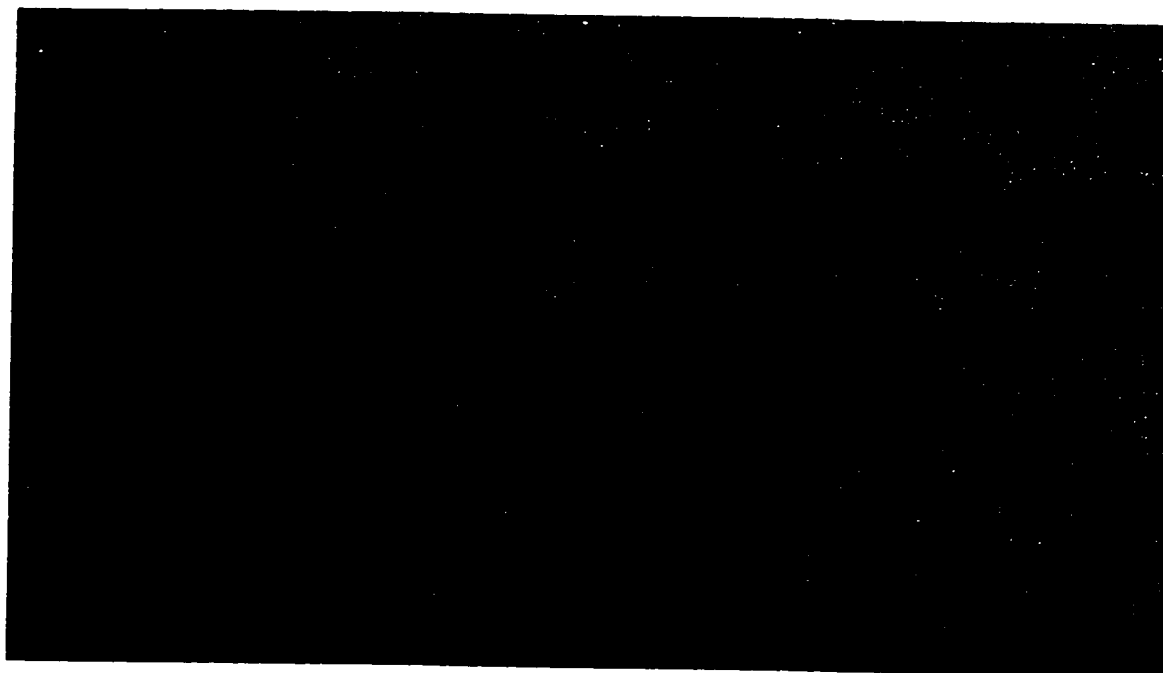
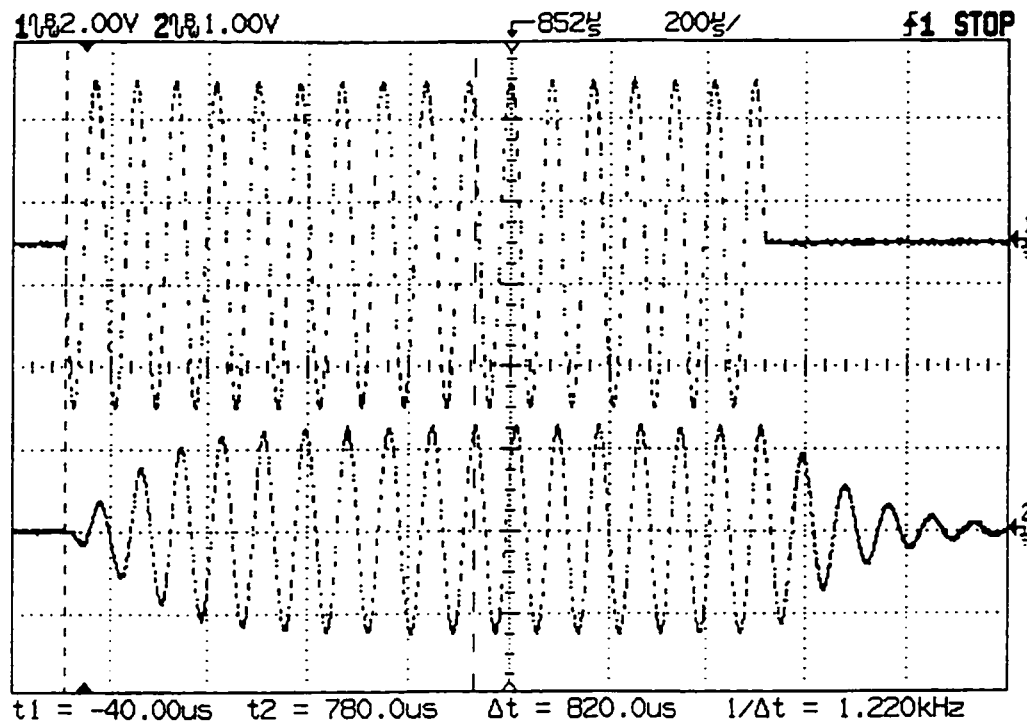


Figure 6-6. The actual view of the receiver unit.

To minimize power consumption of both the transmitter and the receiver circuits, the power for both units was turned on only when the data were acquired. An experiment was done to measure the time required by the receiver to obtain a maximum signal after the transmitted signal was turned on. A sine wave signal was first connected to one of the transmitter coils. The signal was set and turned on for 1.5ms. The signal received on the receiver was measured with an oscilloscope [HP-54600A] and is shown on Figure 6-7. Referring to Figure 6-7, signal 1 is the transmitted sine wave signal with a magnitude of $\pm 5V_{p-p}$, while signal 2 shows the time required by the receiver to obtain the full scale signal after the transmitted signal was turned on. The time required was measured at $820\mu s$. When the transmitted signal was turned off, another $820\mu s$ was required to allow the received signal to attenuate. Therefore, 2ms was adequate for one measurement. Since nine measurements were required for 1 receiver, a minimum 18ms was the time required to sample both units.



1-the transmitted signal, 2- the received signal

Figure 6-7. The time required for the receiver to receive a full scale signal after the transmitted signal was turned on.

6.4. Microcomputer System

As mentioned before, the power consumption of the system can be minimized by turning off any ICs or circuits that are not in use. Therefore, using a controller to control the power for both the transmitter and the receiver units was investigated. Also, a powerful controller is necessary to do the data manipulation. To select a controller, either a microprocessor or a microcontroller or a digital signal processor was considered. The choice of the controller mainly depended on its power consumption and physical size. Table 6-3 shows the characteristic of these three controllers. Among these three, a microcontroller was chosen because it consumed the least power and required the minimum number of external components. Among all the commercially available

microcontrollers, the Motorola product - MC68HC16Z1 microcontroller was chosen. This microcontroller was selected mainly because of its low power consumption, ease of programming and built-in analog-to-digital (A/D) converter. Even though a microcontroller already contains many special functions, some other components and circuits were still required to complete the microcomputer system.

The block diagram of the microcomputer system is shown in Figure 6-8. The microcontroller, MC68HC16, is the major component of this system. This system consists of three sections. The first section is the digital data acquisition section which consists of two 128 Kbytes RAMs, two 8 Kbytes ROMs and a programmable real time clock (RTC). The second section is the received signal section which consists of a multiplexer, a bandpass filter (BPF), a RMS-to-DC integrated circuit, a low pass filter and a phase detection circuit. The third section is the transmitted signal section which was described in one of the previous sections.

Table 6-3. Comparison of the microprocessor, microcontroller and DSP.

	Microprocessor	Microcontroller	DSP
Power consumption	High	Low	High
Required external A/D converter	Yes	No	Yes
Required external UART¹	Yes	No	No
Physical size	Large	Small	Large
Price/unit	High	Low	High

¹. UART-Universal Asynchronous Receiver Transmitter

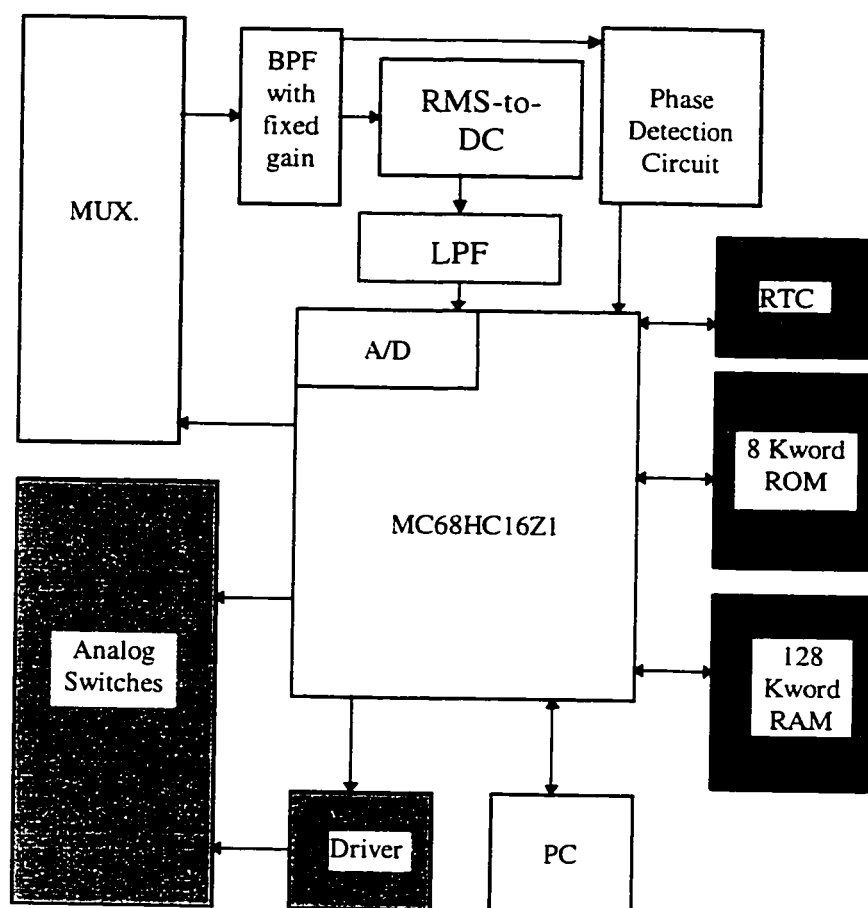


Figure 6-8. The block diagram of the microcomputer system.

6.4.1. The MC68HC16 Microcontroller

The MC68HC16Z1 microcontroller is a high speed 16-bit control unit as well as a member of the M68300/68HC16 Family of modular microcontrollers. In a normal operation, the maximum supply current to this controller is 110mA, but during a low-power stop (LPSTOP) mode, the maximum supply current is only 350 μ A. Power consumption is minimized when the microcontroller is programmed into the LPSTOP mode. An external interrupt is required to awaken the microcontroller from the LPSTOP mode. The maximum speed of the system clock is 16.78 MHz. In addition, this microcontroller consists of a 16-bit CPU (CPU16), a system integration module (SIM),

an 8/10-bit analog-to-digital (A/D) converter, a queued serial module (QSM), a general-purpose timer (GPT), and a 1024-byte standby SRAM. Figure 6-9 shows the internal block diagram of the microcontroller. All these modules are interconnected by the intermodule bus (IMB) and their functions will be explained in the appendix A.

6.4.2. Digital Data Acquisition Section

There are three components connected to the microcontroller: 1) two 8-Kbytes ROMs, 2) two 128-Kbytes RAM and the programmable real time clock (RTC).

6.4.2.a. Read Only Memory (ROM)

The type of ROM (27C64) in this system is an 8-Kbytes, ultraviolet erasable programmable read-only memory. This type of ROM was chosen because of its low power consumption and sufficient memory space available. The data in the ROM can be erased by exposure to an ultraviolet light source with a minimum dosage 15 Wseconds/cm². Two ROMs are used in this system so that 8-Kwords of program or data can be stored. The memory address of the ROMs is mapped from \$000000 to \$001FFF. The ROMs hold both the control program and look-up tables. The control program, written in MC6816 assembly language, oversees the operation of the system under interrupt control while the look-up tables store the information that is used to calculate the position and orientation of the receiver relative to the transmitter. The block diagram of the connection between the ROMs and the MCU is shown in Figure 6-10.

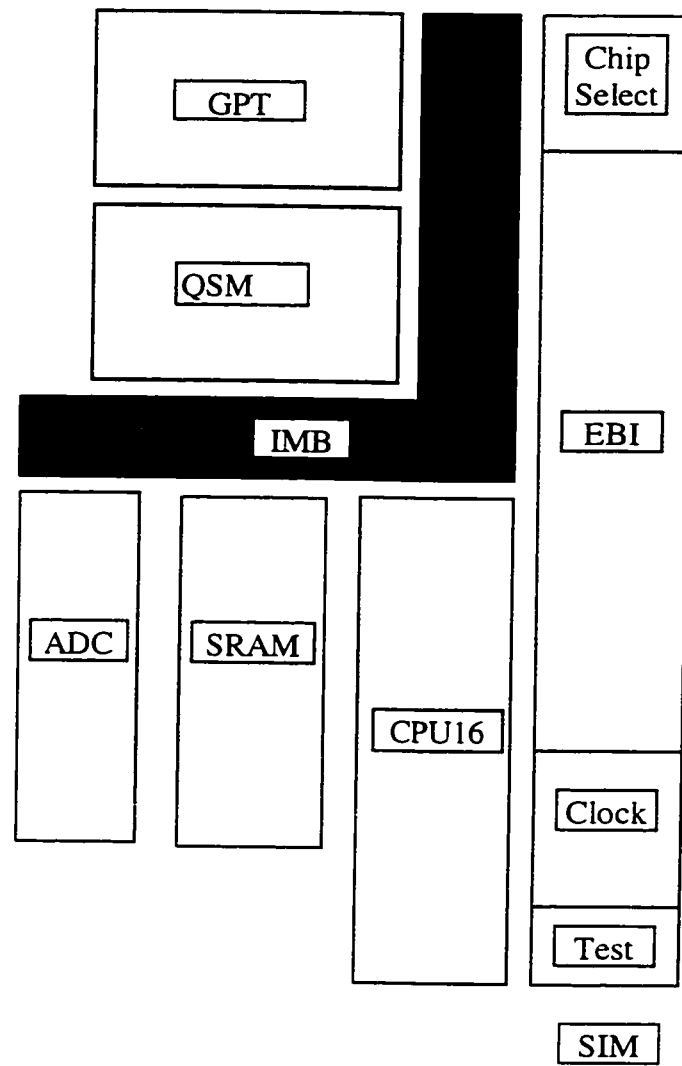


Figure 6-9. The block diagram of the internal module of the MC68HC16Z1 microcontroller.

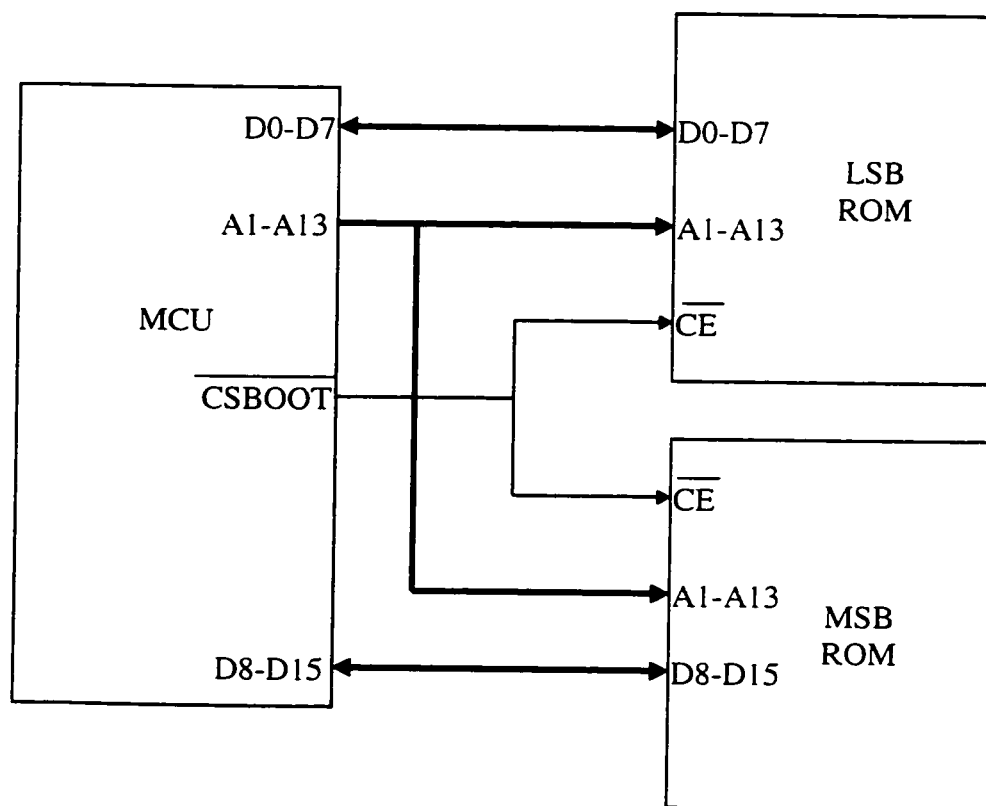


Figure 6-10. The block diagram of the connection between ROMs and MCU.

6.4.2.b. Read Access Memory (RAM)

A high speed low-power 128-Kbyte static RAM (KM681000LP) is used in this system. This IC is fabricated using CMOS process and is particularly well suited for battery back-up non-volatile memory applications. To expand the memory size for the system, two RAMs were used. The total memory size of the system became 128 Kwords and the address of the RAMs was mapped from \$040000 to \$07FFFF. The RAM stores all the acquired data that will be downloaded to a host computer. The block diagram of the connection between the RAMs and the MCU is shown in Figure 6-11.

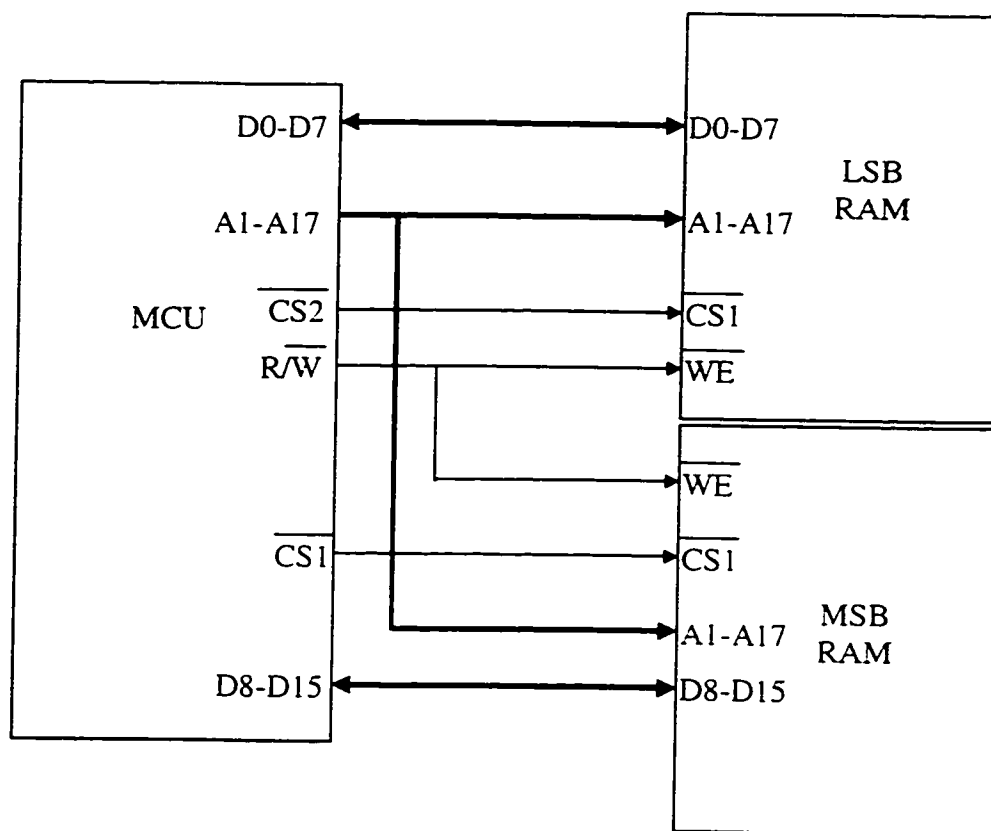


Figure 6-11. The block diagram of the connection between RAMs and MCU.

6.4.2.c. Programmable Real Time Clock (RTC)

The programmable RTC with a built in static RAM (MC68HC68T1) is a Motorola product. This device was chosen because of the ease of interfacing with the MCU and its low power consumption. The RTC and the MCU communicates through the serial communication port of the MCU. Four special features contained in this device are: 1) a real time clock/calendar, 2) a programmable interrupt for alarm and timing function, 3) a square wave generation circuit, and 4) a 32-Kbytes static RAM. However, the main function of this IC is to provide an interrupt signal to awaken the MCU from the

LPSTOP mode. The block diagram of the connection between the RTC and MCU is shown in Figure 6-12.

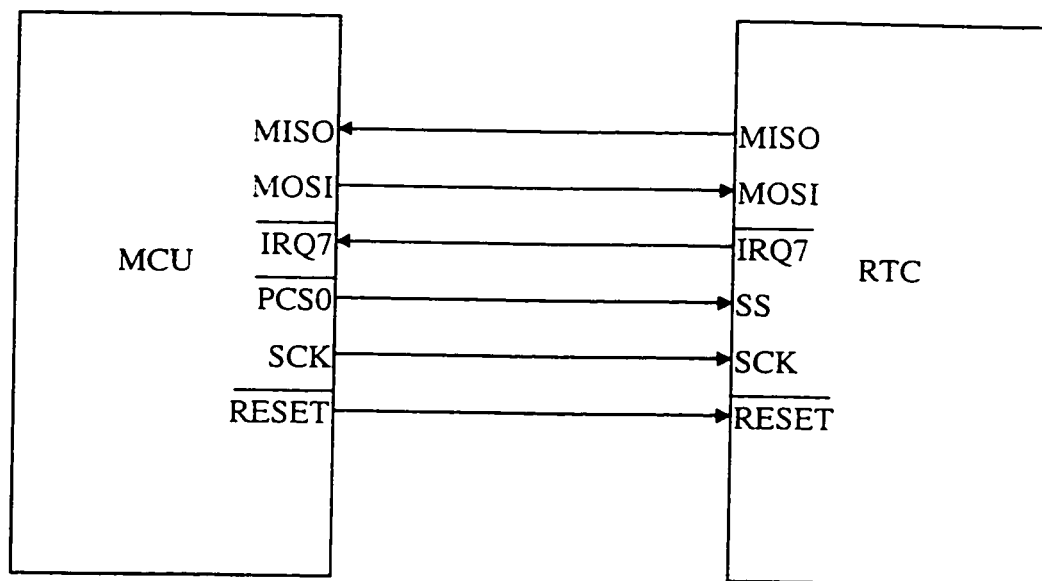


Figure 6-12. The block diagram of the connection between RTC and MCU.

6.4.3. Received Signal Section

The received signal section consists of five components: a multiplexer, a bandpass filter, a RMS-to-DC integrated circuit, an active low pass filter and phase detection circuit.

6.4.3.a. The Multiplexer (MUX)

The multiplexer, MAX399, is a dual 4-channel CMOS analog device. It has low on-resistance ($<100\Omega$) and the on-resistance is matched to within 4Ω between the 4 channels. The switching speed of the analog switch is very fast (transition time less than 250ns). The power consumption of this IC is very low ($<300\mu\text{W}$). One multiplexer can

be used for two receivers. The I/O lines PD4 and PD5 from the microcontroller select the channel-X, -Y, and -Z in a receiver. Also, the I/O lines PF1-3 are used to activate the receiver channel X-Z, respectively. Table 6-4 shows the truth table for PD4-5, PF1-3 and the received channel X-Z.

Table 6-4. The truth table between PD4-5, PF1-3 and the receiver channels.

PD4	PD5	PF1	PF2	PF3	CH.-X	CH.-Y	CH.-Z
0	0	1	0	0	ON	OFF	OFF
0	1	0	1	0	OFF	ON	OFF
1	0	0	0	1	OFF	OFF	ON

6.4.3.b. The Bandpass Filter (BPF)

The bandpass filter, MAX275, is a continuous-time active filter consisting of two independent 2nd-order sections. Cascading two sections can form a 4th-order bandpass filter. In each section, four external resistors are required. The center frequency can be designed within the range from 100Hz to 300kHz, and is accurate to within $\pm 0.9\%$ over the full operating temperature range (0°C to 70°C). The total harmonic distortion is better than -86dB. Figure 6-13 shows the internal circuitry of one section of the 2nd-order filter. To design a fourth-order BPF with center frequency 12kHz, specific values of resistors are chosen based on the manufacture's data sheet.

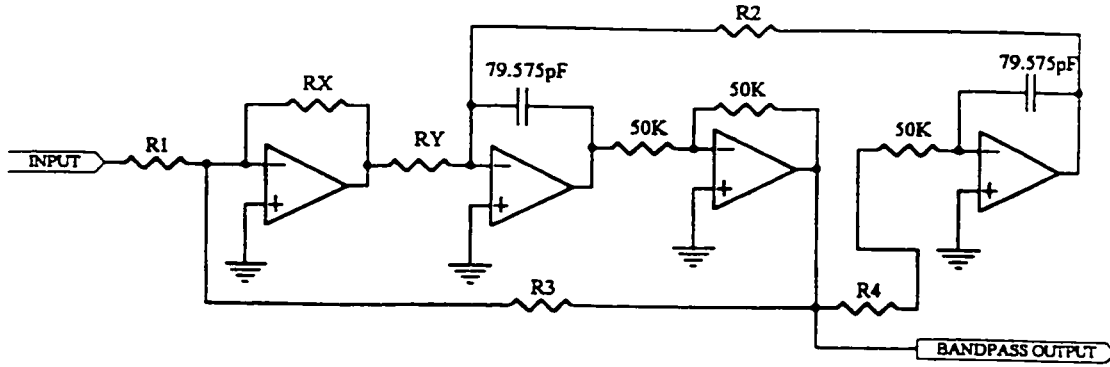


Figure 6-13. The internal circuitry of one section of the 2-nd order filter.

From the data sheet,

$$R_2 = \frac{(2 \times 10^9)}{F_0}, \text{ where } F_0 \text{ is the desired center frequency.}$$

By choosing R_2 to be $165\text{K}\Omega$, sets $F_0 = 12.12\text{kHz}$,

$$R_4 = R_2 - 5\text{K}\Omega = 160\text{K}\Omega$$

$$R_3 = \frac{Q(2 \times 10^9)}{F_0} \times \left(\frac{1}{5}\right)$$

By choosing R_3 to be $330\text{K}\Omega$; sets $Q = 10$, where Q is the quality factor of the complex pole pair.

$$R_1 = \frac{R_3}{H_{OBP}}, \text{ where } H_{OBP} \text{ is the gain of the BPF at } F_0.$$

In the first section, R_1 was a $33\text{K}\Omega$ resistor; therefore, the gain in the first section became 10.

In the 2nd-section, a 50K potentiometer was chosen for R_1 . The gain of this section could be adjusted so that the maximum signal was obtained when the distance between the transmitter and receiver was at the minimum desired value. The resistors R_2 , R_3 and R_4 were chosen as the same values used in section 1.

By cascading these two 2nd-order sections with identical F_0 s and Q s, the resulting Q_t of the 4th-order filter is:

$$Q_t = \frac{Q}{\sqrt{2^{1/2} - 1}}$$

The overall gain of the 4th-order BPF is $\frac{330K}{R_1} \times 10$ and the overall quality factor is 24.

6.4.3.c. RMS to DC Converter

The RMS value of a voltage is defined as: $V_{rms} = \sqrt{\text{Avg.}(V^2)}$. This involves squaring the signal, taking the average, and then obtaining the square root. A RMS-to-DC converter circuit converts an ac signal to a dc signal in which the power or heating value of the ac voltage is the same as the power that produced by the dc signal. For example, if an input signal is a sine wave with its peak voltage equals to 1V, the dc output voltage is then 0.707V.

To select a RMS-to-DC converter, power consumption and external component requirements for the IC were first considered. Among all the commercially available RMS-to-DC converters, the AD736 from Analog Devices was chosen. This IC requires only 200 μ A in supply current and two external components. The disadvantage of this IC was the long settling time requirement (minimum 36ms) when a small averaging error (typically 1%) is required. The longer the settling time, the less the averaging error. A low pass filter (LPF) with the gain greater than 1 amplifies the output signal from the RMS-to-DC converter and the result inputs into the A/D converter. In this application, the averaging error was set to be 0.5%, the corresponding settling time required 50ms.

6.4.3.d. Low Pass Filter

The function of the low pass filter is to remove all undesired high frequency components from the input signal. An active low pass filter usually consists of an op-amp with RC circuit. The gain of the filter can be set either greater than or equal to 1. Figure 6-14 shows the schematic diagram of the active low pass filter with a gain of 1.3. The cutoff frequency of this filter is 15Hz. The gain of the filter multiplies the maximum output voltage (3.8V) from the RMS-to-DC to a 5V value.

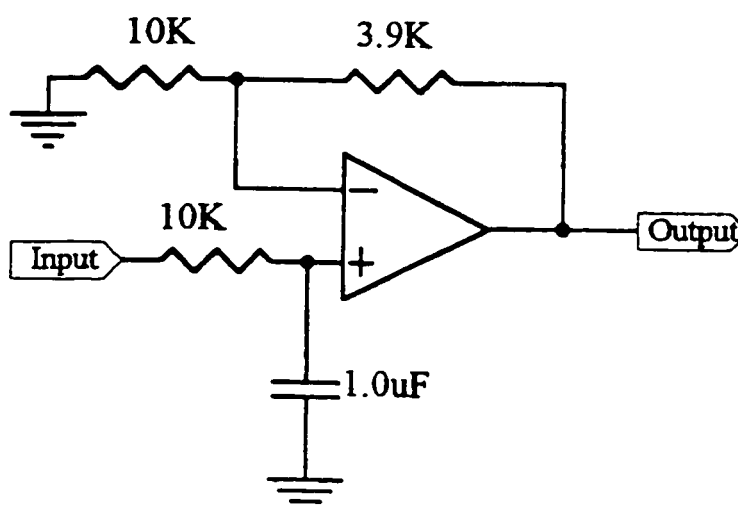


Figure 6-14. The schematic diagram of the active low pass filter.

6.4.3.e. Phase Detection Circuit

The phase detection circuit in this application functions as a zero-crossing detector with hysteresis. Figure 6-15 shows the schematic diagram of the phase detection circuit. When (+) input pin 2 is greater than the (-) input pin 3, the V_{out} is +5V. However, when the (+) input is less than the (-) input, the V_{out} is zero. The 100K and R55 in Figure 6-16 maintain hysteresis of approximately 50mV so that the false output

crossing is minimized. The output signal of the comparator is then input to an I/O pin of the microcontroller. There are three zero-crossing detector circuits in this system, one for the driving signal and two for the received signals. When the microcontroller detects the rising edge from the driving signal, the phase signals of the receivers are recorded. The phase signals can be used to determine the location of the receivers.

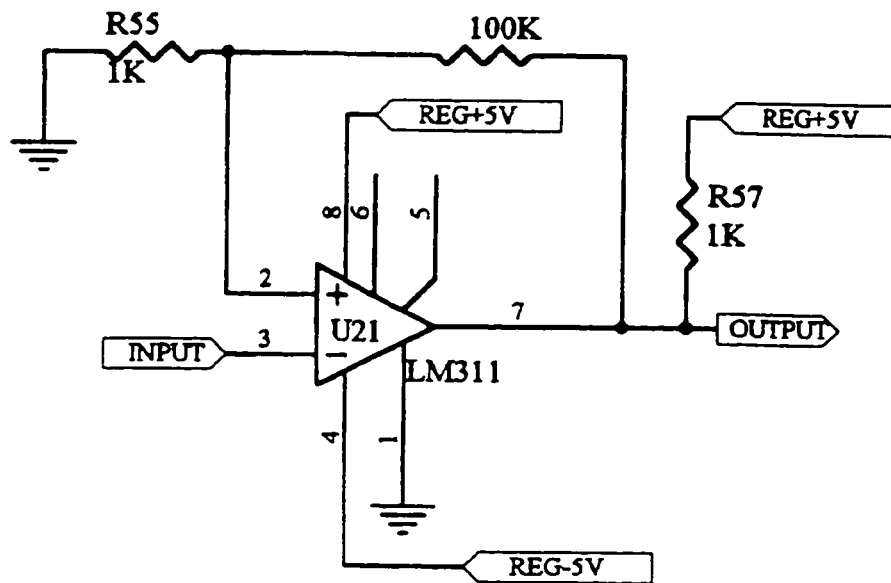


Figure 6-15. The schematic diagram of the phase detection circuit.

6.5. Test of the Received signal sections

To test the received signal section, a small sine wave signal generated from a signal generator, range from 1.28mVp-p to 105mVp-p, was input into the bandpass filter. The input signal emulated a received signal. The 1.28mVp-p signal was the smallest signal that could be generated and the 105mVp-p was the largest signal that could input into the bandpass filter such that the output signal did not saturate. The frequency of the sine wave signal was set to 12.1KHz, which was the center frequency of the designed bandpass filter. The receiver sections for channels 1 and 2 were tested separately.

Output signal from the low pass filter was measured by an oscilloscope. Figures 6-16 and 6-17 show the plotted results on received channels 1 and 2, respectively.

In channel 1, when an input signal was less than 25mV p-p, the gain of the channel 1 varied. However, when the input signal was greater than 25mV p-p, the average gain of channel 1 was 89. Channel 2 had the same characteristics as channel 1, except its average gain was 92. Difference in gain between channels 1 and 2 was due to tolerance of the passive components. Also, the output signals from both channels were linearly proportional to the input signal when the input was greater than 25mVp-p. All the input and output measurements were done by a HP oscilloscope. The gain from channels 1 and 2 varied on small input signals because the reading of small signals from the measurement instrument (HP-oscilloscope) was inaccurate. There was $\pm 4\%$ error in measuring small input signals from the oscilloscope.

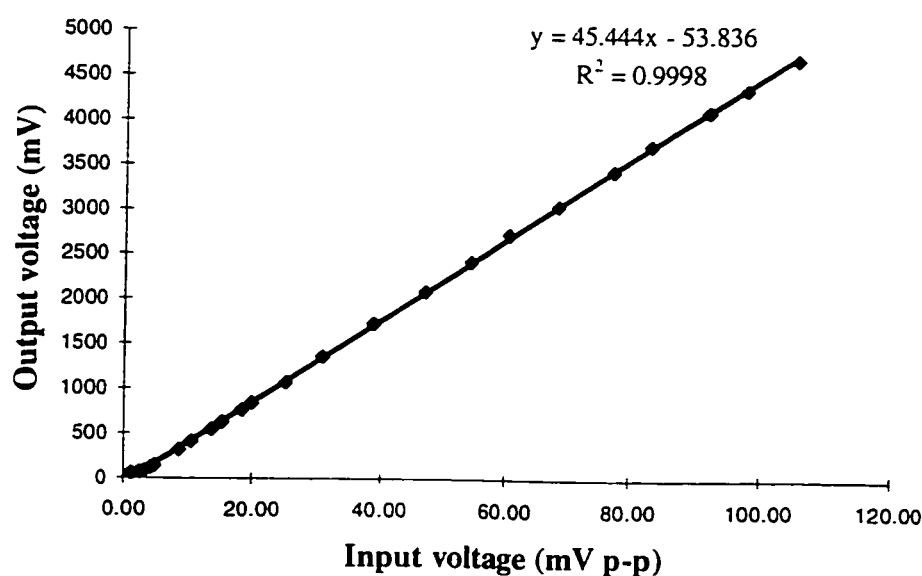


Figure 6-16. The output voltage from the low pass filter versus the input voltage on the bandpass filter of the channel 1.

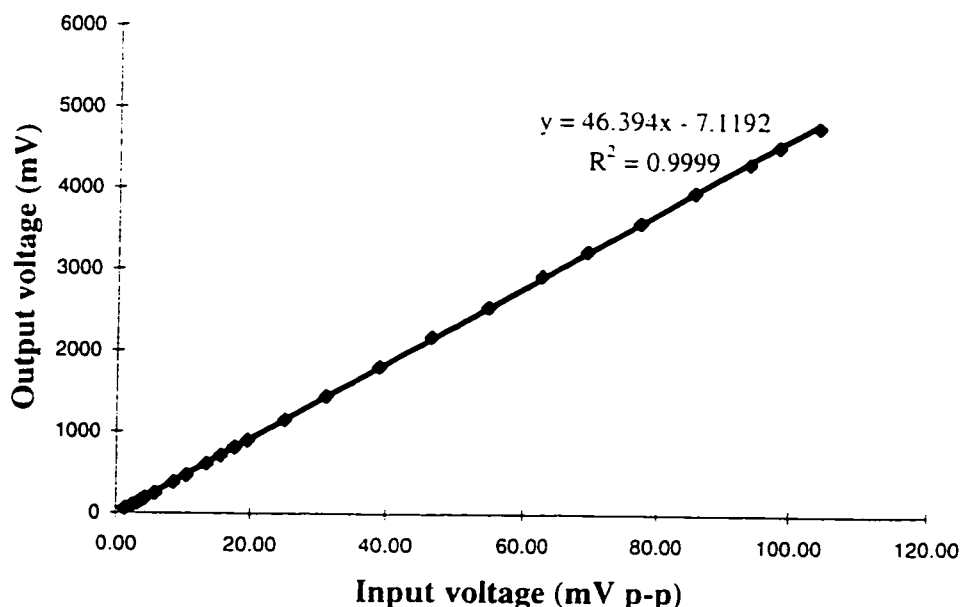


Figure 6-17. The output voltage from the low pass filter versus the input voltage on the bandpass filter of the channel 2.

6.6. Power Consumption

Power consumption is one of the major concerns in the system design. To minimize the power consumption, the number of ICs which provided all the requirements to the system was chosen carefully. Also, any circuit that was not in use was turned off to save power. There are three operating modes in this system: setup mode, sample mode and sleep mode. Since the supply voltage only requires a constant voltage range between 7 to 9V, the supply current can be used to represent power consumption. To determine the current required by the system, the three operating modes are investigated. Setup mode allows users to input all the required parameters. Both the transmitter and the receiver circuits are turned off, but the microcomputer system is turned on. Sample mode is the stage that the designed system acquires samples. All the ICs and circuits are turned on. Sleep mode is the power saving mode; only the RTC IC is on. The system waits for

an interrupt from the RTC to awaken the microcontroller and to collect sample. Power consumption at this stage is the minimum. Current consumption at each stage is reported in Table 6-5. Also, the average current consumption required by the system over a day is calculated. This calculation was based on a sample every 15 minute interval.

Table 6-5. The current consumption of the system at each stage.

Stage	Current consumption (mA)
Setup mode	80.5
Sample mode	200.0
Sleep mode	3.0

The average current consumption over a day, is based on the time required for setting up the parameters (setup mode), and taking a sample with 2 channels (sample mode), and the time period between each sample mode (sleep mode), is 82.56 mA. Since the setup mode only occurs once during the whole measurement period, the current consumption at that stage may be ignored when compared to one day period.

6.7. Justification Different Types of Batteries

Battery power is normally used with portable electronic devices such as cellular phones, video cameras, "Walkman", "Dicsman", pagers and etc. Batteries may be broadly divided into two categories chargeable and non-chargeable batteries. Within these two categories, there are many different types of batteries and their prices can range from a few dollars to a few hundred dollars. In this research, the system is intended to be used over a long period of time and so a rechargeable battery is most appropriate. On selecting the type of rechargeable battery, the charge and discharge characteristics, the weight of the battery, and the cost are the major considerations. The types of batteries

most commonly used are Nickel Cadmium (NiCd), Nickel metal hydride (NiMH) and solid-state Lithium-ion (Li-ion). Table 6-6 shows the characteristics among these three types of batteries. Figure 6-18 shows the discharge curves of these three types of battery. The NiCd type battery has the largest discharge capacity with the highest discharge rate of the three, while the Li-ion has the smallest discharge capacity. Also, the flat discharge profile on both NiCd and NiMH implies that both types of battery have small voltage drop before they require recharging. Among the three, the Li-ion is the most expensive type of battery and the NiCd is the least. One more advantage of both the NiMH and the Li-ion is they have memory free charging characteristic, patients can recharge the system every night after they use the system for a day. Therefore, by comparing the charging and discharging characteristics, the weight and the cost of these three types of battery, the NiMH type battery was chosen for this application.

Table 6-6. The characteristics of the NiCd, NiMH and Li-ion types battery.

	NiCd	NiMH	Li-ion
Energy density (Whr/kg)	40	60	90
Energy density (Whr/l)	100	140	210
Self-discharge rate/month	15% of capacity	25% of capacity	5% of capacity
No. of recharge cycles ¹	1000	800	1000
Price level	Lowest	Moderate	Highest
Charging Characteristic (before recharge)	Need completely discharge	Memory free - no need to completely discharge	Memory free - no need to completely discharge
Operating cell voltage (V)	1.2	1.2	3.6 (average)
Internal resistance	Lowest	Moderate	Highest
Discharge rate (C) ²	<10	<3	<2
Discharge profile	Flat	Flat	Sloping

¹ Defined as the battery's achieving 80% of its initial charge capacity on recharge.

². C =nominal capacity.

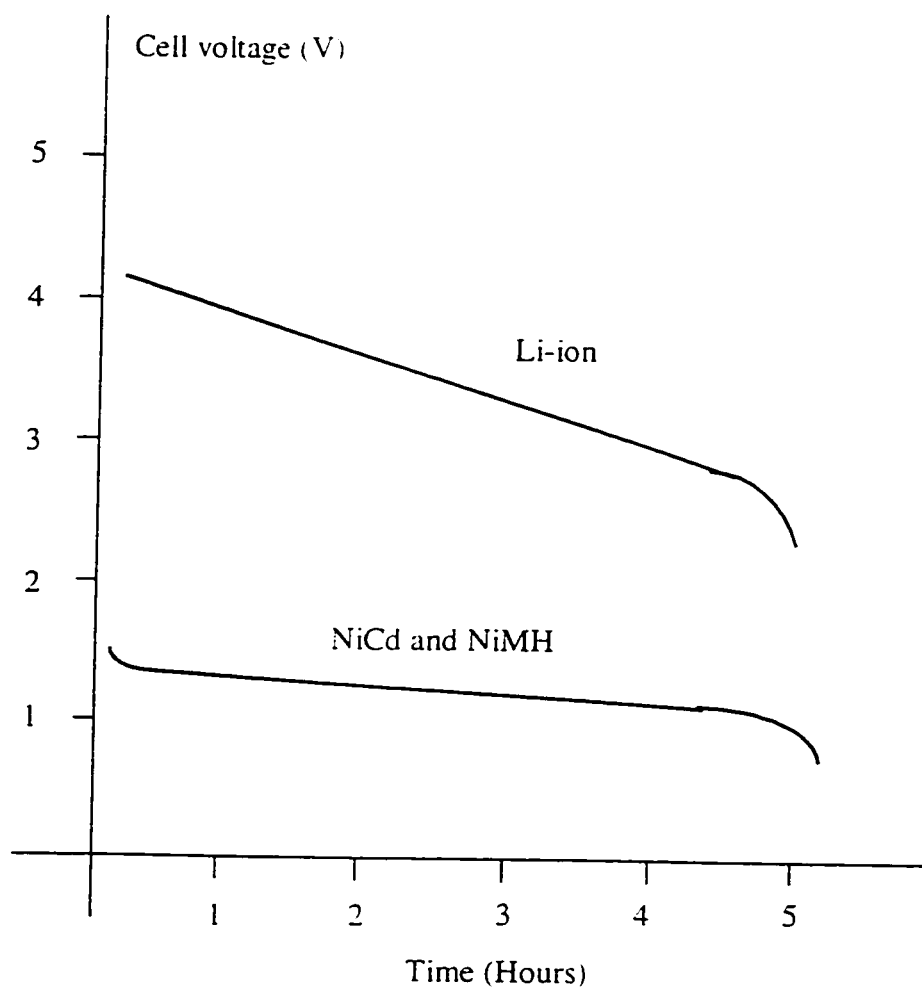


Figure 6-18. The discharge curves of the NiCd, NiMH and Li-ion batteries at 0.2C rate.

6.8. Software Development

The designed system requires three programs to operate the system. The main program controls the hardware to collect, store and analysis data, which was written in assembly language. Interface program allows communication with a PC. Only simple input is required to initialize the system. The S-record conversion program is to simplify the step to store the main program into ROM. The interface program and the S-record conversion program are written in C++ language and both of them are window-based executable programs. The S-record program was only for development and will be described in appendix B. The first two programs have been described in the following.

6.8.1. Main Control Program

After a hardware reset of the system, the main control program starts with the INIT routine. The flowchart of the INIT routine is shown in Figure 6-19 and the routine initializes the stack pointer, the exception vector, external ROM and RAM addresses, the system clock, the RTC and the serial communication. The A/D converter is enabled and selected with 10-bit resolution. The GPT is configured as I/O control lines. Also, the pulse width modulation A in the GPT module is enabled to drive a buzzer. Variable registers are reset in this stage. Following device initialization, the program checks the low battery indicator signal. If the low battery signal is on, the system turns to a low power stop mode (LPSTOP) and a message is displayed on the monitor. A low power red indicator LED is also turned on to alert patients either to change or to recharge the battery. However, if the power is ready, the MAIN routine executes.

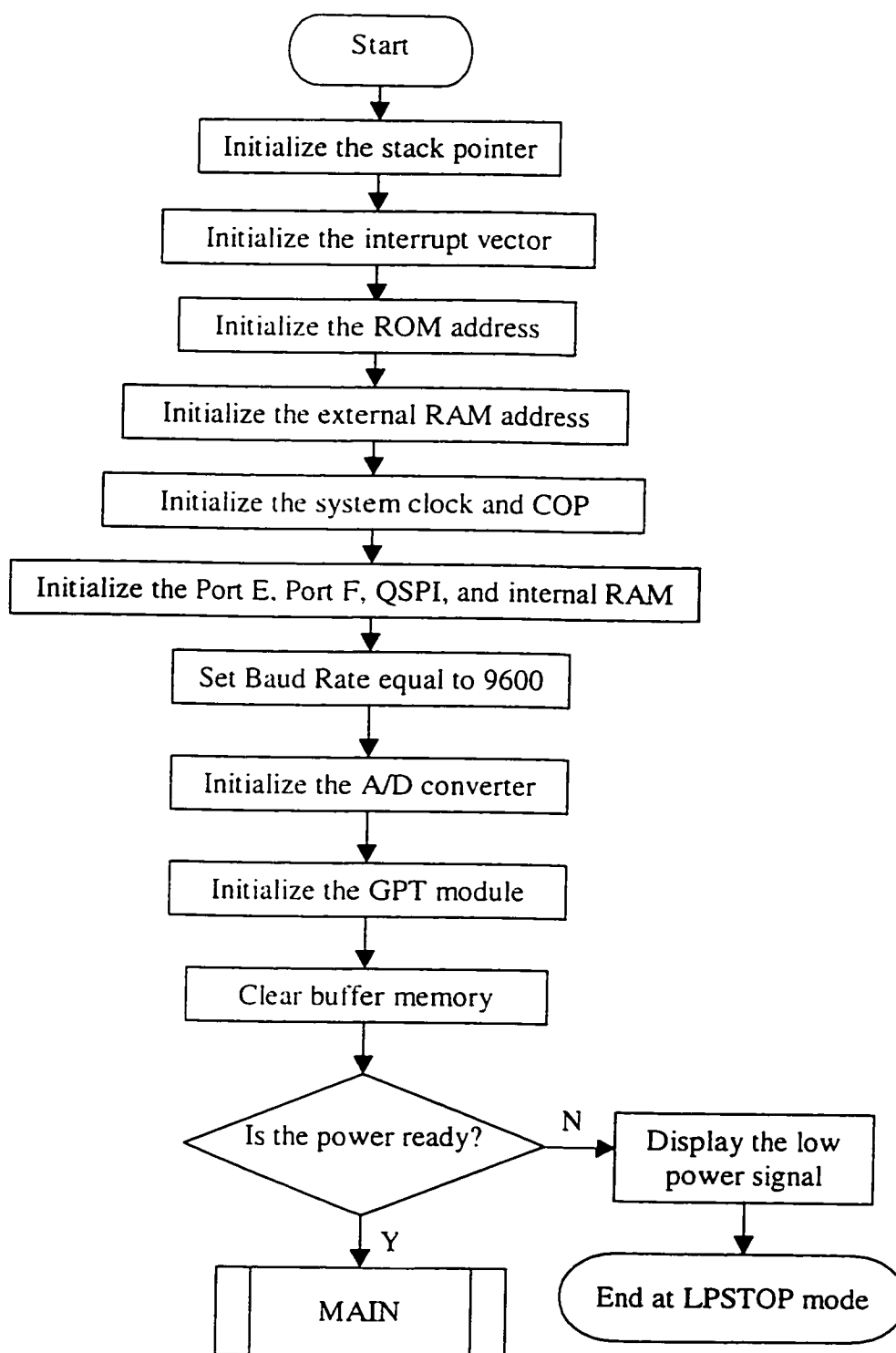


Figure 6-19. The flowchart of the INIT routine.

6.8.2. MAIN routine

This MAIN routine allows users to choose three operation modes: case 1 - INPUT mode, case 2 - Calibration mode, and case 3 - Output mode. Figure 6-20 shows the flowchart of the MAIN routine. Each case is an independent subroutine so that any modification in one subroutine does not affect the other two. The input at this stage must match the pre-defined characters, hence any improper inputs result in re-entering the characters.

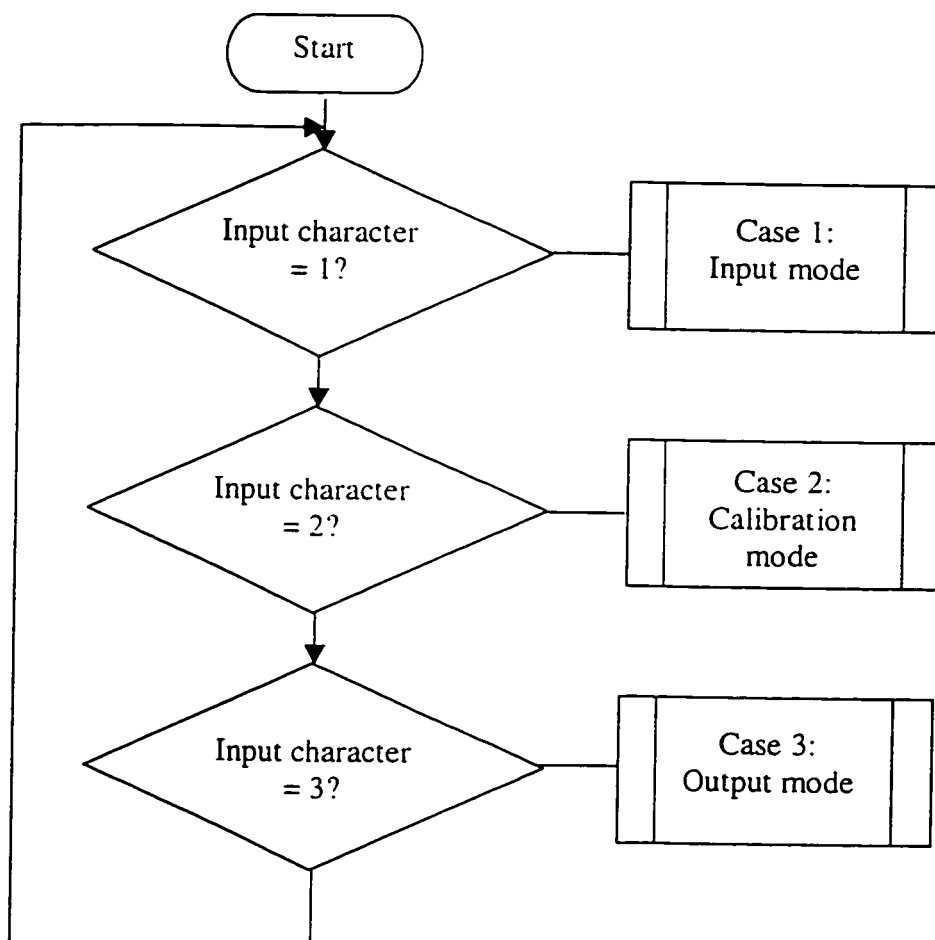


Figure 6-20. The flowchart of the MAIN routine.

6.8.3. INPUT mode

The flowchart for the INPUT mode is shown in Figure 6-21. The routine is executed when the key “1” is pressed in the MAIN routine. The program jumps to the IN_CONV subroutine (Figure 6-22) to convert ASCII numbers (the sample interval input) into hex numbers. The hex numbers are stored and used for the real time clock set up. The sample interval (acceptable input, from 2 seconds to 59 minutes and 59 seconds) is entered at this stage. There is no definite sample interval defined yet. The sample interval will depend on the frequency that the patients feel comfortable with in responding to the feedback signal. Therefore, the sample interval will be defined after clinical trials. At the first trial, the sample interval will be set to a 15 minute- interval. After these parameters are stored, the interrupt configuration is activated. Then, the 232-serial driver is turned off to save power. The initialization of the RCT is executed. The RTC and the MCU communicate via the QSPI of the QSM module. The alarm time is set. All the submodules are turned off to save power. The system then enters a low-power stop (LPSTOP) mode and waits for an external interrupt to awaken the microcontroller. The IRQ routine executes when an interrupt occurs due to the alarm time matching the current time.

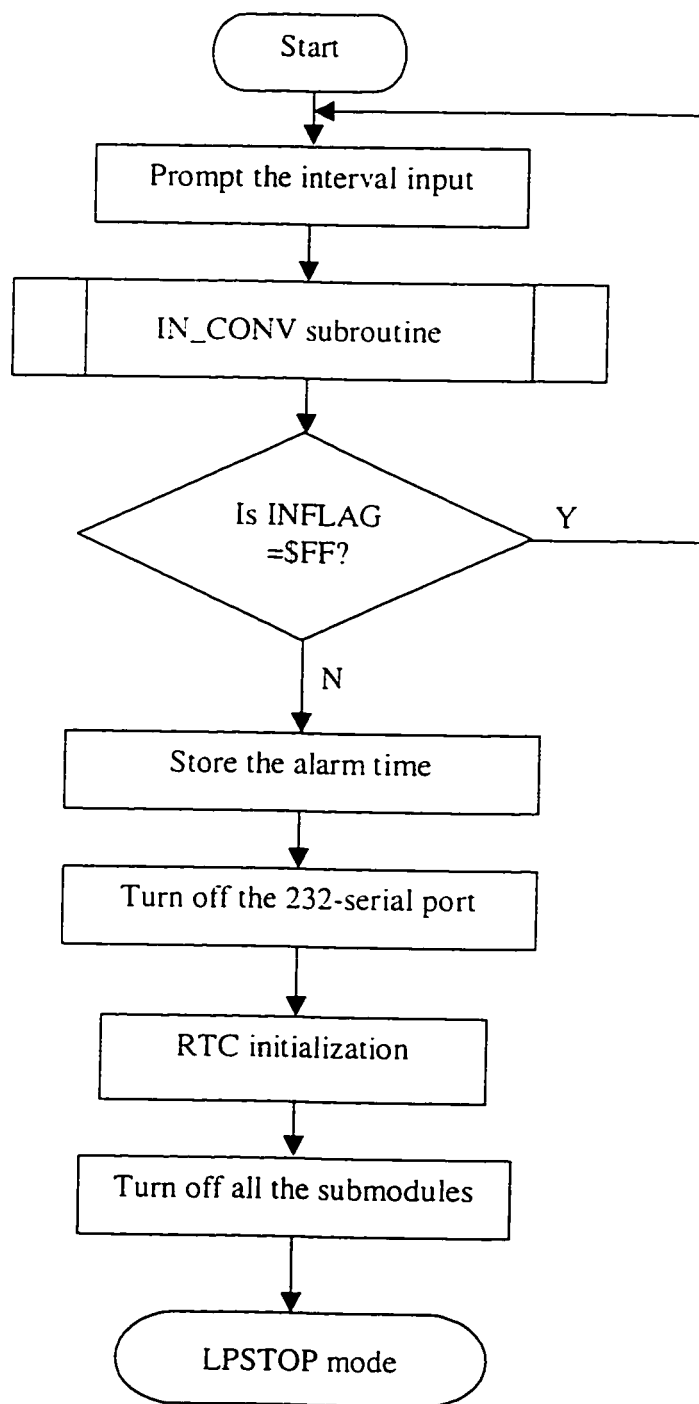


Figure 6-21. The flowchart of the INPUT mode routine.

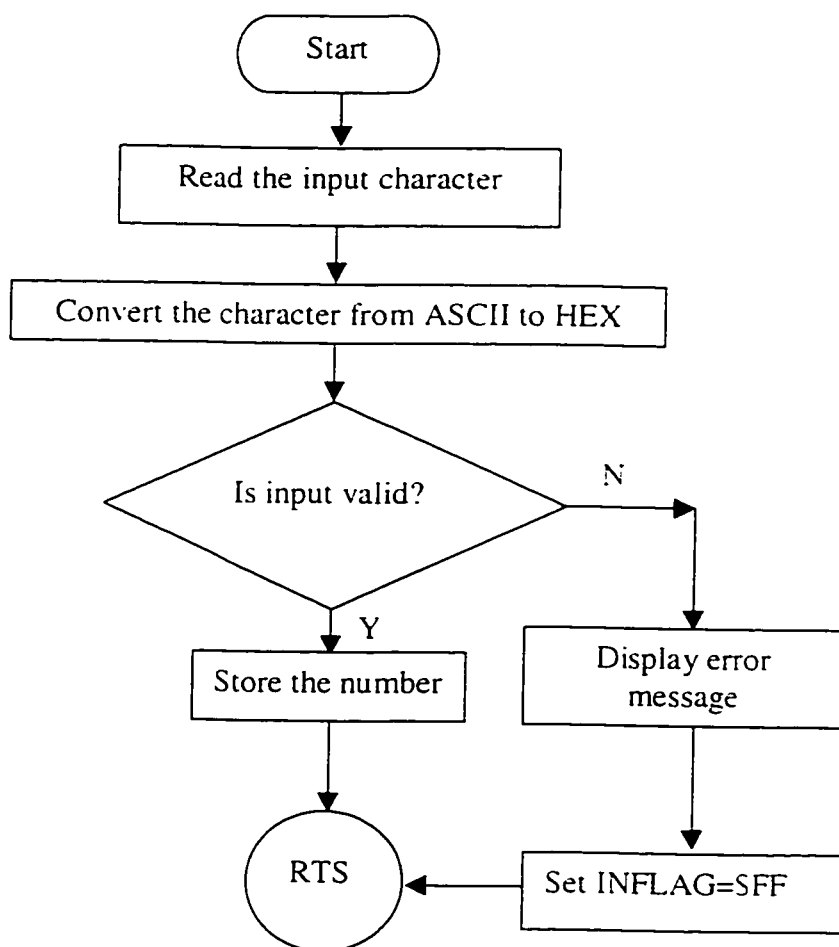
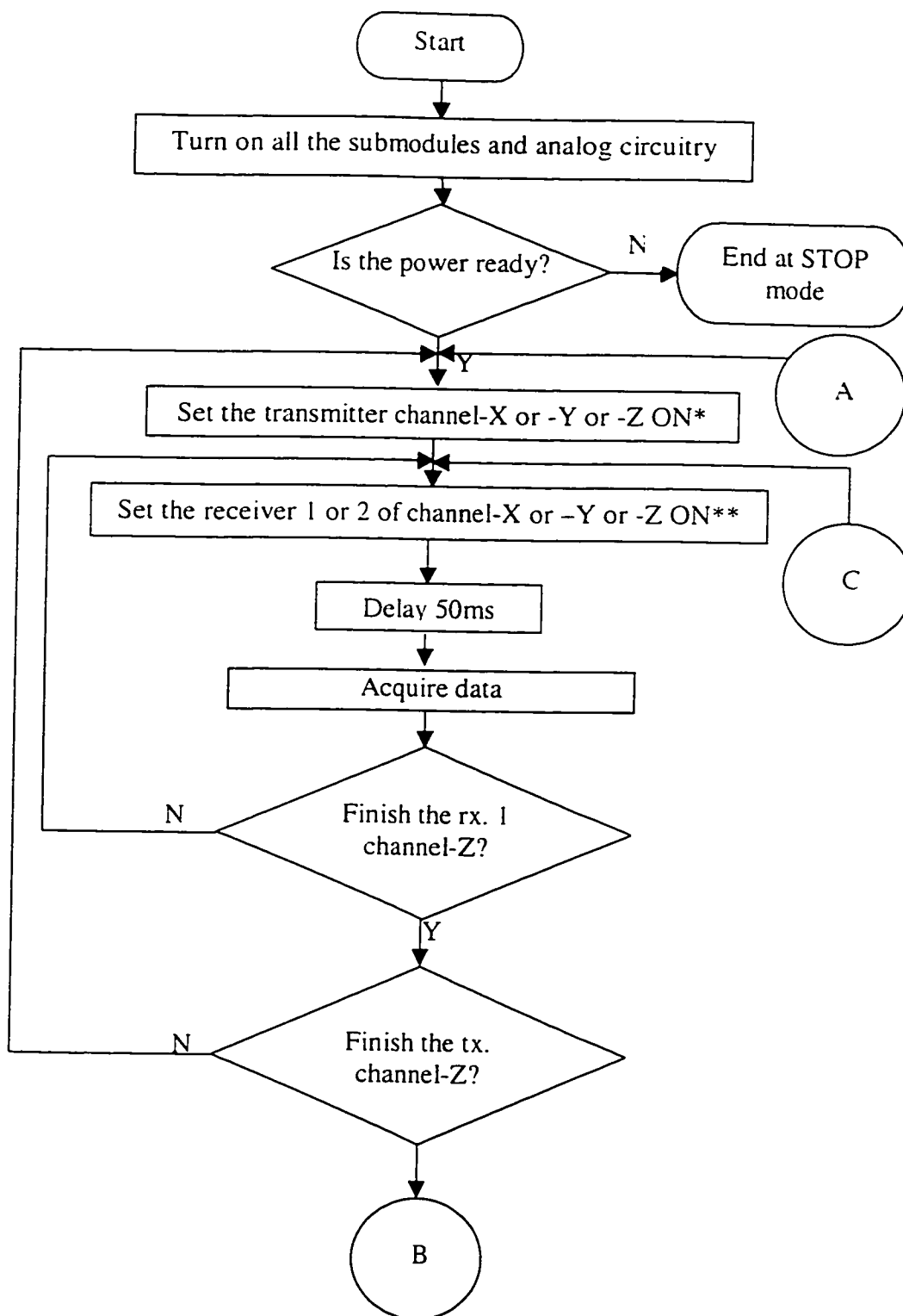


Figure 6-22. The flowchart of the IN_CONV subroutine.

6.8.4. IRQ routine

When the interrupt service routine is executed, all submodules of the microcontroller will be turned on again. Power level and its stability are checked before taking any samples. Figure 6-23 shows the flowchart of this interrupt subroutine. When the power is ready, the channel-X of the transmitter is turned on. Then channel-X of the receiver is activated to receive the signal. A time delay of 50ms is added before data is collected by the A/D converter so that settling time for the RMS-to-DC converter is sufficient. Then the channel-X of the receiver is turned off and simultaneously the

channel-Y of the receiver is turned on. Similarly, another 50ms time delay is added before data is collected. Then the program proceeds to channel-Z of the receiver. After the acquisition of these three samples, the channel-X of the transmitter is turned off and the channel-Y of the transmitter is turned on. The procedures repeat until the channel-Z of the transmitter is turned off. In total nine measurements are obtained from one receiver. Data is stored in the external static RAM for later analysis. If more than 1 receiver is used, the sample procedures repeat until another 9 measurements are collected for each receiver. The position and orientation of all the receivers relative to the transmitter are calculated by using look-up-tables (LUT) and interpolations. An audio feedback will alert patients to adjust his/her posture if required. Then the system goes back to sleep mode again until the next interrupt.



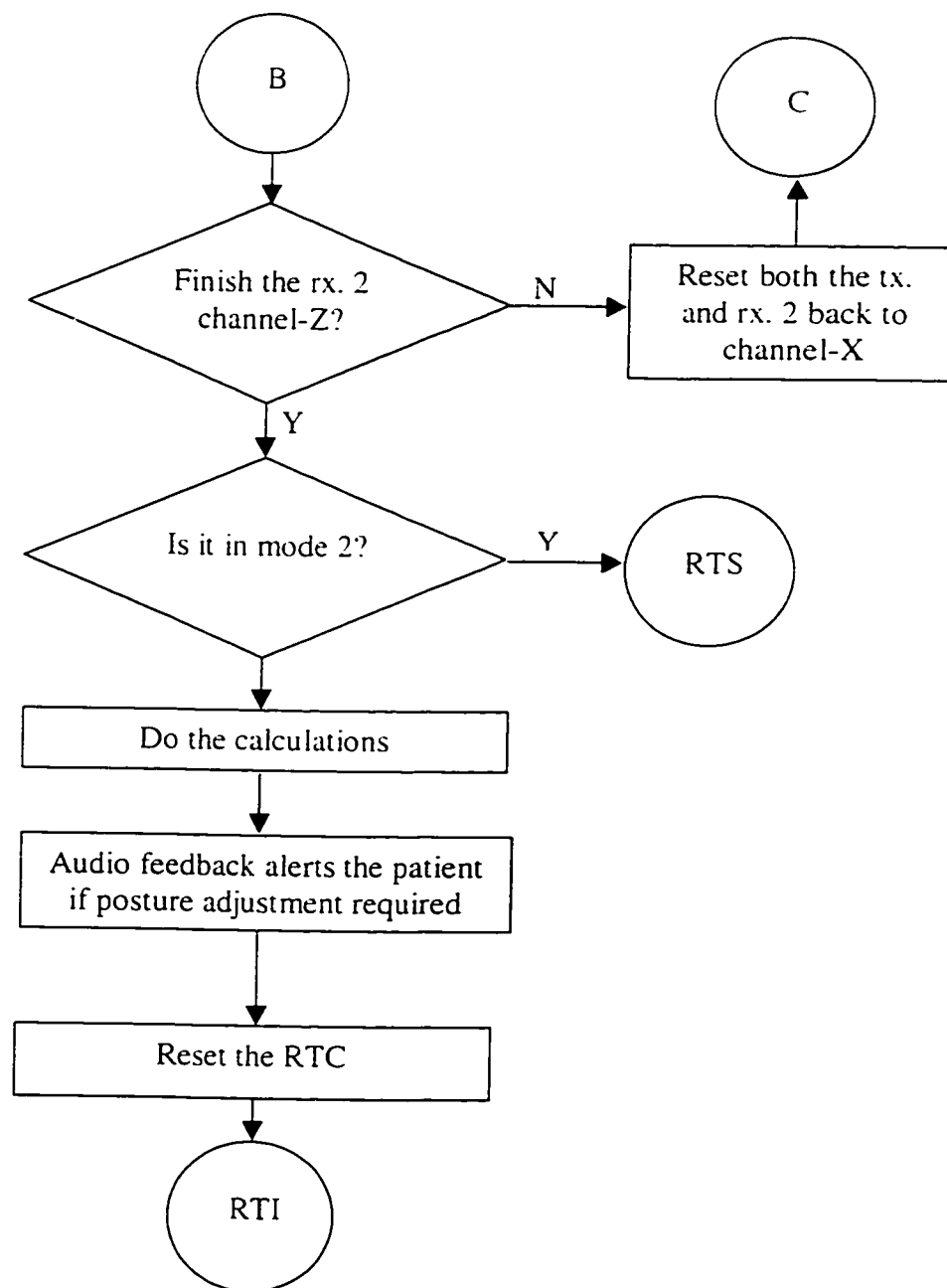


Figure 6-23. The flowchart of the IRQ routine.

6.8.5. CALIBRATION mode

The system executes the calibration mode when the key “2” is pressed in the MAIN routine. Figure 6-24 shows the flowchart of the CASE 2 subroutine. In this mode the 232-serial communication is on all the time. A flag is set to indicate the system is in CASE 2. The system then waits for any key to be pressed to trigger a sample. When a sample is acquired, the system collects the data using the same procedures as that in INPUT mode (CASE 1). But this time the data is stored in the internal static RAM of the microcontroller. After the data is stored, the program returns to the CASE 2 routine and then jumps to the OUTDATA subroutine. The OUTDATA subroutine is also used in the OUTPUT mode (CASE 3) and it will be explained in section 6.8.6. The output data routine with the interface program displays the results – the distance and orientation of all the receivers relative to the transmitter, on the screen. After displaying all the results, the program returns to CASE 2 and waits for another key to be pressed.

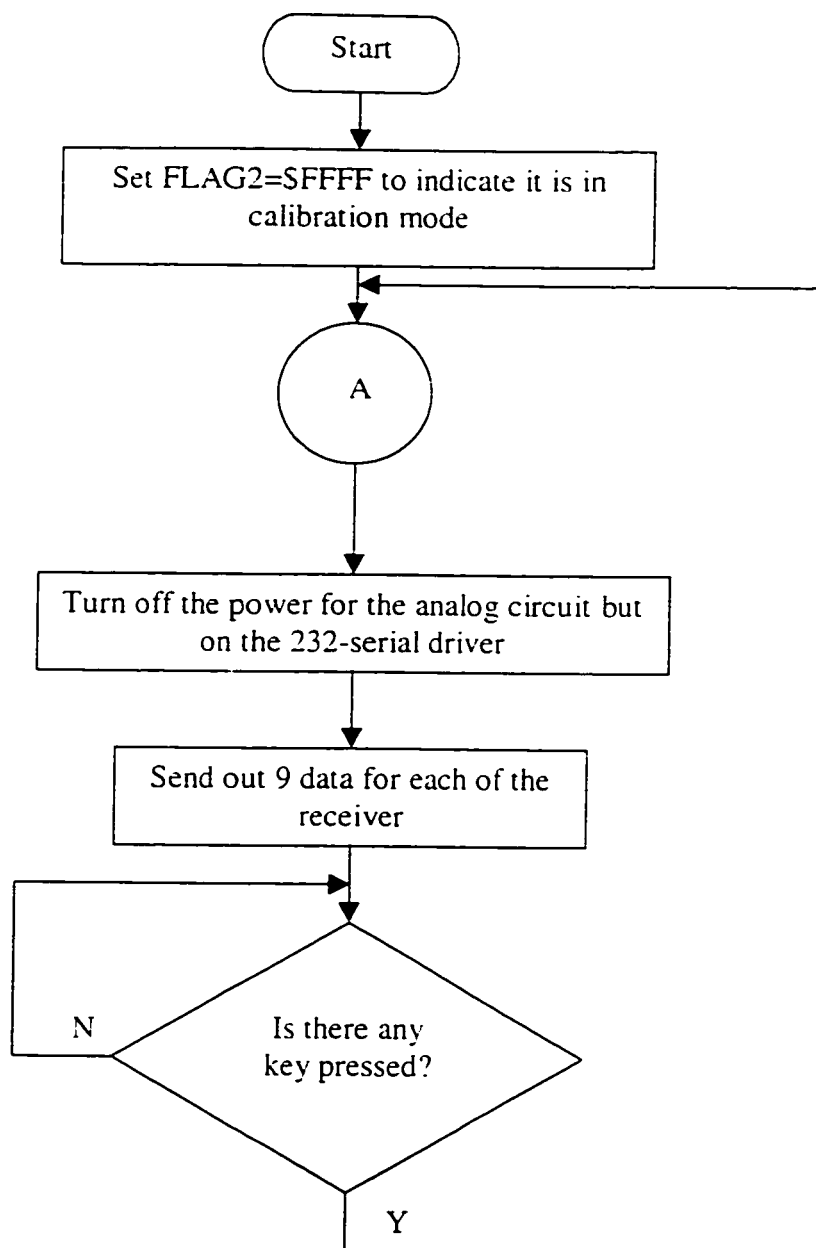


Figure 6-24. The flowchart of the CALIBRATION mode subroutine.

6.8.6. OUTPUT mode

After the key “3” is pressed in the MAIN routine, the OUTDATA subroutine executes. The data in the external static RAMs is retrieved and converted from binary to ASCII. All the data will be downloaded to a host computer and saved into a file. After downloading the data, the system is turned back to the low-power stop (LPSTOP) mode. The data saved in a file will be analyzed and reviewed to investigate how well the patients respond to the system and how their posture changes during their daily activities. If this routine is called from the CASE 2 subroutine, the data will be retrieved from the internal static RAM of the microcontroller and converted into ASCII. An interface program described in section 6.8 will use the data to calculate the position of receivers relative to the transmitter. After the results are displayed on the monitor, the system returns to CASE 2 subroutine.

6.8.7. Interface Program

The interface program, written in the C++ language, is a Windows-based program. This program allows users to select the serial communication port (either port 1 or port 2) on the host computer. Also, the data transferred from the microcomputer system is used to calculate the distance and orientation of receivers relative to the transmitter. The format of the results is: r , θ_z , α_z for each of the receivers. The r is the distance between the center of the transmitter to the center of the receiver, θ_z and α_z are the angles in polar coordinates system. The angle θ_z is the angle made between the z-axis and the line is drawn from the center of the transmitter to the center of the receiver. The angle α_z is the angle made between the x-axis and the line drawn from the center of the

transmitter to the center of the receiver. The results are stored as a text file for later analysis.

6.9. Summary

A low-power portable EM system was developed after a number of innovative improvements. The system consists of one transmitter, two receivers and a microcomputer unit. The dimensions of the microcomputer unit was 4cm x 10cm x 14cm and the weight of this unit was 50g (included the battery pack). The power consumption of the system was 550mW/day. The NiMH battery with 900mAh capacity was chosen so that patients was able to recharge the battery every 10 days if the system was set to be sampled every 15 minutes. Also, the intelligent software allowed the system to start executing automatically after the simple input routine.

7. CALIBRATION PROCEDURES AND RESULTS

This chapter is comprised of four sections. Section 7.1 provides information to establish the distance detection range for the system. Section 7.2 describes the calibration procedures of the system. Section 7.3 presents the implementation of the calibration results into the system. Section 7.4 demonstrates how to calculate a distance and orientation from a set of data.

7.1. The Distance Range

Before starting the calibration, the range of the measured distance must be established. The range of the measured distance depends on which topographical features (refer to chapter 3) are going to be monitored. In a previous study [109], the shoulder height and angles, the scapular asymmetry and the waist asymmetry were the three most significant features that contributed to 75% of the trunk deformity. Among these three features, the shoulder height and angles were chosen as the first features to be monitored. Figure 7-1 shows the position of both the transmitter and receivers on the back surface of a patient. The range of the measured distance was approximately the distance between the midpoint of the pelvis to both shoulders. To investigate the average distance, ninety-three scoliotic images were measured using the video image method described in chapter 3. The images were provided from the scoliosis clinic at Glenrose Rehabilitation Hospital, Edmonton. The ages of the patients were between 10 to 16 years (13.5 ± 2.0), and their Cobb angles were 42.3 ± 6.2 degrees. No one had had spinal surgery. The average distance and the standard deviation between the mid-point of the pelvis to the right shoulder and left shoulder were $345 \pm 43\text{mm}$ and $347 \pm 44\text{mm}$,

respectively. Even though the average distance was about 345 mm, the distribution of the 93 subjects is not in a normal distribution. The histogram of the distribution is shown on Figure 7.2. Both left and right shoulders have similar distribution. Approximately 85% of subjects had a distance over 300 mm. Therefore, the optimal distance range for the system was set between 300mm to 480mm.

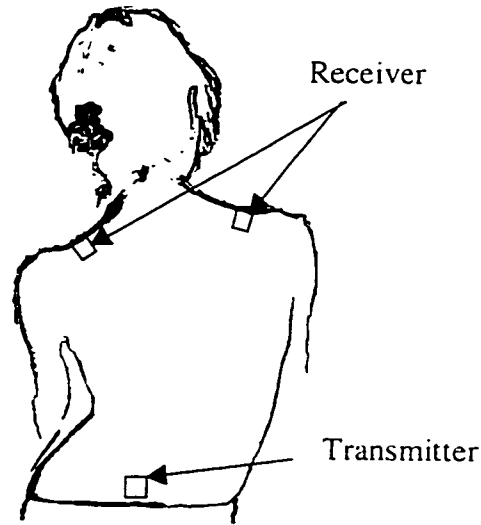


Figure 7-1. The position of the transmitter and receivers at the back of the surface to measure the shoulder asymmetry feature.

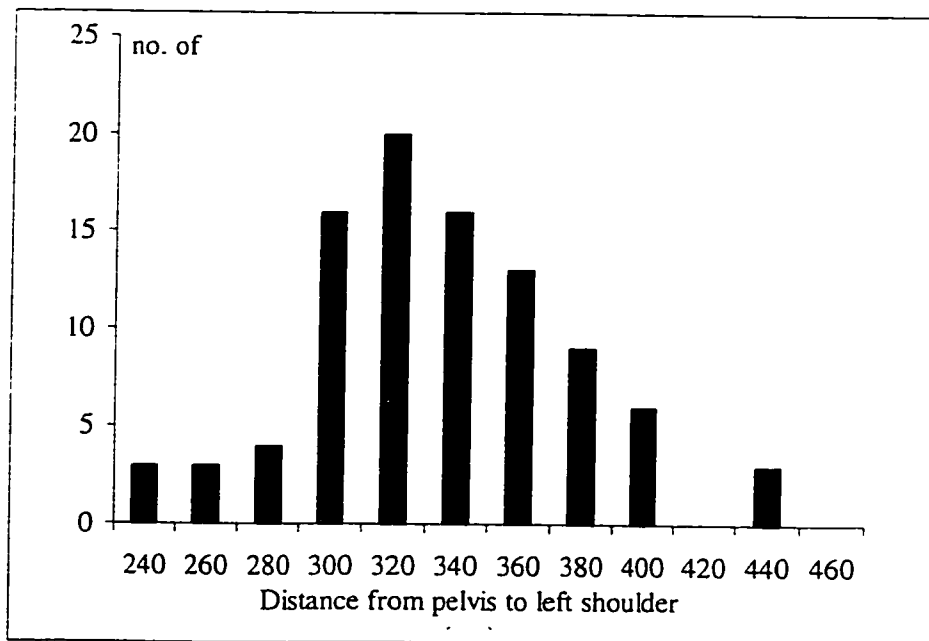


Figure 7-2. The distribution of the distance between the left shoulder and the pelvis.

7.2. Calibration Procedures

A grid map was used to calibrate the system. Figure 7-3 shows the prototype system (inside the black box) with one transmitter and two receivers lying over the map. To calibrate the receiver 1, receiver 2 was fixed at one location and the center of the receiver 1 was placed at the position 30cm away from the center of the transmitter. Figure 7-4 shows the first orientation of the receiver relative to the transmitter. The system was then turned on. The hyper-terminal program in Windows95 was configured to communicate with the prototype system. The system was set in the calibration mode (CASE 2). A key was then pressed on the host computer keyboard to trigger a sample. Nine measurements for receiver 1 and nine measurements for receiver 2 were obtained. The nine measurements are Tx-x (Transmit from x-channel and receives on x-channel), Tx-y, Tx-z, Ty-x, Ty-y Ty-z, Tz-x, Tz-y and Tz-z. Then, receiver 1 was rotated about the y-axis by 90 degrees. A sample was taken again. After that, receiver 1 was rotated in z-axis by 90 degrees, and then rotated about x-axis by 90 degrees again. After each of the rotations, a sample was taken. Four sets of data were obtained at one position. The distance between the center of the transmitter and the center of the receiver was then incremented by 2cm until it reached 48cm. At each of the positions, the same procedures were repeated. After finishing the calibration for receiver 1, the procedures were repeated on receiver 2. At this time receiver 1 was fixed in one position, while receiver 2 was free to move. Four samples each with nine measures were collected at each point. Figure 7-5 shows four sets of data of receiver 1 and 2 at a distance of 32cm. The numbers in each row are in the sequence that defined the nine measurements. Each number is directly output from the 10-bit A/D converter. The first number, 417, on the

first row is the Tx-Rx signal with magnitude equal to 2.07V. The data on the second row is from receiver 2. Since receiver 2 is fixed in a position, the data are almost the same for all four measurements. The processing of the calibration data will be explained in section 7.3 and the calculation of the actual distance and angles will be shown in section 7.4.

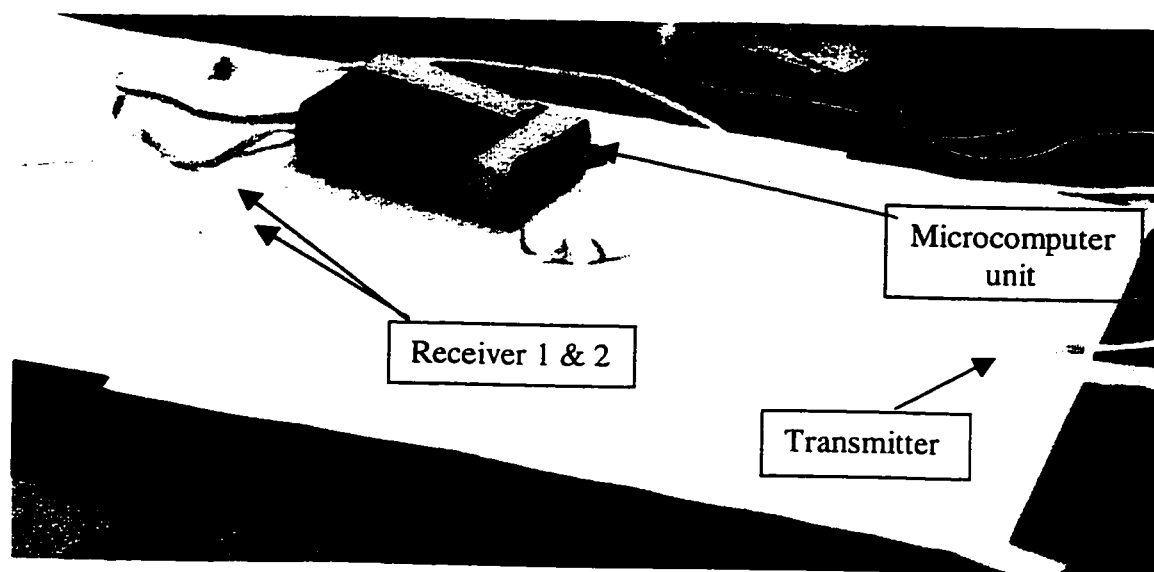


Figure 7-3. The prototype system with one transmitter and two receivers lying over the grid map.

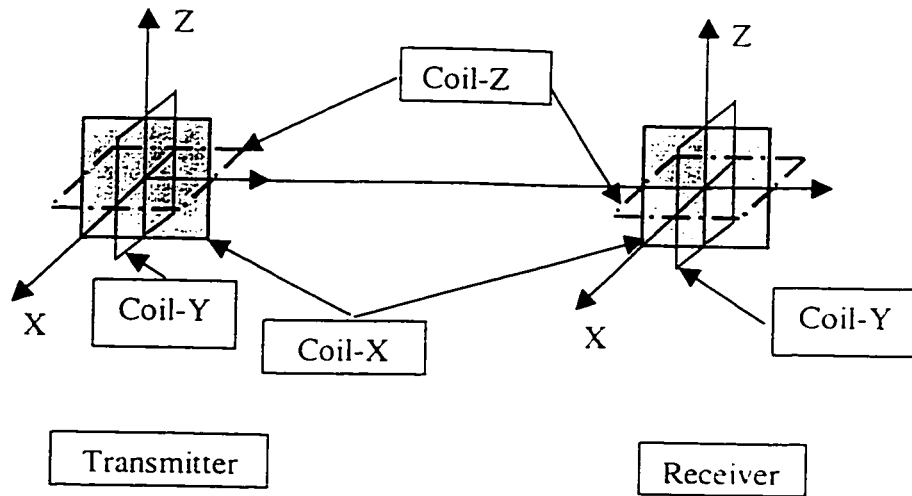


Figure 7-4. The first orientation of the receiver relative to the transmitter.

$$r=32\text{cm}$$

	Tx-x	Tx-y	Tx-z	Ty-x	Ty-y	Ty-z	Tz-x	Tz-y	Tz-z
R1	0417	0052	0064	0053	0794	0131	0035	0071	0412
R2	0785	0845	0108	0522	0270	0050	0085	0114	0550
R1	0062	0439	0055	0765	0099	0032	0026	0043	0413
R2	0782	0848	0103	0522	0266	0048	0085	0112	0546
R1	0048	0055	0464	0057	0781	0114	0358	0047	0048
R2	0781	0847	0106	0523	0268	0052	0086	0112	0548
R1	0420	0009	0036	0038	0094	0846	0009	0378	0052
R2	0783	0849	0109	0522	0267	0051	0084	0111	0550

Figure 7-5. Four sets of data of receiver 1 and 2 at distance 32 cm.

7.3. The Implementation of the Calibration Results for the System

The results from section 7.2 were used to calculate the actual ratio between V_{xx} : V_{xy} : V_{xz} : ... : V_{zz} and the ratio between V_{xR} : V_{yR} : V_{zR} . According to the EM theory, at each of the positions the resultants V_{xR} , V_{yR} , and V_{zR} were constants. Therefore by using three of four sets of the data at one position, the ratios between V_{xx} : V_{xy} : V_{xz} , V_{yx} : V_{yy} :

V_{yz} , and $V_{zx} : V_{zy} : V_{zz}$ could be solved. For example, at distance $r=32\text{cm}$ of the receiver 1, assuming the ratio between $V_{xx} : V_{xy} : V_{xz}$ was $1:a:b$, then

$$417^2 + (52a)^2 + (64b)^2 = V_{xR} = \text{constant } l \quad (1)$$

$$62^2 + (439a)^2 + (55b)^2 = V_{xR} = \text{constant } l \quad (2)$$

$$48^2 + (55a)^2 + (464b)^2 = V_{xR} = \text{constant } l \quad (3)$$

Solving the equations (1) to (3), $a = 0.9484$ and $b = 0.9006$.

Similarly, the ratio between $V_{yx} : V_{yy} : V_{yz}$, and $V_{zx} : V_{zy} : V_{zz}$ were solved to be $1.0442:1.0:0.9444$, and $1.1603:1.1059:1.0$, respectively.

Substituting the values a and b into equation (1), the $V_{xR} = 424.0$. Similarly, V_{yR} and V_{zR} were 805.1 and 421.1 , respectively. Therefore, the ratio of $V_{xR} : V_{yR} : V_{zR} = 1:1.90:0.99$, which was slightly different from the theoretical ratio $1:2:1$. Also, during calibration the distance between the receiver and the transmitter was incremented in 2cm steps from 30cm to 48cm , the ratios of $V_{xR} : V_{yR} : V_{zR}$ at each of the distances were calculated by the same procedures. Tables 7-1 and 7-2 show the ratios $V_{xx} : V_{xy} : V_{xz}$, $V_{yx} : V_{yy} : V_{yz}$, $V_{zx} : V_{zy} : V_{zz}$, and $V_{xR} : V_{yR} : V_{zR}$ of receivers 1 and 2 at each of the calibration distances. Also, the resultant values $V_R = (V_{xR}^2 + V_{yR}^2 + V_{zR}^2)^{1/2}$ is shown on the tables at each of the distances. Look-up-tables were then built based on tables 7-1 and 7-2 and stored in ROMs.

Table 7-1. The ratios between ($V_{xx} : V_{xy} : V_{xz}$), ($V_{yx} : V_{yy} : V_{yz}$), ($V_{zx} : V_{zy} : V_{zz}$), and ($V_{xR} : V_{yR} : V_{zR}$) on receiver 1 at calibration distances.

R	V_R	$V_{xx}:V_{xy}:V_{xz}$	$V_{yx}:V_{yy}:V_{yz}$	$V_{zx}:V_{zy}:V_{zz}$	$V_{xR} : V_{yR} : V_{zR}$
30	1290	1.0:0.949:0.903	1.038:1.0:0.947	1.160:1.104:1.0	1.0:1.054:1.008
32	1062	1.0:0.948:0.901	1.044:1.0:0.944	1.160:1.106:1.0	1.0:1.90:0.99
34	890	1.0:0.952:0.899	1.051:1.0:0.951	1.168:1.121:1.0	1.0:1.053:1.008
36	755	1.0:0.953:0.895	1.059:1.0:0.948	1.168:1.120:1.0	1.0:1.047:1.007
38	644	1.0:0.951:0.892	1.060:1.0:0.951	1.177:1.136:1.0	1.0:1.055:1.004
40	562	1.0:0.945:0.888	1.088:1.0:0.947	1.180:1.138:1.0	1.0:1.045:0.991
42	487	1.0:0.947:0.884	1.058:1.0:0.940	1.174:1.129:1.0	1.0:1.069:0.985
44	428	1.0:0.938:0.882	1.063:1.0:0.938	1.178:1.125:1.0	1.0:1.063:0.982
46	374	1.0:0.940:0.878	1.063:1.0:0.939	1.186:1.149:1.0	1.0:1.064:0.974
48	335	1.0:0.924:0.864	1.065:1.0:0.930	1.188:1.148:1.0	1.0:1.061:0.949

Table 7-2) The ratios between ($V_{xx} : V_{xy} : V_{xz}$), ($V_{yx} : V_{yy} : V_{yz}$), ($V_{zx} : V_{zy} : V_{zz}$), and ($V_{xR} : V_{yR} : V_{zR}$) on receiver 2 at calibration distances.

R	V_R	$V_{xx}:V_{xy}:V_{xz}$	$V_{yx}:V_{yy}:V_{yz}$	$V_{zx}:V_{zy}:V_{zz}$	$V_{xR} : V_{yR} : V_{zR}$
30	1345	1.0:0.980:0.929	1.077:1.0:0.982	1.152:1.090:1.0	1.0:1.066:1.052
32	1107	1.0:0.979:0.928	1.076:1.0:0.980	1.144:1.083:1.0	1.0:1.061:1.046
34	921	1.0:0.965:0.918	1.061:1.0:0.970	1.130:1.076:1.0	1.0:1.065:1.039
36	784	1.0:0.965:0.924	1.057:1.0:0.970	1.100:1.052:1.0	1.0:1.072:1.067
38	666	1.0:0.961:0.920	1.082:1.0:0.990	1.097:1.048:1.0	1.0:1.050:1.062
40	571	1.0:0.954:0.919	1.067:1.0:0.978	1.078:1.029:1.0	1.0:1.059:1.073
42	507	1.0:0.955:0.938	1.075:1.0:0.984	1.108:1.039:1.0	1.0:1.084:1.067
44	441	1.0:0.950:0.939	1.078:1.0:0.993	1.098:1.019:1.0	1.0:1.062:1.059
46	394	1.0:0.978:0.965	1.074:1.0:0.991	1.074:1.007:1.0	1.0:1.088:1.100
48	343	1.0:0.926:0.938	1.090:1.0:1.013	1.070:0.973:1.0	1.0:1.061:1.077

7.4. Calculation Demonstration

Calculations of distance and angles from one set of data (nine measurements) depend on the operating mode. For example, if the data set from the receiver 1 is 0295 0043 0049 0048 0564 0096 0028 0052 0295, and the system is in the sample mode; the following calculations will be done by the microcontroller. First, the system will assume the ratios of the nine data values are all 1. The resultant V_R is then calculated by summing the square of the nine data.

$$V_R = \sqrt{295^2 + 43^2 + 49^2 + 48^2 + 564^2 + 96^2 + 28^2 + 52^2 + 295^2} = 715$$

Then, from the table 7-1, the distance was estimated to be between 36 and 38 cm. Using the ratio of those nine data at the smaller distance (36cm in this case), the values V_{xR} , V_{yR} and V_{zR} are calculated, and the value V_R is computed also. Distance is then calculated by the interpolation method based on the V_R value.

$$V_{xR} = \sqrt{295^2 + (0.9529 * 43)^2 + (0.895 * 49)^2} = 301$$

$$V_{yR} = \sqrt{(48 * 1.059)^2 + 564^2 + (0.948 * 96)^2} = 573$$

$$V_{zR} = \sqrt{(28 * 1.168)^2 + (1.12 * 52)^2 + (295)^2} = 302$$

$$V_{yR'} = 1.047 * 573 = 600$$

$$V_{zR'} = 302 * 1.007 = 304$$

$$V_R = \sqrt{301^2 + 600^2 + 304^2} = 737$$

$$R = \frac{755 - 737}{755 - 644} * (38 - 36) + 36 = 36.3$$

To determine angles of a receiver relative to the transmitter, tables 4-3 and 4-4 in chapter 4 are used. The values a, b and c in table 4-3 must be calculated first.

$$a = \frac{301}{304} = 0.990$$

$$b = \frac{600}{304} = 1.974$$

$$c = \frac{301}{600} = 0.5017$$

Therefore, by using those two tables,

$$\theta_z = 85.3''$$

$$\alpha_z = 90.0''$$

Then the final result is (36.3, 85.3°, 90°).

The actual measurement of the position is (36.5, 88°, 90°).

If the system is in the calibration mode, the nine data will be sent to a host computer.

The interface program calculates the distance and angles based on the EM theory and table 7-1. Since the strength of the received signal is inversely proportional to the cube of distance, R can be calculated from the following:

$$R = \sqrt[3]{\frac{755}{737}} * 36 = 36.4$$

Angle θ_z can be calculated from the equation (47) in chapter 4.

$$\sqrt{3\cos^2 \theta_z + 1} = \frac{304}{301}$$

$$\theta_z = 85.3''$$

Similarly, by using the same method from the equations (48) and (49) in chapter 4, θ_x and

θ_y are calculated to be:

$$\theta_x = 90.0''$$

$$\theta_y = 5.4''$$

Then by substituting θ_x , θ_y and θ_z into equations (50) and (51) in chapter 4.

$$\alpha_{z1} = 90.0'' \quad \text{from equation (50)}$$

$$\alpha_{z2} = 87.3'' \quad \text{from equation (51)}$$

$$\alpha_z = 0.5 * (\alpha_{z1} + \alpha_{z2}) = 88.7''$$

Therefore, the calculated result is (36.4, 85.3°, 88.7°).

7.5. Summary

Topographical trunk features affected by spinal deformity were used to determine the detection range of the system. Shoulder asymmetry was chosen due to the significant contribution to the trunk deformity. The detection range was then defined to be 30cm to 48cm. Calibration procedures were described. Results of the calibration were implemented in the system. A working demonstration in calculating distance and angles from a set of data (nine measurements) were presented. Also, from the ratios $V_{xx} : V_{xy} : V_{xz}$, $V_{yx} : V_{yy} : V_{yz}$, $V_{zx} : V_{zy} : V_{zz}$, and $V_{xR} : V_{yR} : V_{zR}$, the inter-and intra- error factors are within the predicted values. The accuracy of the calculated distance and angle are greater than 97%.

8. LABORATORY MEASUREMENTS AND CLINICAL TRIALS¹

This chapter consists of four sections. Section 8.1 describes the procedures and reports the test results from laboratory experiments. Section 8.2 discusses the test results from section 8.1. Section 8.3 describes the procedures and reports the test results from clinical trials with four subjects. A brief discussion of the clinical test results is presented in section 8.4.

8.1. Laboratory Test procedures and Results

To validate the system, the prototype system was first tested in a laboratory environment. In this test, the receivers 1 and 2 were moved randomly over the grid map while the transmitter was fixed at one position. When the receiver was placed at one location, three measurements were collected at that point in the calibration mode. Polar coordinates (r , θ_z , α_z) of the center of the receivers 1 and 2 were recorded. A ruler and a protractor were then used to measure the actual position of the receivers relative to the transmitter. Receivers 1 and 2 were then moved to other locations and measurements were taken again. Tables 8-1 and 8-2 show the 10 position measurements of both receivers 1 and 2 in which three readings were collected at one position. The actual measurements at each of positions were compared to the three measurements. Tables 8-3 and 8-4 show the comparison between the average distance and angle α_a to the actual measured values on receivers 1 and 2, respectively.

¹ Material in this chapter has been submitted to the International Research Society of Spinal Deformities, Vermont, June 1998 – E. Lou, N. G. Durdle, V. J. Raso and D.L. Hill, "A Posture Measurement System for AIS".

Table 8-1. The comparison of 10 position measurements on receiver 1 with the actual measurement.

Position number	Measurement 1	Measurement 2	Measurement 3	Actual measurement
1	(36.39, 90.0, 74.2)	(36.35, 90.0, 74.3)	(36.42, 90.0, 73.9)	(36.1, 90.0, 75.6)
2	(47.29, 90.0, 76.5)	(47.76, 90.0, 80.0)	(47.48, 90.0, 76.8)	(47.0, 90.0, 81.2)
3	(45.30, 90.0, 29.4)	(45.30, 90.0, 29.8)	(45.28, 90.0, 29.9)	(44.8, 90.0, 27.0)
4	(35.84, 90.0, 85.7)	(35.88, 90.0, 86.0)	(35.76, 90.0, 86.0)	(35.6, 90.0, 82.0)
5	(36.23, 90.0, 66.3)	(36.31, 90.0, 66.4)	(36.28, 90.0, 66.4)	(36.0, 90.0, 65.0)
6	(40.04, 90.0, 61.2)	(39.80, 90.0, 61.3)	(39.77, 90.0, 61.5)	(39.5, 90.0, 63.0)
7	(31.26, 90.0, 66.4)	(31.29, 90.0, 66.3)	(31.25, 90.0, 66.3)	(31.2, 90.0, 65.0)
8	(42.68, 90.0, 68.6)	(42.66, 90.0, 68.5)	(42.53, 90.0, 68.5)	(42.2, 90.0, 70.0)
9	(42.30, 90.0, 58.6)	(42.36, 90.0, 59.0)	(42.34, 90.0, 58.8)	(42.0, 90.0, 57.5)
10	(36.52, 90.0, 6.0)	(36.60, 90.0, 7.9)	(36.57, 90.0, 8.4)	(36.3, 90.0, 3.0)

Table 8-2. The comparison of 10 position measurements on receiver 2 with the actual measurement.

Position number	Measurement 1	Measurement 2	Measurement 3	Actual measurement
1	(37.80, 90.0, 8.1)	(37.82, 90.0, 7.8)	(37.88, 90.0, 7.9)	(37.5, 90.0, 4.0)
2	(44.64, 90.0, 79.3)	(44.76, 90.0, 80.0)	(44.48, 90.0, 76.8)	(44.2, 90.0, 82.0)
3	(38.68, 90.0, 64.5)	(38.70, 90.0, 64.3)	(38.62, 90.0, 64.7)	(38.3, 90.0, 66.0)
4	(40.56, 90.0, 69.3)	(40.49, 90.0, 69.1)	(40.42, 90.0, 69.5)	(40.1, 90.0, 72.0)
5	(49.12, 90.0, 90.0)	(49.64, 90.0, 90.0)	(49.33, 90.0, 90.0)	(48.8, 90.0, 90.0)
6	(45.69, 90.0, 69.4)	(45.72, 90.0, 69.6)	(45.68, 90.0, 69.2)	(45.2, 90.0, 67.0)
7	(34.48, 90.0, 59.7)	(34.49, 90.0, 59.9)	(34.41, 90.0, 59.8)	(34.3, 90.0, 60.5)
8	(30.22, 90.0, 49.5)	(30.21, 90.0, 49.6)	(30.17, 90.0, 49.6)	(30.1, 90.0, 48.5)
9	(36.46, 90.0, 88.7)	(36.57, 90.0, 88.4)	(36.32, 90.0, 86.0)	(36.2, 90.0, 83.0)
10	(47.31, 90.0, 36.5)	(47.37, 90.0, 36.4)	(47.35, 90.0, 36.6)	(46.8, 90.0, 35.0)

Table 8-3. The comparison between the average values of the distance r_a and angle α_a to the actual measured values r_m and α_m on the receiver 1.

Average r_a (cm)	Measured r_m (cm)	$r_a - r_m$ (cm)	Average α_a (degrees)	Measured α_m (degrees)	$\alpha_a - \alpha_m$ (degrees)
36.39	36.1	0.29	74.1	75.6	-2.2
47.51	47.0	0.51	77.8	81.2	-3.4
45.29	44.8	0.49	29.7	27.0	2.7
35.83	35.6	0.23	85.9	82.0	3.9
36.27	36	0.27	66.4	65.0	1.4
39.87	39.5	0.37	61.3	63.0	-1.9
31.27	31.2	0.07	66.3	65.0	1.3
42.62	42.2	0.42	68.5	70.0	-1.5
42.33	41.9	0.43	58.8	57.5	1.3
36.56	36.3	0.26	7.4	3.0	4.4

Table 8-4. The comparison between the average values of the distance r_a and angle α_a to the actual measured values r_m and α_m on the receiver 2.

Average r_a (cm)	Measured r_m (cm)	$r_a - r_m$ (cm)	Average α_a (degrees)	Measured α_m (degrees)	$\alpha_a - \alpha_m$ (degrees)
37.83	37.5	0.33	7.9	4.0	3.9
44.63	44.2	0.43	78.7	82.0	-3.3
38.67	38.3	0.37	64.5	66.0	-1.5
40.49	40.1	0.39	69.3	72.0	-2.7
49.36	48.8	0.56	90.0	90.0	0.0
45.69	45.5	0.49	69.4	67.0	1.4
34.46	34.3	0.16	59.8	60.5	-0.7
30.20	30.1	0.10	49.6	48.5	1.1
36.45	36.2	0.25	87.7	83.0	4.7
47.34	46.8	0.54	36.5	35.0	1.5

8.2. Discussion

From tables 8-1 to 8-4, the results showed that the variations in the distance between the actual and the measured values were increased when the distance between the transmitter and receivers were bigger. This phenomenon occurred because the received signals were decreased when the distance was increased, which implied the signal-to-noise ratio decreased. Also, the variations of the angles between the actual and the measured values were greater when the angles were close to 90 and 0 degrees. This phenomenon occurred because the sine and cosine functions were involved in the calculations. The change in these two functions was very small when the angle was close to 90 or 0 degrees.

The laboratory test only obtained the accuracy in two-dimensional measurements. Figures 8-1, 8-2, 8-3 and 8-4 summarized all the information of the distance and angle errors in channels 1 and 2. The absolute distance error on both channels increased from 0.07 to 0.51cm when the distance between the transmitter and receiver was increased from 30 to 47cm. Also, the relative percentage error increased from 0.03% to 1.1% at the same distance range. The error on the angle measurements depended on the actual position of the receiver relative to the transmitter. If the angle α was close to 0 or 90 degrees, the absolute error was approximately 5 degrees. If the angle α was close to 45 degrees, the error was approximately 1.2 degrees.

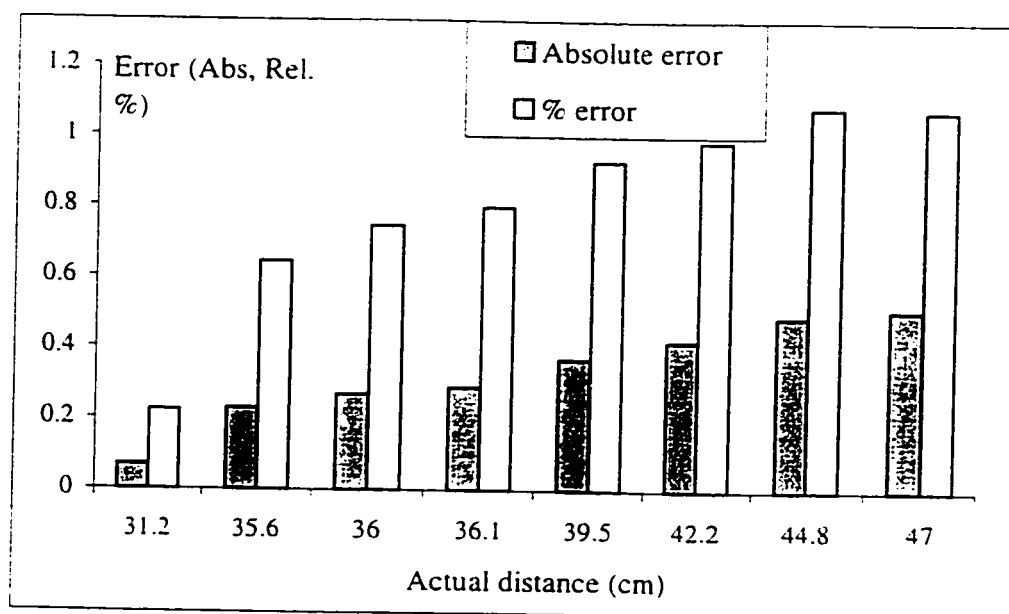


Figure 8-1. The absolute and percentage error of the measured distance at different distances on channel 1.

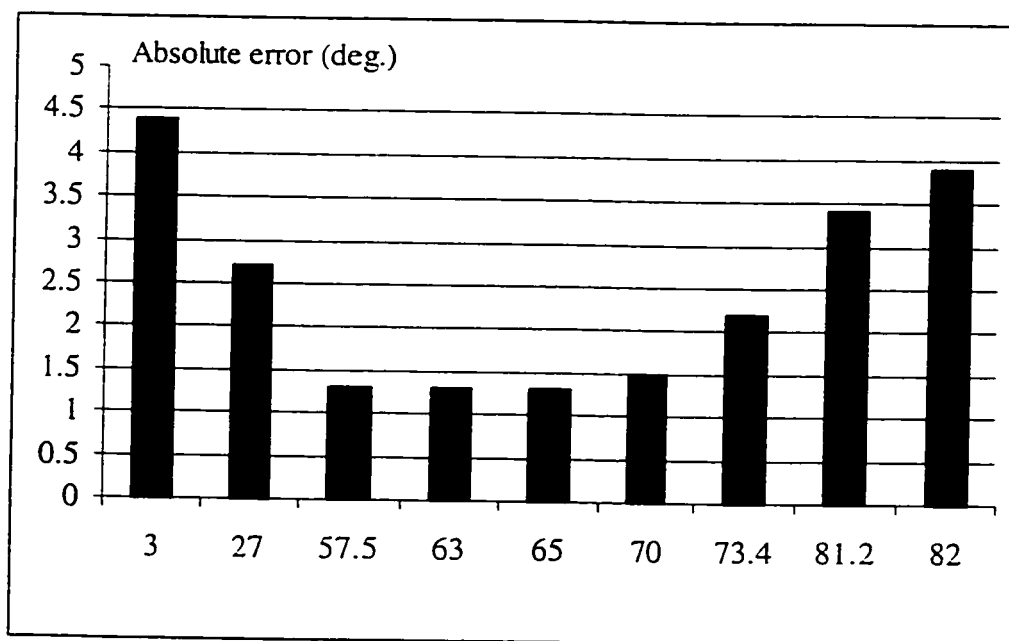


Figure 8-2. The absolute error of the measured angle α at different angles on channel 1.

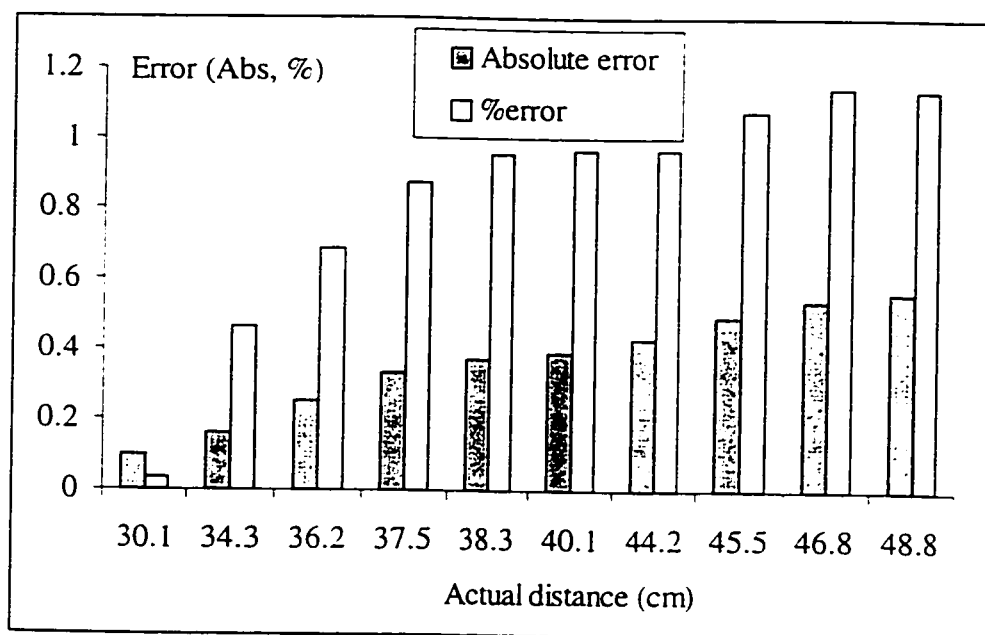


Figure 8-3. The absolute and percentage errors of the measured distance at different distances on channel 2.

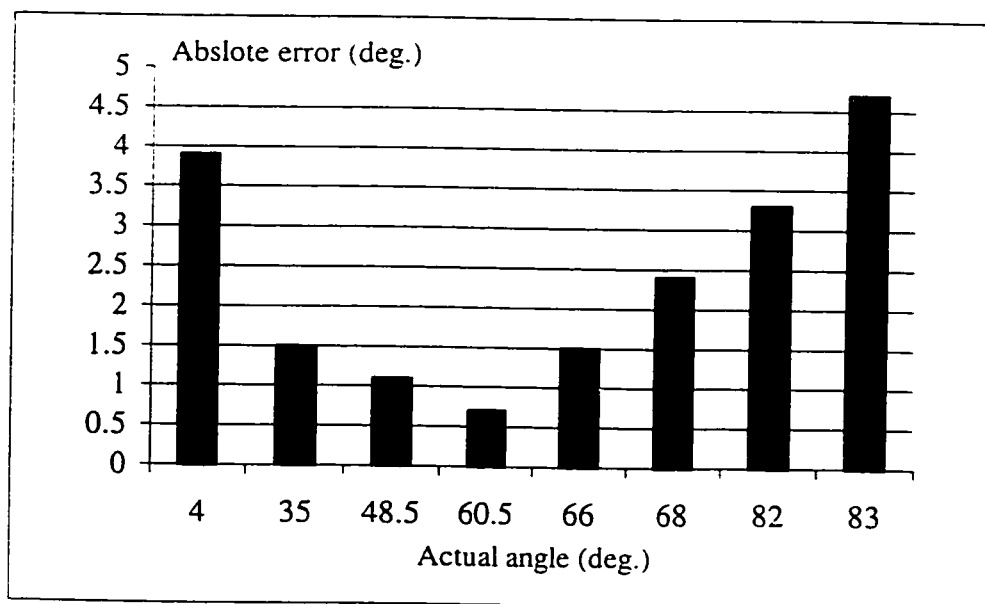


Figure 8-4. The absolute error of the measured angle α at different angles on channel 2.

8.3. Clinical Test Procedures and Results

The objective of this test was to confirm that the system was able to detect postural changes of a subject. During the clinical test, four subjects wore the system and stood in front of the camera with the same set up described in chapter 3. Back images and measurements were taken at the same time to check the accuracy of the system for the three-dimensional measurements. The first feature to be tested was the shoulder asymmetry. Two receivers and one transmitter were placed on each side of the shoulders and the middle of the pelvis, respectively, by using adhesive pads and surgical tape. Before the test, a normal standing image was captured. Then, the subject was requested to perform some movements during the test.

Those movements involved

- a) bending the body to the left and right hand side,
- b) raising and lowering the shoulders (shrugging) on the left and right separately.

All these movements were captured onto a series of images. Figure 8-5 shows one set of images from one subject. The positions of the receivers relative to the transmitter for each movement were measured from the images by the method described in chapter 3. Also, the positions from the posture control system were compared. Four subjects were tested and the results were reported in Table 8-5 to Table 8-8. Table 8-9 summarized the results into three categories: normal standing, shrugging shoulders, and bending body to the side.



Normal

Bend to left

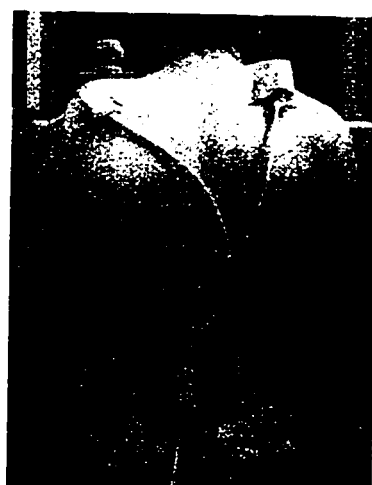
Bend to right



Raise left shoulder



Lower left shoulder



Raise right shoulder



Lower right shoulder

Figure 8-5. One set of experimental test images from a subject.

Table 8-5. The test result of subject 1.

	Left Rx.				Right Rx.			
	Image (Standard)		Posture Measurement System		Image (Standard)		Posture Measurement System	
	r(mm)	α (deg.)	r(mm)	α (deg.)	r(mm)	α (deg.)	r(mm)	α (deg.)
B1	381	70	378	72	367	70	364	69
Rltsh	412	74	414	73	358	68	354	69
Lltsh	386	69	384	69	379	72	376	73
Rrtsh	378	69	379	71	387	74	387	74
Lrtsh	383	70	385	70	364	69	364	68
Blt	386	46	382	45	390	84	386	90
Brt	404	86	399	81	371	46	366	45
B2	391	70	391	68	364	70	365	73
θ	76		78		76		77	

Note:

B1 – Normal standing

Rltsh – Raise left shoulder

Lltsh – Lower left shoulder

Rrtsh – Raise right shoulder

Lrtsh – Lower right shoulder

Blt – Bent to left

Brt – Bent to right

B2 – Normal standing

Angle θ was measured from the normal standing image.

Table 8-6. The test result of subject 2.

	Left Rx.				Right Rx.			
	Image (Standard)		Posture Measurement System		Image (Standard)		Posture Measurement System	
	r(mm)	α (deg.)	r(mm)	α (deg.)	r(mm)	α (deg.)	r(mm)	α (deg.)
B1	360	73	360	75	357	70	361	68
Rltsh	396	80	392	83	348	66	351	63
Lltsh	372	77	368	82	348	66	352	64
Rrtsh	350	71	346	75	397	75	400	72
Lrtsh	344	77	346	74	360	66	362	70
Blt	356	44	351	42	409	77	406	80
Brt	409	73	404	79	331	37	326	41
B2	365	74	362	75	356	71	355	69
θ	81		84		84		82	

Table 8-7. The test result of subject 3.

	Left Rx.				Right Rx.			
	Image (Standard)		Posture Measurement System		Image (Standard)		Posture Measurement System	
	r(mm)	α (deg.)	r(mm)	α (deg.)	r(mm)	α (deg.)	r(mm)	α (deg.)
B1	400	71	398	72	394	76	395	75
Rltsh	424	73	427	75	389	75	391	77
Lltsh	390	70	388	72	410	78	413	81
Rrtsh	394	71	396	73	400	78	403	80
Lrtsh	410	71	414	69	389	74	392	76
Blt	393	40	390	39	430	73	435	76
Brt	417	83	422	86	383	49	377	50
B2	393	72	395	72	392	75	394	75
θ	73		70		75		78	

Table 8-8. The test result of subject 4.

	Left Rx.				Right Rx.			
	Image (Standard)		Posture Measurement System		Image (Standard)		Posture Measurement System	
	r(mm)	α (deg.)	r(mm)	α (deg.)	r(mm)	α (deg.)	r(mm)	α (deg.)
B1	364	72	364	74	369	72	365	74
Rltsh	381	75	385	73	370	70	365	74
Lltsh	363	72	363	75	369	71	367	72
Rrtsh	372	72	372	76	395	74	391	72
Lrtsh	378	75	374	72	360	69	357	74
Blt	357	55	357	50	382	89	378	90
Brt	384	89	388	86	363	66	359	64
B2	368	72	368	74	369	73	366	74
θ	77		79		76		75	

Table 8-9. Summary of the test results.

Category	Distance Measurements (mm)			Angle Measurements (α) (degrees)	
	Mean value \pm S.D.	Mean absolute error \pm S.D.	% error \pm S.D.	Mean value \pm S.D.	Mean absolute error \pm S.D.
Normal Standing	374 \pm 15	1.8 \pm 1.4	0.5 \pm 0.5	72 \pm 2	1.5 \pm 0.8
Shrugging shoulders	380 \pm 20	2.6 \pm 1.5	0.7 \pm 0.4	72 \pm 4	2.3 \pm 1.3
Bending	385 \pm 26	4.2 \pm 1.4	1.1 \pm 0.4	65 \pm 19	2.9 \pm 1.8

Category	Angle Measurements (θ) (degrees)	
	Mean value \pm S.D.	Mean absolute error \pm S.D.
Normal Standing	77 \pm 4	2.1 \pm 0.8

8.4. Discussion

From tables 8-5 to 8-8, the results showed that the measured values r , θ , and α from the posture control system agreed with that from the images. B1 and B2 were the images where the subjects were standing normally. Rltsh, Lltsh, Rrtsh and Lrtsh were the images where the subjects raised or lowered their left and right shoulders. Blt and Brt were the images where the subjects were bending to the left and right hand sides. From table 8-9, the distance and angle errors were 1.8 ± 1.4 mm and 1.5 ± 0.8 degrees when the subjects were standing normally. When the subjects raised or lowered their shoulders, the distance and angle errors were 2.6 ± 1.5 mm and 2.3 ± 1.3 degrees. However, when the subjects were bending to the left and right hand sides, the distance and angle errors were 4.2 ± 1.4 mm and 2.9 ± 1.8 degrees, respectively. The distance error increased when the measured distances increased. Also, the angle error increased when the measured angles increased and especially when the angles were closed to 90 degrees.

According to chapter 3, the acceptable errors in shoulder measurements on distance and angle were ± 5 mm and ± 5 degrees. Therefore, this system was able to measure the shoulder asymmetry of a subject. Also, the system should be able to measure the pelvis asymmetry, decompensation and waist asymmetry index because the accuracy of the system is within the acceptable errors.

8.5. A Comparison between a Commercial EM System to the Designed System

An experiment was carried out to compare the accuracy of the designed system to a commercial EM system, the Flock of Birds system that developed by Ascension Technology Corporation.

8.5.1. Procedures

Measurements using both systems were carried out on a wooden table with a grid map laid on top. A point on the grid map was chosen as an origin and used as a reference point. Measurements from the Flock of Birds system were carried out first. The transmitter of the Flock of Birds system was placed at the origin. The receiver of the Flock of Birds system was moved from 300 mm to 480mm with increments of 10 mm. At each of the positions six measurements were taken. Figure 8-6 shows the results of the average distance measurement with one standard deviation versus the actual distance from the Flock of Birds system. Measurements from the designed system were then carried out. The same procedures as before were done. Figure 8-7 shows the results of the average distance measurement with one standard deviation versus the actual distance.

8.5.2. Results and Discussion

From the measurements using the Flock of Birds and the designed system, the distance measurements at 300 and 480 mm are 300.1 ± 0.6 and 483.0 ± 1.05 mm and 300.6 ± 1.15 and 485.0 ± 2.05 mm, respectively. Although the commercial system has a higher accuracy, the designed system is able to detect the distance measurements from 300 to 480 mm and measurement errors within 5mm.

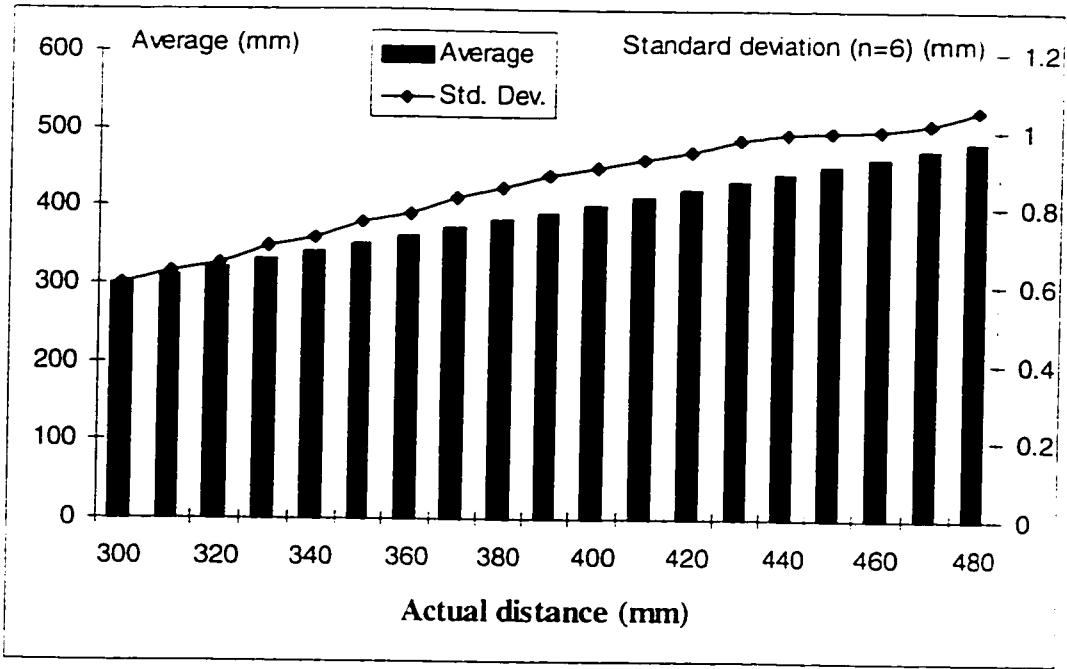


Figure 8-6. The average distance measurement with one standard deviation versus the actual distance from the Flock of Birds system

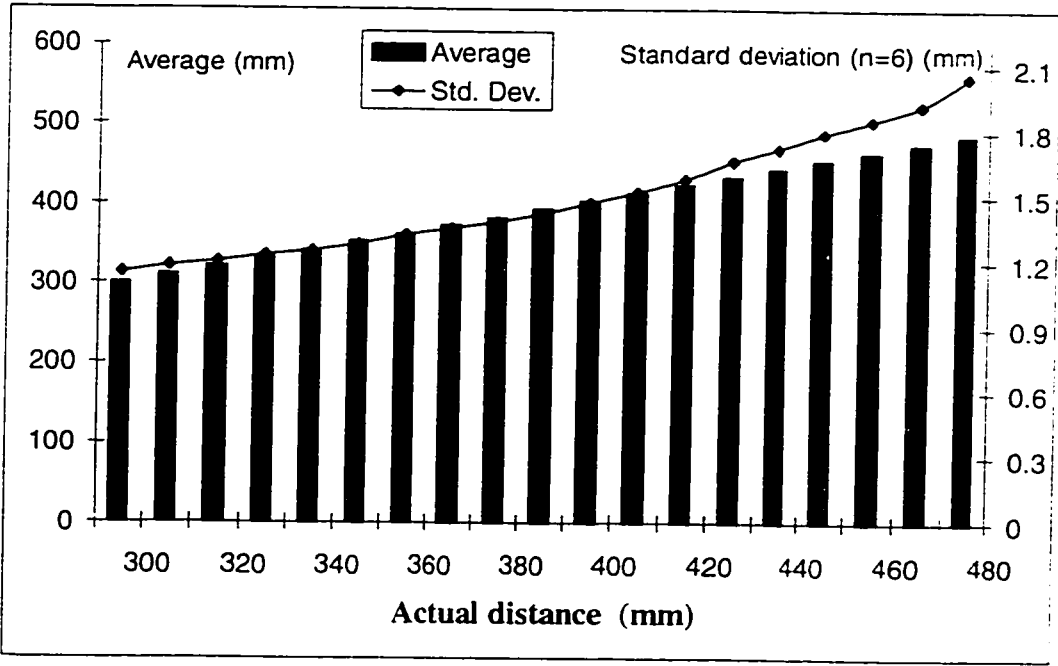


Figure 8-7. The average distance measurement with one standard deviation versus the actual distance from the designed system

8.6. Summary

Experimental tests and clinical trials were done to validate the system. Experimental tests provided results to test the accuracy of two-dimensional measurements, while the clinical trials tested the three-dimensional measurements. The range of distance error from the experimental tests was 0.07cm to 0.54cm in the range of 30 to 48cm, while the range of the angle error was from maximum 4 degrees to minimum 1.1 degrees in the range of 0 to 90 degrees. Also, from the clinical trials, the distance and angle errors are both in the same range as that from the experimental. A comparison between a commercial EM system to the designed system was carried out. Although, the commercial system had a higher accuracy, the accuracy of the designed system was within the acceptable error. Therefore, the system was able to detect the changes of the shoulder asymmetry.

9. CONCLUSIONS AND FUTURE DEVELOPMENT

9.1. Conclusions

The intent of this research was to develop a new method help scoliotic patients to correct their spinal deformities. This method requires a three-dimensional measurement system to measure the topographical features of a scoliotic trunk and provide feedback to patients during their daily activities. Trunk distortion and back shape studies were used to determine the features that contribute to the deformity. An objective method was shown that the topographical features could be reliably and repeatably measured. Electromagnetic theory was applied to develop an algorithm so that the three dimensional measurements could be determined automatically. The challenges in developing this low-power portable EM system have been reported in this thesis. Also, because of the innovative design of the system, a U.S. patent application has been submitted. This measurement system consists of a controller unit, one transmitter and two receivers (a maximum of eight receivers can be used simultaneously). The dimensions and the weight of the controller unit are 4 cm x 10 cm x 14 cm and 120 g, respectively. The average power consumption per day of the system is 400 mW (5 V x 80 mA). The dimensions and the weight of the transmitter and receivers are 4cm x 2cm x 2cm and 30g, respectively. The transmitter and receiver units are easily hidden under clothes. The system has been tested in both the laboratory and clinical environments. The results show that the accuracy of the distance and angle measurements are within 5mm and 5 degrees over the distance and angle ranges 30 to 48 cm and 0 to 90 degrees, respectively. The system is able to detect the postural changes of a subject. Furthermore, this system is

not limited to use in scoliosis studies but may be used for a variety of other portable three-dimensional measurement studies.

9.2. Recommendations for Future Work

The designed system was shown to be able to detect reliably postural changes of adolescent associated with idiopathic scoliosis. Further development of this system should combine a biofeedback approach to offer a new way to help adolescents to improve trunk asymmetry associated with mild scoliosis.

Also, more clinical trials should be arranged so that

- (1) the range of acceptable and unacceptable postures can be defined,
- (2) a feedback method can be explored,
- (3) a more acceptable sample interval can be determined,
- (4) more suggestions and feedback from patients can be incorporated, and
- (5) the feedback responses from subjects can be determined.

In addition, the system can be enhanced with improvements to the hardware that reduce the size, the weight, the computation time and that improve the accuracy and the resolution of the system. These hardware enhancements could include:

- (1) Replacement of the existing MC68HC16Z1 microcontroller by a low power 32-bit digital signal processor. For example, the Motorola DSP96000-family is the low power DSP chip family which can be programmed into a low power mode in which the current consumption is less than 1 mA. Most of the DSP chips have higher clock speeds so that the computation time can be shorter. Also, the built-in EEPROM and the Fast Fourier Transform (FFT) function of the DSP chips can

eliminate the existing ROMs and the bandpass filter so that the size of the system can be reduced. The 32-bit signal processor enhances the resolution of the whole system so that more accurate results can be obtained, especially when the angle is close to 0 or 90 degrees. The low power and high resolution A/D converter can increase the resolution of the system.

- (2) Fabrication of the transmitting circuitry as an individual IC so that the reliability can be increased and the noise generated from the circuitry can be decreased.
- (3) Fabrication of the receiver circuitry such as the regulator, the pre-amplifier and the multiplexer as an individual IC so that the reliability can be increased and the noise generated from the circuitry can be decreased.

REFERENCES

- [1] L. A. Goldstein, and T. R. Waugh, "Classification and terminology of scoliosis," *Clin. Orth.*, vol. 93, pp. 10-22, 1973.
- [2] H. A. King, and J. H. Moe, "The selection of fusion levels in thoracic idiopathic scoliosis," *J. Bone Joint Surg.*, vol. 65, pp. 1302-1313, 1983.
- [3] J. R. Cobb, "Outline for the study of scoliosis," *Am. Acad Orthop.*, vol 5, pp. 261-275, 1948.
- [4] C. L. Nash and J. H. Moe, "A Study of Vertebral Rotation," *J. Bone Joint Surg.*, vol. 61A, pp. 371-380, 1979.
- [5] I. A. F. Stokes, L. C. Bigalow, and M. S. Moreland, "Measurement of Axial Rotation of vertebrae in Scoliosis," *Spine*, vol. 11, no. 3, pp. 213-218, 1985.
- [6] B. Derup, "Principles of Measurement of Vertebral Rotation from Frontal Projections of the Pedicles," *J. Biomechanics*, vol. 17, no. 12, pp. 923-935, 1984.
- [7] S. L. Weinstein, "The Pediatric Spine: Principles and Practice," Raven Press Ltd., New York, 1994.
- [8] S. Willner and A. Uden, "A prospective prevalence study of scoliosis in southern Sweden," *Acta Orthop. Scand*, vol. 52, pp. 233-237, 1982.
- [9] J. E. Lonstein, "Natural History and School Screening for Scoliosis," *Orthopedic Clinics of North America*, vol. 19, no. 2, pp. 227-237, 1988.
- [10] W. W. Greulich and S. I. Pyle, "Radiographic Atlas of skeletal Development of the Hand and Wrist," Stanford University Press, California, 2nd edition, 1959.
- [11] A. L. Zaosis and J. I. P. James, "The iliac apophysis and the evolution of curves in scoliosis," *J. Bone Joint Surg.*, vol. 40B, pp. 442-453, 1958.

- [12] M. Anderson, S. Hwan, and W. T. Green, "Growth of the normal trunk in boys and girls during the second decade of life," *J. Bone Joint Surg.* vol. 47A, p. 1554, 1965.
- [13] J. E. Lonstein and J.M. Carlson, "The prediction of curve progression in untreated idiopathic scoliosis during growth," *J. Bone Joint Surg.*, vol. 66A, pp. 1067-1071, 1984.
- [14] A. Nachemson, J. E. Lonstein, and S. L. Weinstein, "Report of the SRS Prevalence and Natural History Committee 1982," Presented at SRS meeting Denver, 1982.
- [15] W. P. Bunnell, "A study of the natural history of idiopathic scoliosis before skeletal maturity," *Spine*, no. 11, p.773, 1986.
- [16] G. C. Robin, "The Aetiology of Idiopathic Scoliosis," Freund Publishing House Ltd., 1990.
- [17] S. Willner, "Growth in height of children with scoliosis," *Acta Orth. Scand.*, vol. 45, pp. 854-866, 1974.
- [18] S. Willner, "Study of growth in girls with adolescent idiopathic structural scoliosis," *Clin. Orth.*, vol. 101, pp. 129-135, 1974.
- [19] S. Willner, "A study of height, weight and menarche in girls with idiopathic structural scoliosis," *Acta Orth. Scand.*, vol. 46, pp. 71-83, 1975.
- [20] S. Willner, "The proportion of legs to trunk in girls with idiopathic structural scoliosis," *Acta Orth. Scand.*, vol. 46, pp. 84-89, 1975.
- [21] J. C. Risser and A. B. Ferguson, "Scoliosis - its prognosis," *J. Bone Joint Surg.*, vol. 18, pp. 667-670, 1936.
- [22] S. Misol, I. V. Ponseti, N. Samaan and J. T. Bradbury, "Growth hormone blood level in patients with idiopathic Scoliosis," *Clin. Orth.*, vol. 81, pp. 122-125, 1971.

- [23] S. Willner, K. O. Nilsson, K. Kastrup and C. G. Bergstrand, "Growth hormone and somatomedin-A in girls with idiopathic scoliosis," *Acta Paed. Scand.*, vol. 65, pp. 547-552, 1976.
- [24] L. B. Skogland and J. A. Miller, "The incidence of scoliosis in North Norway. A preliminary report," *Acta Orth. Scand.*, vol. 49, p. 635, 1978.
- [25] L. B. Skogland, J. A. Miller, A. Skottner and L. Fryklund, "Serum somatomedins and non-dialysable urinary hydroxyproline in girls with idiopathic scoliosis." *Acta Orth. Scand.*, vol. 52, pp. 307-313, 1981.
- [26] R. D. Pool, R. M. Smith, D. Sharpes and R. A. Dickson, "Bone drift and structural scoliosis," *Orth. Trans.*, no. 11, pp. 109-110, 1987.
- [27] K. P. Meade, W. H. Bunch, R. Vandery, A. G. Patwardhan and G. W. Knight "Progression of unsupported curves in adolescent idiopathic scoliosis. *Spine*," no. 12, pp. 520-526, 1987.
- [28] E. Somerville, "Rotational lordosis in the development of the single curve." *J. Bone Joint Surg.*, vol. 34B, pp. 412-427, 1952.
- [29] R. Roaf, "Vertebral growth and mechanical control," *J. Bone Joint Surg.*, vol. 42B, pp. 40-59, 1960.
- [30] F. Knutsson, "Vertebral genesis of idiopathic scoliosis in children," *Acta Radiol.*, vol. 4, pp. 395-402, 1966.
- [31] W. F. Enneking and P. Harrington, "Pathological changes in scoliosis," *J. Bone Joint Surg.*, vol. 51A, pp. 165-184, 1969.
- [32] G. A. Olsen and J. H. Allen, "The lateral stability of the spine," *Clin. Orth.*, vol. 65, pp. 143-156, 1969.

- [33] J. A. Sevastikoglou, S. Aaro, T. S. Lindholm and M. Dahlborn, "Experimental scoliosis in growing rabbits by operations on the rib cage," *Clin. Orth. and Related Research*, vol. 136, pp. 282-286, 1978.
- [34] H. Normelli, J. Sevastik and J. Akrivos, "The length and ash weight of the ribs of normal and scoliotic persons," *Spine*, no. 10, pp. 590-592, 1985.
- [35] I. A. F. Stokes, J. Dansereau and M. S. Moreland, "Rib cage asymmetry in scoliosis," *J. Orthop. Res.*, vol. 7, pp. 599-606, 1989.
- [36] J. Sevastik, M. Agadir and B. Sevastik, "Effects of rib elongation on the spine. I. Distortion of the vertebral alignment in the rabbit," *Spine*, vol. 15, pp. 822-825, 1990.
- [37] R. Roaf, "Spinal Deformities". London: Pitman Medical, 1977.
- [38] J. R. Schwartzmann and M. Miles, "Experimental production of scoliosis in rats and mice," *J. Bone Joint Surg.*, vol. 27, pp. 59-69, 1945.
- [39] R. M. Smith and R. A. Dickson, "Progressive experimental scoliosis in the New Zealand white rabbit," *J. Bone Joint Surg.*, vol. 68B, p.682, 1986.
- [40] R. M. Smith and R. A. Dickson, "Experimental structural scoliosis," *J. Bone Joint Surg.*, vol. 69B, pp. 576-581, 1987.
- [41] H. V. F. Riddle and R. Roaf, "Muscle imbalance in the causation of scoliosis," *Lancet I*, pp. 1245-1247, 1955.
- [42] H. Rossler, "Biomechanics of scoliosis," *J. Bone Joint Surg.*, vol. 50B, p.880, 1968.
- [43] V. M. Badger, "Correlation studies on muscle in scoliosis: histochemistry, EMG, EM, and quantive enzyme estimation," *J. Bone Joint Surg.*, vol. 51A, p.204, 1969.

- [44] V. Gueth and F. Abbink. "Electromyogram and kinesiologic investigation: a comparison of congenital and idiopathic scoliosis," *Ztschr. Orth. Grenzgeb.*, vol. 118, pp. 165-172, 1980.
- [45] M. Reyber, A. Schultz., T. McNell and D. Spencer, "Trunk muscle myoelectric activities in idiopathic scoliosis," *Spine*, vol. 8, pp. 447-456, 1983.
- [46] R. Roaf, "The role of the multifidus muscle and its practical significance," *J. Bone Joint Surg.*, vol. 58B, pp. 374-375, 1976.
- [47] W. Gonyea, D. Wenger, B. Moseley, M. Hollman and C. Moore-Woodhead. "Assessment of primary versus stress-related changes in scoliosis muscles - an exercise physiologist's interpretation," *Orth. Trans.*, no. 8, p.143, 1984.
- [48] T. Sahlstrand, B. Petrusson and R. Ortengren., "Vestibulospinal reflex activity in patients with adolescent idiopathic scoliosis," *Acta Orth. Scand.*, vol. 50, pp. 275-281, 1979.
- [49] R. L. Barrack, T. S. Whitecloud, S. W. Burke, S. D. COOK and A. F. Harding, "Proprioception in idiopathic scoliosis," *Orth. Trans.*, no. 8, p.142, 1984.
- [50] M. Gregoric, F. Pecak, J. V. Trontelj, M. R. Dimitrijevic, "Posture control in scoliosis. A statokinesimetric study in patients with scoliosis due to neuromuscular disorders and in patients with idiopathic scoliosis." *Acta Orth. Scand.*, vol. 52, pp.59-63, 1981.
- [51] M. Yekutieli, G. C. Robin and R. Yarom, "Proprioceptive function in children with adolescent idiopathic scoliosis," *Spine*, vol. 6, pp. 560-566, 1981.
- [52] W. Keessen, "Proprioceptive Accuracy in Idiopathic Scoliosis," *Spine*, vol. 17, pp. 149-155, 1992.

- [53] T. Sahlstrand, B. Petrusson and R. Ortengren, "Vestibulospinal reflex activity in patients with adolescent idiopathic scoliosis," *Acta Orth. Scand.*, vol. 50, pp. 275-281, 1979.
- [54] M. P. Wyatt and R. L. Barrack. "Posterior column function in idiopathic scoliosis." Presented at the 19th Annual Meeting of the Scoliosis Research Society, Orlando, Florida, 1984.
- [55] H. Yamamoto, "A postural dysequilibrium as an aetiological factor in idiopathic scoliosis," *Orth. Trans.*, no. 7, p.5, 1983.
- [56] J. Dubousset, P. Queneau and M. J. Thillard, "Experimental scoliosis induced by pineal and diencephalic lesions in young chickens: its relation with clinical findings in idiopathic scoliosis," *Orth. Trans.*, no. 7, p.7, 1983.
- [57] A. Nordwall, "Studies in idiopathic scoliosis." *Acta Orth. Scand.*, no.150, pp. 100-103, 1973.
- [58] D. S. Bradford, T. R. Oegema, D. M. Brown, "Studies on skin fibroblasts of patients with idiopathic scoliosis," *Clin. Orthop.* no. 126, p.111, 1977.
- [59] V. A. Pedrini, I. V. Ponseti and S. C. Dohrman, "Glycosaminoglycans of intervertebral discs in idiopathic scoliosis," *J. Lab. Clin. Med.*, vol. 82, pp. 938-950, 1973.
- [60] T. K. F. Taylon, P. Ghosh, G. R. Bushell and J. M. Sutherland, "Disc metabolism in scoliosis", ed. Zorab PA, pp. 231-246. London: Academic Press, 1977.
- [61] M. H. O. Francis, M. C. Sanderson and R. Smith, "Skin collagen in idiopathic adolescent scoliosis and Marfan syndrome," *Clin. Sci. Mol. Med.*, vol. 51, pp. 467-474, 1976.

- [62] G. R. Bushell, P. Ghose, T. K. F. Taylon and J. M. Sutherland, "The collagen of the intervertebral disc in adolescent idiopathic scoliosis," *J. Bone Joint Surg.*, vol. 61B, pp. 501-508, 1979.
- [63] G. Venn, M. H. Mehta and R. M. Mason, "Solubility of spinal ligament collagen in idiopathic and secondary scoliosis," *Clin. Orth.*, vol. 177, pp. 294-301, 1983.
- [64] T. R. Oegema, D. S. Bradford, K. M. Cooper and R. E. Hunter, "Comparsion of biochemistry of proteoglycans isolated from normal, idiopathic scoliosis and cerebral palsy spines," *Spine*, vol. 8, pp. 378-387, 1983.
- [65] F. Nitsche and P. Armknecht, "Orthopaedische Leide bei Zwilligen," *Ztsch. Orth.*, vol. 58, pp. 528-537, 1933.
- [66] R. L. Fisher and F.V. DeGorge, "A twin study of idiopathic scoliosis," *Clin. Orth.*, vol. 55, pp. 117-126, 1967.
- [67] J. James, "Scoliosis," Edinburgh: Livingstone, 2nd edition 1967.
- [68] F. V. DeGeorge and R. L. Fisher, "Idiopathic scoliosis: genetic and environmental aspects," *J. Med. Genet.*, vol. 4, pp. 251-257, 1967.
- [69] G. C. Robin and T. Cohen, "Familial scoliosis: a clinical report," *J. Bone Joint Surg.*, vol. 57B, pp. 146-147, 1975.
- [70] R. Wynne-Davies, "Familial (idiopathic) scoliosis: a family study," *J. Bone Joint Surg.*, vol. 50B, pp. 24-30, 1968.
- [71] E. J. Riseborough and R. Wynne-Davies, "A genetic Survey of idiopathic scoliosi in Boston, Massachusetts," *J. Bone Joint Surg.*, vol. 55A, pp. 974-982, 1973.

- [72] T. P. Andriosechi, A. B. Schultz, T. B. Belytschko and R. L. Dewald, "Milwaukee Brace Correction of Idiopathic Scoliosis," *J. Bone Joint Surg.*, vol. 58A, pp. 806-815, 1976.
- [73] H.G. Watts, J. E. Hall and W. M. Stanish, "The Boston Brace System for the Treatment of Low Thoracic and Lumbar Scoliosis by the Use of a Girdle Without Superstructure," *Clin. Orth. and Related Research*, vol. 126, pp. 87-92, 1977.
- [74] A. P. Chase, D. L. Bader and G. R. Houghton, "The Biomechanical Effectiveness of the Boston Brace in the Management of Adolescent Idiopathic Scoliosis," *Spine*, vol. 14, pp. 636-639, 1989.
- [75] C. T. Price, D.S. Scott, F.E. Reed and M.F. Riddick, "Nighttime Bracing for Adolescent Idiopathic Scoliosis with the Charleston Bending Brace," *Spine*, vol. 15, no. 12, pp. 1294-1299, 1990.
- [76] R. H. Houghton, A. McInerney and T. Tew, "Monitoring True Brace Compliance." *Proceedings of the 21st. Meeting of the Scoliosis Research Society*, Hamilton, Bermuda, September, 1986.
- [77] M. Ylikoski, J. Peltonen and M. Poussa, "Biological Factors and Predictability of Bracing in Adolescent Idiopathic Scoliosis," *Journal of Pediatric Orthopaedics*, no. 9, pp. 680-683, 1989.
- [78] J. Dansereau, H. Labelle, C. Bellefleur and B. Poitras, "Boston Brace Treatment: 3-D Immediate effect on the Thoracic Scoliotic Spine," *International Symposium on 3-D Scoliotic Deformities*, ed J.Dansereau, pp. 312-316, Montreal, 1992.

- [79] C. E. Aubin, J. Dansereau, J. A. de Guise, H. Labelle, "Rib Cage-Spine Coupling Patterns Involved in Brace Treatment of Adolescent Idiopathic Scoliosis." *Spine*, vol. 22, no. 6, pp. 629-635, 1997.
- [80] C. S. Lehnert, "Introduction to the three-dimensional scoliosis treatment according to Schroth", *Physiotherapy*, vol. 78 no. 11 pp. 810-815, 1992.
- [81] H. R. Weiss, "The Progression of Idiopathic Scoliosis under the Influence of a Physiotherapy rehabilitation Programme", *Physiotherapy*, vol. 78, no. 11. pp. 815-821, 1992.
- [82] B. Dworkin, N. E. Miller, S. Dworkin, N. Birbaumer, M. L. Brines, S. Joans, E. P. Schwentker and J. J. Graham, "Behavioral method for the treatment of Idiopathic Scoliosis", *Proc. Natl. Acad. Sci. USA*, Vol. 82, pp. 2493-2497, 1985.
- [83] M. El-Sayyad, T. A. Conine, "Effect of exercise, bracing and electrical surface stimulation on idiopathic scoliosis: preliminary study", *International Journal of Rehab. Research*, Vol. 17, pp. 70-74, 1994.
- [84] F. G. Allan, "Scoliosis: Operative correction of fixed curves," *J. Bone Joint Surg.*, vol. 37B, p.92, 1955.
- [85] P. R. Harrington, "Treatment of scoliosis: correction and internal fixation by spine instrumentation," *J. Bone Joint Surg.*, vol. 44A, pp. 519-610, 1962.
- [86] E. R. Luque, "The anatomical basis and development of segmental spinal instrumentation," *Spine*, vol. 7, pp. 256-259, 1982a.
- [87] E. R. Luque, "Segmental spinal instrumentation for correction of scoliosis," *Clin. Orth.*, vol. 163, pp. 192-198, 1982b.

- [88] A. F. Dwyer, N. C. Newton and A. A. Sherwood, "An anterior approach to scoliosis," *Clin. Orth.*, vol. 62, pp. 192-202, 1969.
- [89] C. J. Harvey, R. R. Betz, D. H. Clements, G. K. Huss and M. Clancy M, "Are there Indications for partial Rib Resection in patients with Adolescent Idiopathic Scoliosis Treated with Cotrel-Dubousset Instrumentation?" *Spine*, no. 18, pp. 1593-1598, 1993.
- [90] Scoliosis Association Inc., P.O. 81705, Boca Raton, Florida 33481-1705, 1993.
- [91] J. K. Mahood, M. J. Moreau, D. L. Hill, and V. J. Raso, "Perceptions of Cosmetic Deformity in Scoliosis," *Proceedings of the 2nd. International Symposium on Three Dimensional Scoliotic Deformities*, Pescara, September, pp. 239-242, 1994.
- [92] H. Hsiao and W. M. Keyserling, "A three-dimensional ultrasonic system for posture measurement," *Ergonomics*, vol. 33, no. 9, pp. 1089-1114, 1990.
- [93] H. Nagano, "Inclination sensor," *Mechanical Automation*, vol. 15, no. 6, p. 127, 1983.
- [94] H. Kato, M. Kojima, M. Gattoh, Y. Okumura and S. Morinaga, "Photoelectric inclination sensor and its application to the measurement of the shades of 3-D Objects," *IEEE Trans. On Instrumentation and measurement*, vol. 40, no. 6, pp. 1021-1026, 1991.
- [95] S. Tanaka, K. Yamakoshi and P. Rolfe, "New portable instrument for long-term ambulatory monitoring of posture change using miniature electromagnetic inclinometers," *Med. & Biol. Eng. & comput.*, vol. 32, pp. 357-360, 1994.

- [96] J. D. Harris, A. R. Turner-Smith, "Clinical Back Shape Analysis with an Anatomically Defined Datum". *Moire Fringe Topography*, ed. by Dreup. Forbin & Hierholzer, New York, 1983.
- [97] T. N. Theologis, R. J. Jeffereson, A. H. Simpson, A.R. Turner-Smith. J. C. Fairbank, "Quantifying the Cosmetic Defect of Adolescent Idiopathic Scoliosis". *Spine*, vol. 18, pp. 909-912, 1993.
- [98] D. L. Hill, J. K. Mahood, M. J. Moreau, V. J. Raso, N. G. Durdle, "The Scoring of Trunk Distortion in Scoliosis", *Studies in Health Technology and Informatics*, vol. 37, pp. 289-292, 1996.
- [99] H. P. Kalmus, "A new guiding and tracking system", *IRE Trans. Aerosp. Navig. Electron*, vol. 9, pp. 7-10. 1962.
- [100] F. H. Raab, E. B. Blood, T. O. Steiner, H. R. Jones, "Magnetic Position and Orientation Tracking System," *IEEE Trans. Aerosp. Electron Systems*, vol. AES-15, no. 5, pp. 709-718, 1979.
- [101] K. N. An, M. C. Jacobsen, L. J. Berglund & E. Y. S. Chao, "Application of a Magnetic Tracking Device to Kinesiologic Studies," *J. Biomechanics.*, vol. 21, No. 7, pp. 613-620, 1988.
- [102] M. J. Pearcy, R. J. Hindle, "New method for the non-invasive three-dimensional measurement of human back movement," *Clinical Biomechanical*, vol. 4, pp.73-79, 1989.
- [103] S. Levine, D. Silage, D. Henson, J. Wang, J. Krieg, J. Lamanca, S. Levy, "Use of a triaxial magnetometer for respiratory measurements," *Special Communications*, pp. 2311-2321, 1990.

- [104] S. J. Bresina, M. W. Vannier, S. E. Logan, P.M. Weeks, "Three-dimensional Wrist Imaging: Evaluation of Functional and Pathologic Anatomy by computer," *Computers in Plastic Surgery*, vol. 13, No. 3, pp.389-405, 1986.
- [105] S. Iskra, I. P. Macfarlane, "H-Field Sensor Measurement Errors in the Near-Field of a Magnetic Dipole Source," *IEEE Transactions on Electromagnetic compatibility*, Vol. 31, No. 3, pp.306-311, 1989.
- [106] D. K. Cheng, "Field and Wave Electromagnetics," 2nd edition. Addison-Wesley Publishing Company Inc. 1989.
- [107] R. G. Olsen and A. J. Farstad, "Electromagnetic direction finding experiments for location of trapped miners," *IEEE Trans. Geosci. Electron.*, vol. GE-11, pp. 178-185, 1973.
- [108] J. H. Murphy and H.E. Parkinson, "Underground mine communications." *Proc. IEEE*, vol. 66 pp. 26-50, 1978.
- [109] V. J. Raso, E. Lou, D. L. Hill, J. K. Mahood, M. J. Moreau, and N. G. Durdle, "Trunk Distortion in Adolescent Idiopathic Scoliosis", *Journal of Pediatric Orthopaedics*. (IN PRESS), 1998.
- [110] E. Lou, D. L. Hill, V. J. Raso, N. G. Durdle and J. K. Mahood, "An Objective Measurement of Trunk Deformity", the Transactions of the 2nd combined meeting of the Orthopaedic Research Societies of U.S.A., Japan. Canada and Europe, p.242, 1995.
- [111] E. Lou, N. G. Durdle, V. J. Raso and D. L. Hill, "Measurement of Magnetic Field in the Near-Field Region and Self-inductance in Free Space Due to a multiturn square

loop," *IEE Proceedings – Science Measurement and Technology*, vol. 144, no.6, pp. 252-256, 1997.

APPENDIX A

A.1. CPU16

The CPU16 is a true 16-bit device, which supports 8-bit (byte), 16-bit (word) and 32-bit (long-word) load and store operations, as well as 16- and 32-bit signed fractional operations. The CPU16 uses 16 data lines and 20 address lines to support 1 Mbyte program space and 1 Mbyte data space. Twenty-bit addressing (ADDR[19:0]) and transparent bank switching are used to implement extended memory. Therefore, the accessible addresses are \$000000-\$07FFFF and \$F80000-\$FFFFFF. The internal addressing map of the MC68HC16Z1 is shown in Figure A-1 in which the internal 1K RAM is positioned from \$FF0000 to \$FF03FF. Furthermore, the CPU16 includes instructions and hardware to implement control-orientated digital signal processing functions with a minimum of interfacing. A multiply and accumulate unit provides the capability to multiply signed 16-bit fractional numbers and store the resulting 32-bit fixed point product in a 36-bit accumulator.

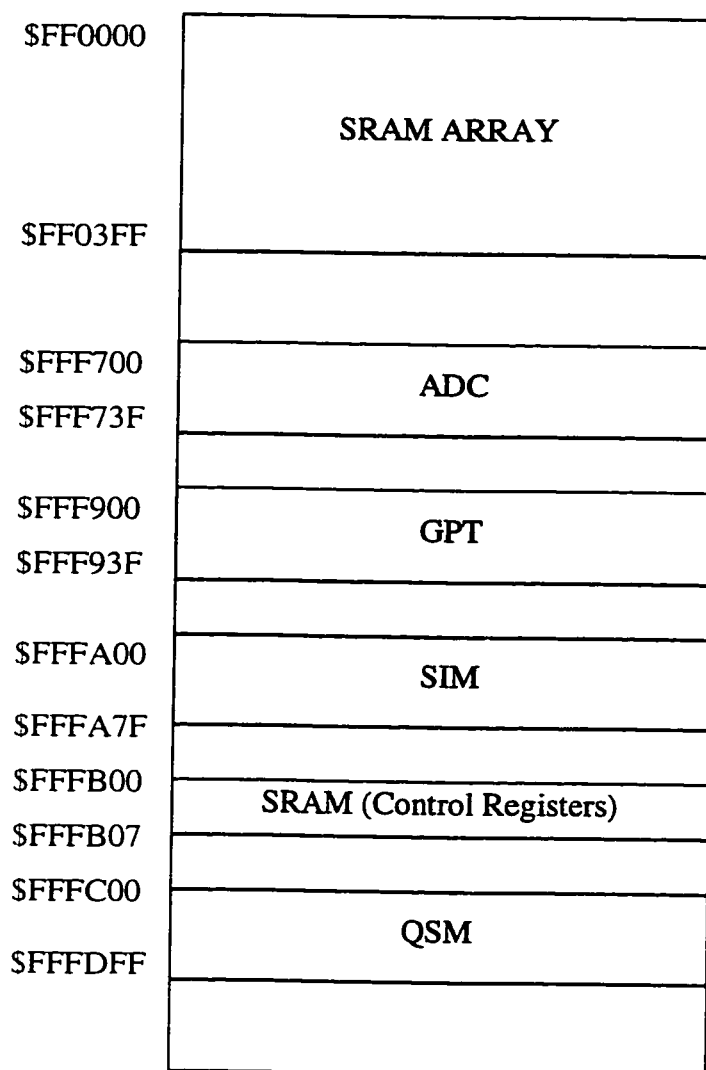


Figure A-1. The internal addressing map of the MC68HC16Z1.

A.2. System Integration Module (SIM)

The SIM consists of five functional blocks (Figure A-2): 1) system configuration and protection, 2) clock synthesizer, 3) chip selects, 4) external bus interface and 5) factory test, which control system startup, initialization, configuration, and external bus with a minimum external devices.

The system configuration block controls the system startup, provides configuration control for the entire microcontroller, and performs interrupt arbitration, bus monitoring and system test functions. The protection block provides the system protection that includes a bus monitor, a HALT monitor, a spurious interrupt monitor, a software watchdog timer, and a periodic interrupt timer.

The clock synthesizer generates the system clock by using either an external frequency source or an external clock signal. The system clock provides timing signals for the IMB modules and for an external peripheral bus, and which can be changed by software.

Twelve chip select lines can be used to provide fast access (two cycle only) to external memory or peripherals without requiring any external circuitry. The maximum block size for an external peripheral is 512-kbyte.

The external bus interface transfers information between the internal MCU bus and external devices when the MC68HC16Z1 is operating in expanded modes. The external bus has 16 data lines (DATA[15:0]) and 24 address lines (ADDR[23:0]). However, the logic state of the address lines ADDR[23:20] is the same as that of ADDR[19], that means the sign extension applies on ADDR[23:20]. Only twenty addresses lines ADDR[19:0] can be assessed.

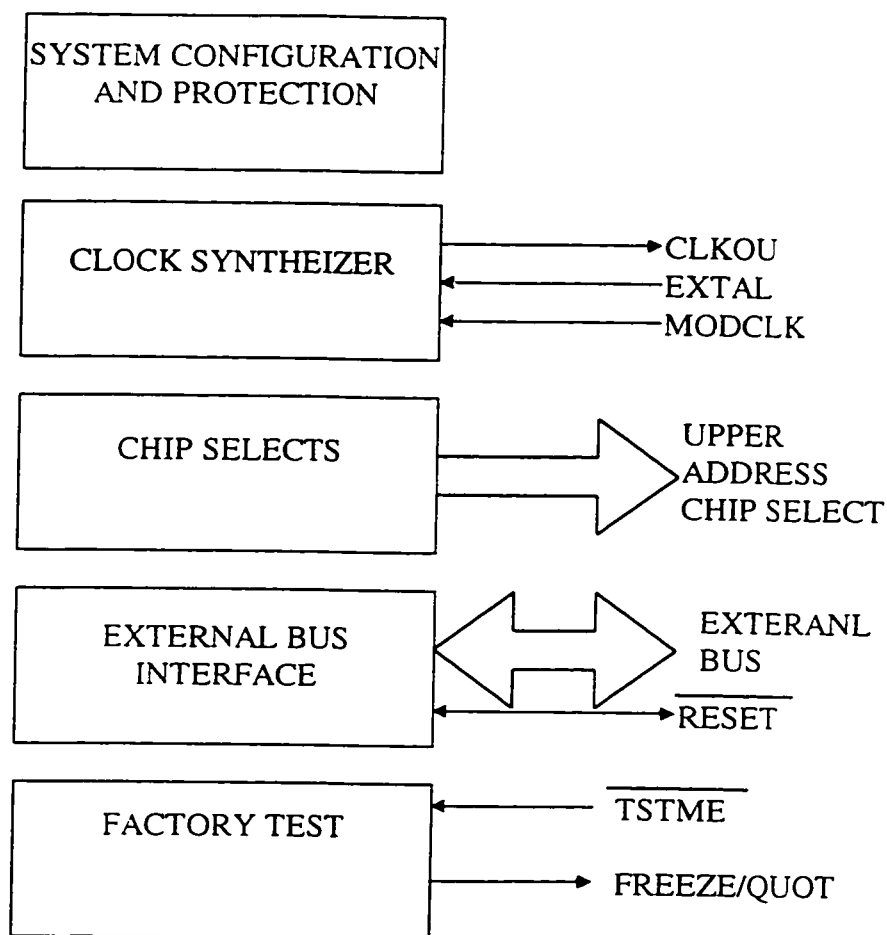


Figure A-2. The block diagram of SIM module.

A.3. Analog-to-Digital Converter (ADC) Module

The ADC is an unipolar, successive-approximation converter with eight modes of operation. Figure A-3 shows the block diagram of the ADC. Its resolution can be selectable either 8 or 10-bit. Its accuracy is ± 1 count (1 LSB) in 8-bit mode and ± 2.5 counts (2.5 LSB) in 10-bit mode. With the maximum clock frequency (16.78 MHz) of the system, the ADC can perform an 8-bit single-conversion in 8 microseconds while a 10-bit single-conversion requires 9 microseconds. The input pins of the ADC are shared

with Port A so that the user can program those pins as either analog inputs for the ADC or digital inputs for the Port A. In this application, a 10-bit ADC was configured.

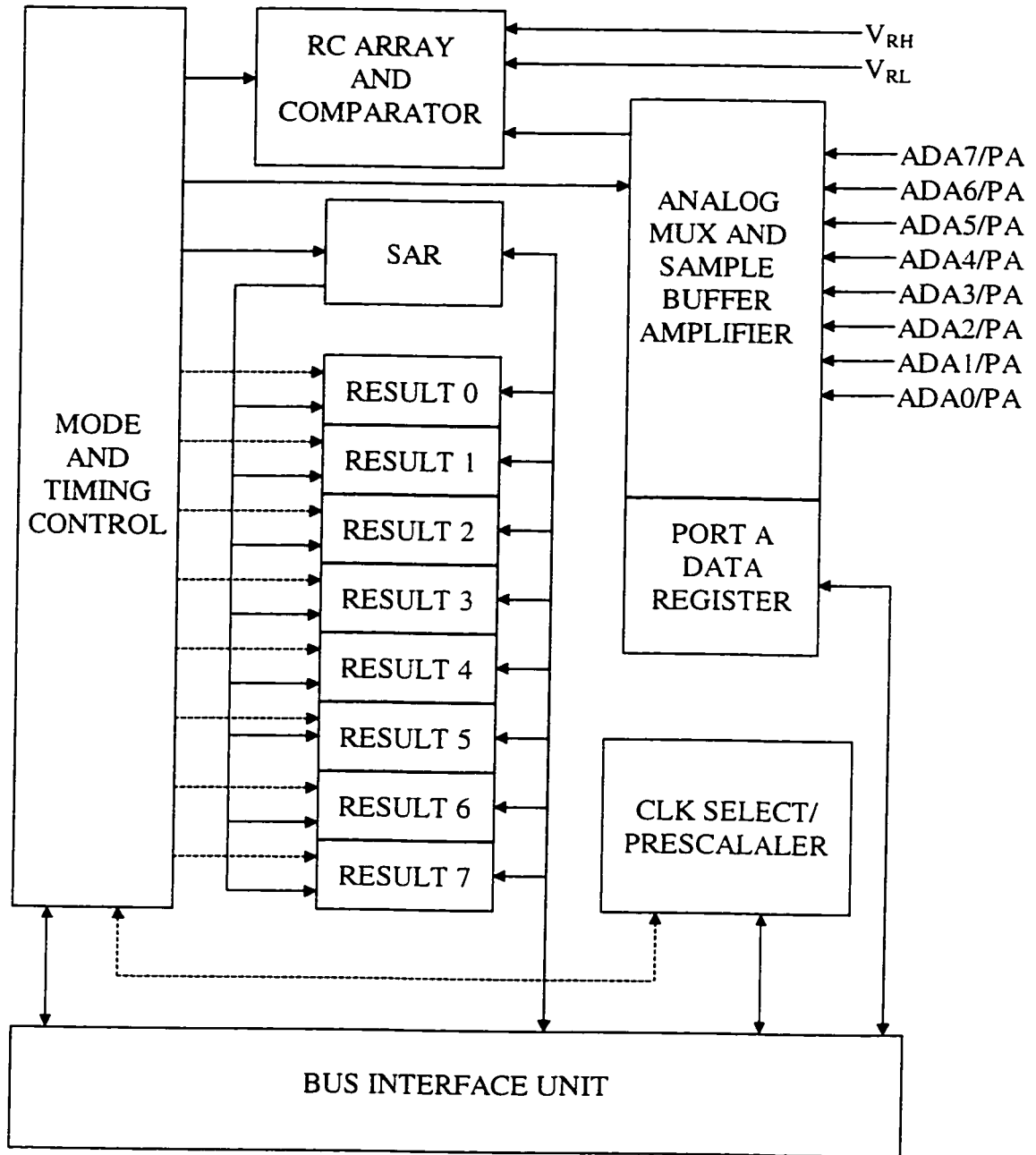


Figure A-3. The block diagram of ADC module.

A.4. Queued Serial Module (QSM)

The QSM contains two serial interfaces : 1) the queued serial peripheral interface (QSPI) and 2) the serial communication interface (SCI). The block diagram of this module is shown in Figure A-4. The QSPI provides easy peripheral expansion or interprocessor communication via a full-duplex, synchronous, three-line bus: data in, data out, and a serial clock. A programmable RTC communicates with the microcontroller through this serial interface. The SCI provides a standard non-return to zero mark/space format. It operates either in full-duplex or half-duplex mode and communicates with a PC so that data can upload from or download to a host computer.

A.5. General Purpose Timer (GPT) Module

The GPT is a simple and a flexible 12-channel timer module. Figure A-5 shows the block diagram of the GPT module. It consists of two independent submodules: the input capture/output compare unit (8 bidirectional I/O, and 2 input pins: PAI and PCLK), and the pulse-width modulator (2 output pins: PWMA and PWMB). The input capture shares the same pins with the output compare so that those pins are bidirectional. In addition, those pins can be configured as an 8-bit parallel port (Port D). Each pin is configured to control the selection of transmitter or receiver channels. Table A-1 shows the configuration of each pin. The pulse-width modulator has two output pins, and each output pin can output a periodic waveform that is under software control. The pulse-width modulation A has been connected to a buzzer which uses to provide an audio feedback to patients.

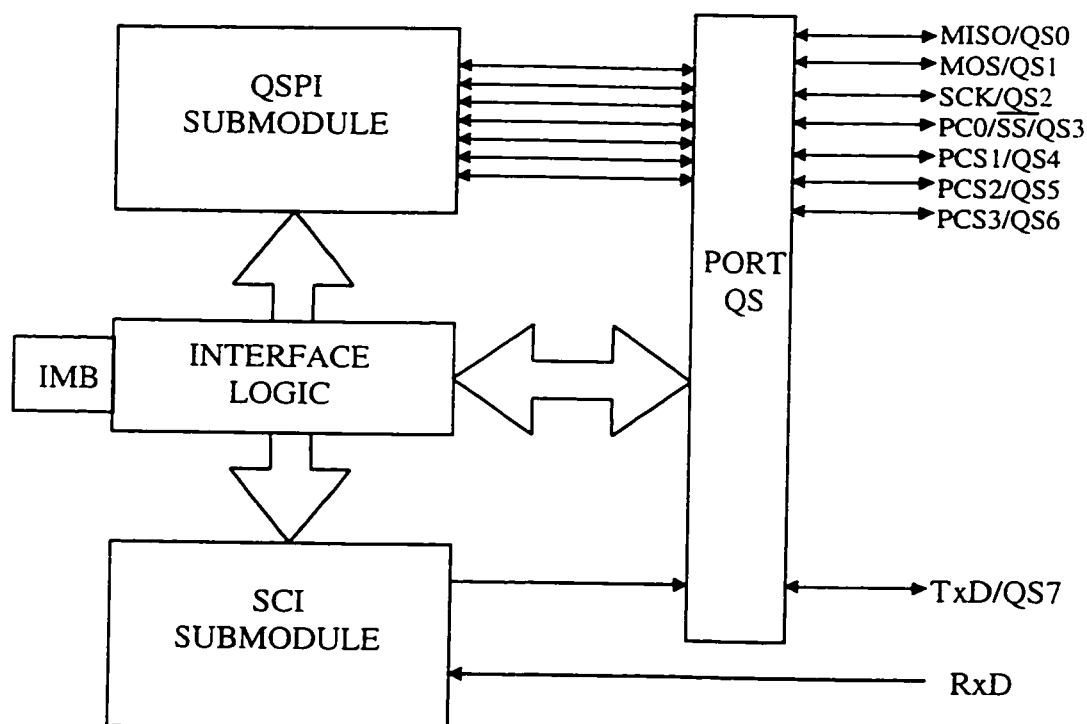


Figure A-4. The block diagram of QSM module.

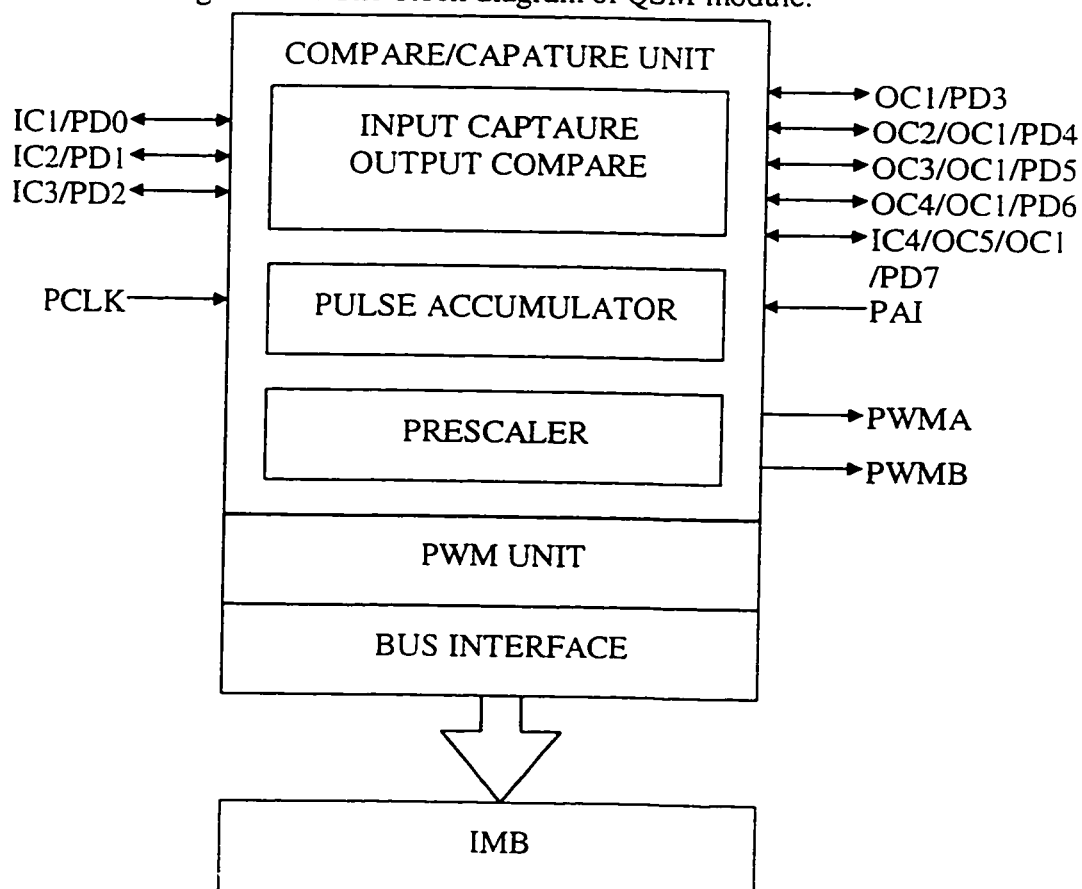


Figure A-5. The block diagram of GPT module.

Table A-1. The configuration of PD0-PD7

PD0	Logic control of the enable pin for +5V regulator, 0 = ON, 1 = OFF
PD1	Logic control of the enable pin for -5V regulator, 0 = ON, 1 = OFF
PD2	Logic for selecting channel X or Y or Z on receiver
PD3	Logic for selecting channel X or Y or Z on receiver
PD4	+5V & -5V power for Rx.1, 0 = OFF 1 = ON
PD5	+5V & -5V power for Rx.2, 0 = OFF 1 = ON
PD6	Logic control of the enable pin for the RS232, 0 = OFF, 1 = ON
PD7	Input capture pin for the Tx. to detect the synchronize signal

A.6. Standby Ram (SRAM) Module

This module contains a 1Kbyte array of fast access static RAM and usually uses for system stacks and variable storage. The RAM can be mapped to any 1 Kbyte boundary in the address map in condition that does not overlap the module control registers.

APPENDIX B

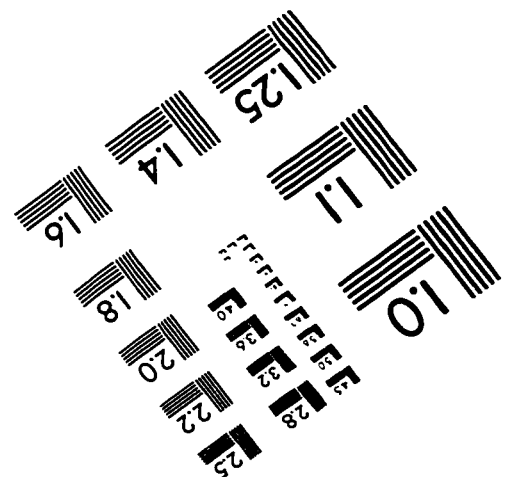
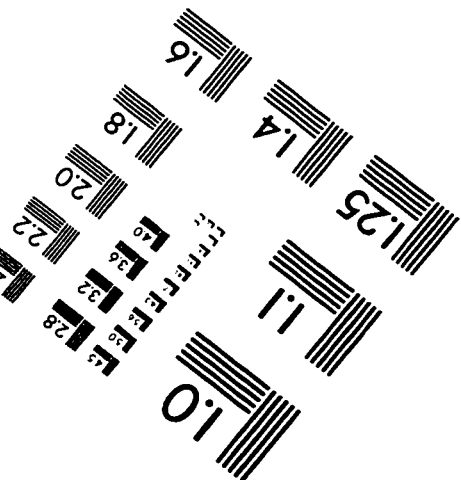
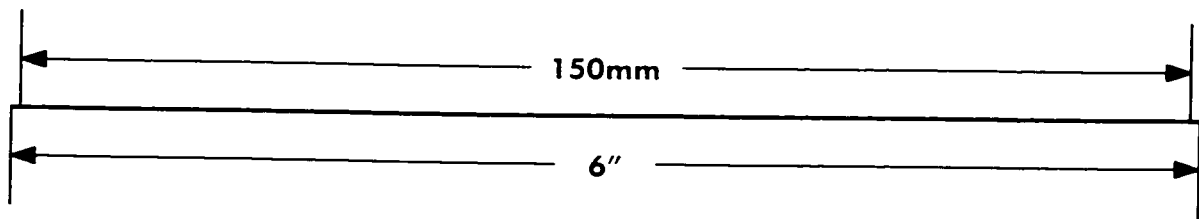
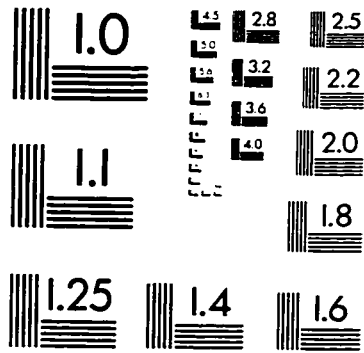
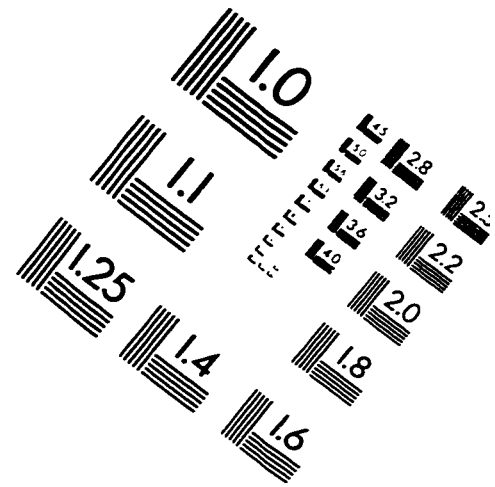
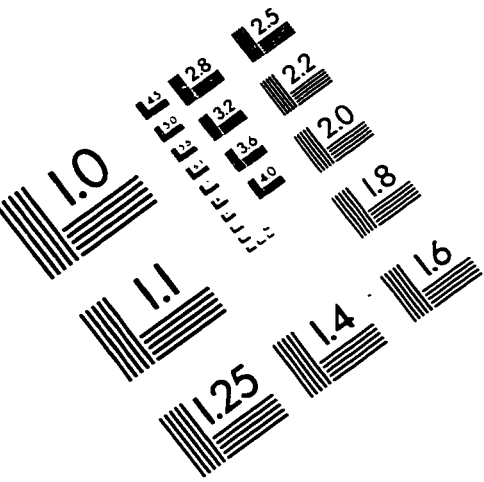
B.1. S-Record Conversion Program

The conversion program, written in C++ language, was a Windows-based executable program. This program was used only when the control program required to be programmed into the ROMs. The S-19 format file was generated after the assembly control program was compiled. Figure B-1 shows the format of a S-record file. The first three rows of the S-19 file consist of the information about the file name, the reset address and the interrupt service routine address. The characters "S1" are the standard format that start from row 2 to the second last row. The two characters after S1, for example "23" on the forth rows, mean there are 35 bytes (23 in hex = 35 in decimal) of data on that row. The odd address data is then stored into the ODD ROM and the even address data is then stored into the EVEN ROM. On the fourth row, the characters "1000" after S123, "10" is the even address data and "00" is the odd address data. Executing the conversion program produces two machine code files from the ASCII S-record file. An EPROM programmer is used to program the two machine code files into the ROMs. Once the program is burnt into the ROMs, the two ROMs will be plugged into the sockets on the main circuit board. When the power was turned on, the microcomputer system executed automatically.

S0090000474F4F442E6F30
 S10B00000F0100003FE0000F3
 S105002E1800B4
 S1231000F5FF27FA379C37B50FFF37FAFA4437B5015537FAFA4637B5000137FAFA4837B57C
 S12310206B7037FAFA4A37B5040537FAFA5037FAFA5437B55B7037FAFA5237B53B7037FA71
 S1231040FA5637B57F0037FAFA041735FA2175FF177FAFA17750E177FAFA1D7501177FAFA1FDA
 S123106075FF37FAFC1675FE177AFC177500177AFC1537B5A10437FAFC183705177AFC1ECA
 S123108037B500FF37FAFB0437B5000037FAFB061735FB00F50F379F37BF03FE37B50037D8
 S12310A037FAFC0837B5000C37FAFC0A37B5000037FAF70037B5008337FAF70A37B57F7038
 S12310C037FAF90637B5003037FAF92437B5040037FAF90C273500102735002827350020E0
 S12310E0273500122735001427350034FA00121AFA00138037BE13D4FA0013AEFA001380A7
 S123110037BE13E3FA0013AEFA00138037BE13F2FA0013AEFA00138037BE140CFA0013AE86
 S1231120FA0013A0FA0013BC17FA0014F833B2BCB6007A0012E6F832B6007A0011EAF830D2
 S1231140B2007A0010F027350004FA00138037BE142DFA0013AE27350030FA0011A217FA37
 S1231160002CFA0013A0FA0013BCF83AB62827350030FA0011A217FA002AFA0013A0FA009E
 S123118013BCF80DB6107581177FAFA1F7530177AF907FA0012247A0012C4FA00138E7A0046
 S12311A0114AFA0013A0FA0013BCF03017750030B61A17330030F805378E0024F800378D92
 S12311C0001E371437143714371417FA0010B0CEF809378E000AF800378D000417F100107A
 S12311E027F7FA00138E7A00114AFA001380FA00121A37B5000137FA003237B5FFFFF37FA3F
 S123120000347571177AF907FA001822FA00121AFA0012F8FA0013A0B0D0F504379D17FDB3
 S1231220000027F737B50E0037FAFC1C37B5003037FAFD2037FAFD2237FAFD2437FAFD26E9
 S123124037B500A037FAFD2827F537FAFD2A37FAFD2C37FAFD2E37B500A837FAFD3017F580
 S1231260002A37FAFD3217F5002C37FAFD34371537FAFD3637B500B137FAFD3837B500B4F3
 S123128037FAFD3A37B5001037FAFD3C37B5B1B137FAFD4037FAFD4437FAFD4837FAFD4C5E
 S12312A037B5B13137FAFD4237FAFD4637FAFD4A37FAFD4D37B5840437FAFC1A1775FC1F23
 S12312C0BAF627F737B5808037FAF70037FAF90037FAFC00370537FD274C274C27F1274CF0
 S12312E0FA001380B0DAFA00138037F5000437FA0032B6007A0013661735001A37B50009AF
 S123130037FA0010950037BC000A372AF13017FA001937CC37BC000A372AF13017FA00189F
 S123132037CC37BC000A372AF13017FA001737CCF13017FA0016F5FF379E37BE0016FA00E6
 S123134013AE3715379E3D02F520FA0013BC27310010B7007A001304FA00138027310032C3
 S1231360B7007A0012FC37F50034B7FE27F737BE145CFA0013AE7530177AF9077A0012C451
 S1231380F50DAFA0013BCF50AFA0013BC27F7FA00138037BE1464FA0013AEFA00138027F738
 S12313A01775FC0D7640B7F417F5FC0F27F7E500B704FA0013BC3E01B0F027F71775FC0C04
 S12313C07601B7F4750037FAFC0E1775FC0D7680B7F427F7312E2053746F726520646174FE
 S12313E0612000322E2043616C6962726174696F6E00332E204F75747075742074686520ED
 S123140073746F72656420646174610043686F6F73652031202D20333B206F746865727737
 S1231420697365205245534554203A2000494E505554205448452053414D504C494E47201E
 S1231440494E54455256414C20286D6D3A737329203A200052414D454E4420005448452066
 S1231460454E44004552524F522120005741495420464F5220494E5445525255505420007D
 S1231800F50F27FA3715379E37B5008037FAF70037FAF90037FAFC007531177AF907FA0062
 S12318201934177500207801B7087802B70CF50217F4F907B00AF50617F4F907B002F50CC1
 S123184017F4F90717FAF907F6CF17FAF90775F3177AFA19FA0018C01775F9077110177A16
 S1231860F90775F5177AFA19FA0018C01775F9077110177AF90775F9177AFA19FA0018C002
 S12318801775002071017803B704177A00207A001822273500202733000437F50034B7FE9C
 S12318A027F77530177AF90737B50E0037FAFC1C37B5840437FAFC1A1775FC1FBAF62777DD
 S12318C0FA00191C2735001037B5000537FA002637B5001037FAF70C1775F70EBAF637BCBD
 S12318E0F710850037F1001037FA00103C02377CF720B6EA27310026B6D237F5001037BC02
 S12319000028372A37CC9A003D02FA00191027F737ADF808B6007A00194627F737083718FE
 S123192037B5600037FA002227310022B6F63719370927F737081775FA197610B6007A009C
 S11919401946370927F77530177AF9077501177AFA1F7A0012C42A
 S9030000FC

Figure B-1. An example of a S-19 record file

IMAGE EVALUATION TEST TARGET (QA-3)



APPLIED IMAGE, Inc.
1653 East Main Street
Rochester, NY 14609 USA
Phone: 716/482-0300
Fax: 716/288-5989

© 1993, Applied Image, Inc., All Rights Reserved